PLASMA ASSISTED METAL ORGANIC CHEMICAL VAPOUR DEPOSITION OF YTTRIA AND YTTRIA STABILIZED ZIRCONIA COATINGS AND THEIR CHARACTERIZATION

By

Supriya Suresh Chopade

PHYS01200904019

Homi Bhabha National Institute

A thesis submitted to the

Board of Studies in Physical Sciences

In partial fulfillment of requirements for the Degree of

DOCTOR OF PHILOSOPHY

Of

HOMI BHABHA NATIONAL INSTITUTE

March, 2015

Homi Bhabha National Institute

Recommendations of the Viva Voce Committee

As members of the Viva Voce Committee, we certify that we have read the dissertation prepared by **Mrs.Supriya Suresh Chopade** entitled “**Plasma assisted metal organic chemical vapour deposition of yttria and yttria stabilized zirconia coatings and their characterization** ” and recommend that it may be accepted as fulfilling the thesis requirement for the award of Degree of Doctor of Philosophy.

KDasgupta

Chairman – Prof. K. Dasgupta **Date:**26.08.2015

DS Patil

Guide / Convener – Prof. D. S. Patil **Date:** 26.08.2015

Sahoo

Member 1 – Prof. N. K. Sahoo **Date:** 26.08.2015

P. Ayyub

Member 2- Prof. Pushan Ayyub **Date:** 26.08.2015

Rajiv Dusane

External Examiner- Prof. Rajiv O. Dusane **Date:** 26.08.2-015

Final approval and acceptance of this thesis is contingent upon the candidate’s submission of the final copies of the thesis to HBNI.

I hereby certify that I have read this thesis prepared under my direction and recommend that it may be accepted as fulfilling the thesis requirement.

DS Patil

Place: Mumbai **Guide**

---

[1] This page is to be included only for final submission after successful completion of viva voce.

STATEMENT BY AUTHOR

This dissertation has been submitted in partial fulfillment of requirements for an advanced degree at Homi Bhabha National Institute (HBNI) and is deposited in the Library to be made available to borrowers under rules of the HBNI.

Brief quotations from this dissertation are allowable without special permission, provided that accurate acknowledgement of source is made. Requests for permission for extended quotation from or reproduction of this manuscript in whole or in part may be granted by the Competent Authority of HBNI when in his or her judgment the proposed use of the material is in the interests of scholarship. In all other instances, however, permission must be obtained from the author.

Supriya

Supriya Suresh Chopade

DECLARATION

I, hereby declare that the investigation presented in the thesis has been carried out by me. The work is original and has not been submitted earlier as a whole or in part for a degree / diploma at this or any other Institution / University.

Supriya

Supriya Suresh Chopade

List of Publications arising from the thesis

Journal

1. ‘RF plasma MOCVD of Y_2O_3 thin films: Effect of RF self-bias on the substrates during deposition’,

   S. S. Chopade, S. A. Barve, K. H. Thulasi Raman, N. Chand, M. N. Deo, A. Biswas, Sanjay Rai, G. S. Lodha, G. M. Rao, D. S. Patil

   Appl.Surf.Sci.285P (2013) 524-531.

2. **‘**EXAFS Study on Yttrium oxide thin films deposited by RF plasma enhanced MOCVD under the influence of varying RF self –bias’,

   S. S. Chopade, C. Nayak, D. Bhattacharyya, S. N. Jha, R. B. Tokas, N. K. Sahoo and D. S. Patil

   Appl.Surf.Sci.314 (30) (2014) 400-407.

3. **‘**RF Plasma enhanced MOCVD of Yttria Stabillized Zirconia thin films using octanedionate precursors and their characterization’,

   S. S. Chopade, C. Nayak, D. Bhattacharyya, S. N. Jha, R. B. Tokas, N. K. Sahoo, M. N. Deo , A. Biswas , Sanjay Rai , K. H. Thulasi Raman , G. M. Rao , Niranjan Kumar Pandey and D. S. Patil

   Appl.Surf.Sci. 355 (2015) 82-92.

4. ‘Deposition and Characterization of Yttrium oxide thin films by RF plasma MOCVD using $Y(thd)_3$ and $Y(tod)_3$ precursors’

   S. S. Chopade , S. A. Barve , Jagannath , M. N. Deo , A. Biswas , S. Rai , N. Chand, G. S. Lodha , Niranjan Kumar , D. S. Patil

   Manuscript under preparation

Conferences

1. ‘Effect of Argon ion activity on the properties of DLC-SiOx thin films deposited by RF Plasma CVD process’,

   S. A. Barve , **S. S. Chopade** , R. Kar , N. N. Patel , R. Kishore , A. Biswas , N. Chand, V. Anand, G. M. Rao, D. S. Patil

   Thin Film Science and Technology (TFST-2011), Bhabha Atomic Research Centre, Mumbai, 09-12 November, 2011.

2. ‘Bias independent growth of carbon nanowalls’,

   R. Kar, N. Patel**, S. S. Chopade**, S. Mukherjee, A. K. Das, D. S. Patil

   2nd international conference on Advanced nanomaterials and nanotechnology, I.I.T. Guwahati, 08-10 December, 2011.

3. ‘A possible explanation of anomalous emissive probe behaviour in RF plasma’,

   R. Kar, S. A. Barve, **S. S. Chopade**, N. Chand, A. K. Das, D. S. Patil

   26th national symposium on plasma science and technology (Plasma-2011), Birla institute of technology, Patna, December, 2011.

4. ‘RF Plasma Assisted MOCVD of Yttrium Oxide Thin Films’, **S. S. Chopade** , S. A. Barve , N. Chand , M .N. Deo , A. Biswas , Sanjay Rai , G. S. Lodha , K. H. Thulasi Raman , G. M. Rao and D. S. Patil

   Plasma Science Society of India (PSSI)-Plasma Research Scholars Colloquim, Institute for Plasma Research, Gandhinagar, 03-04 July, 2012.

5. ‘Deposition and characterization of Yttrium Oxide thin films by RF Plasma Assisted MOCVD’,

   S. S. Chopade , S. A. Barve , N. Chand , Nidhi Mithal , Jagannath , Sanjay Rai , G. S. Lodha and D. S. Patil

   27th Plasma Science Society of India (PSSI) National Symposium on Plasma Science and Technology (Plasma-2012), Pondicherry University, Pondicherry, 10-13 December 2012.

6. ‘Plasma Assisted Metal Organic Chemical Vapour Deposition and Characterization of Yttria stabilized Zirconia thin films’,

   S. S. Chopade , K. H. Thulasi Raman , N. Chand , M. N. Deo , A. Biswas , Sanjay Rai , G. S. Lodha , G. M. Rao , Niranjan Kumar Pandey and D. S. Patil

   International Union of Materials Research Society-International Conference in Asia (IUMRS-ICA 2013), Indian Institute of Science, Bangalore, 16-20 December, 2013.

7. ‘Deposition of Yttrium Oxide thin films by RF plasma enhanced MOCVD using two different β-diketonate precursors’,

   S. S. Chopade , S. A. Barve , N. Chand , Jagannath , M. N.Deo , A. Biswas , S. Rai , G. S. Lodha , Niranjan Kumar , A. K. Tyagi and D. S. Patil

   National Symposium on Emerging Plasma Techniques for Materials Processing and Industrial Application (NSEPMI-2014), Pune University, Pune.13-15 February 2014.

8. ‘Effect of yttria doping on optical properties of Yttria stabilized Zirconia thin films deposited by RF plasma enhanced MOCVD’,

   S. S. Chopade , M. N.Deo , Arup Biswas , Sanjay Rai , G. S. Lodha and D. S. Patil .

   DAE-BRNS 5th Interdisciplinary Symposium on Materials Chemistry (ISMC-2014), BARC, Mumbai, 09-13 December 2014.

Others

1. ‘Anomalous Emissive Probe Behaviour in Reactive RF Plasma’,

   R. Kar, S. A. Barve, **S. S. Chopade**, A. K. Das and D. S. Patil

   Plasma Sources Sci.Technol 21 (2012) 055009.
2. ‘Bias independent growth of carbon nanowalls by microwave electron -cyclotron resonance plasma CVD’,

   R. Kar, N. N. Patel, **S. S. Chopade**, S. Mukherji, A. K. Das and D. S. Patil

   Journal of Experimental Nanoscience (2012) 1–7.
3. ‘Scratch resistance and tribological properties of SiO_x incorporated diamond-like carbon films deposited by r.f. plasma assisted chemical vapor deposition’

   N. Kumar, S. A. Barve, **S. S. Chopade**, Rajib Kar, N. Chand, S. Dash, A. K. Tyagi, D. S. Patil

   Tribology international, 84 (2015) 124-131.
4. ‘Effect of RF self-bias on the substrate during deposition of BxC coatings using ortho-carborane precursor by RF plasma enhanced CVD’,

A. Bute , **S. S. Chopade,** R. Kar, Jagannath , Pritty Rao , M. N. Deo , N. Chand , Sanjiv Kumar and D. S. Patil.

Manuscript under preparation.

5. **‘**Effect of substrate heating and microwave attenuation on the catalyst free growth and field emission of carbon nanotubes’

   R. Kar, S. Sarkar, C. Basak, A. Patsha, S. Dhara, C. Ghosh, D. Ramachandran, N. Chand, **S.S. Chopade**, D.S.Patil .

   Carbon, 94 (2015) 256-265.

Supriya

Supriya Suresh Chopade

ACKNOWLEDGEMENTS

I express my deep and sincere gratitude to my guide, Prof. (Dr.) D. S. Patil for his invaluable guidance, constant encouragement, keen interest and good wishes. His enthusiasm, punctuality, passion for research, knowledge of developing various plasma based systems and simplicity has made deep impression on me. I am also grateful to him for being patient during the course of this work and for critically reviewing the thesis.

I would like to give my sincere thanks to Dr. Dasgupta, Associate Director, Beam Technology and Development Group, Dr. A. K. Das, former head, Laser and Plasma Technology Division and Dr. Sucharita Sinha, Head, Laser and Plasma Surface Process Section for giving me an opportunity to work in Laser and Plasma Technology Division. I am grateful to doctoral committee members, Dr. Pushan Ayyub, Senior Professor, TIFR and Dr. N. K. Sahoo, Head Applied Spectroscopy for spending their precious time for periodic assessment of the work and giving valuable suggestions to enhance the quality of work.

It gives me pleasure to place on record my sincere thanks to Dr. P.V.A. Padmanabhan, Mr. S. N. Sahasrabudhe, Dr. K. Patel, Dr. S. Ghorui, Mr. A. Tak and Smt. Nirupama Tiwari for attending periodic review presentations and for giving their valuable suggestions.

I express my deep gratitude to Dr. M. N. Deo, Dr. Dibyendu Bhattacharya, Dr. Jagannath, Mr. R. Tokas, Ms. Chandrani Naik, Prof. G. M. Rao, Mr. Arup Biswas, Dr. G. S. Lodha, Mr. Sanjay Rai, Dr. Niranjan Kumar for providing the characterization facilities.

I offer my sincere gratitude to my section members, Mr. Rajib Kar, Mr. Naresh Chand, Ms. Arundhati Bute and Ms. Shazia Shaikh for their constant support and creating

a lively working environment. Interaction with them has been enjoyable, enriching and fruitful in many ways. I sincerely acknowledge Mr. K. C. Meher, for his help throughout the course of this work. It gives me immense pleasure to thank my senior, Dr. Shruti Barve for her support during initial phase of this work. My special thanks to Mr. Sankalp Thakur for his help during experimental setup.

I take this opportunity to thank my other colleagues Ms. Gayatri Dhamale, Ms. Vandana Chaturvedi and all well wishers for their unconditional support and help. I am grateful to Mr. Amey Wadawale for his help during formatting of the thesis.

I am thankful to Dr. Mohanty, Dean of Academics, Physical Sciences, HBNI for his support during the course of this work. I gratefully acknowledge the financial support provided by DAE and HBNI during course of these investigations.

It gives me pleasure to express my deep gratitude to my parents, in-laws and all my family members for their constant support, well wishes and encouragement. I specially acknowledge the help provided by my husband Mr. Suresh Chopade during drafting of thesis and co-operation from my dear son Soham who allowed me the space and time to carry the present work.

Supriya

Supriya Suresh Chopade

CONTENTS

Plasma Assisted Metal Organic Chemical Vapour Deposition of Yttria and Yttria Stabilized Zirconia Coatings and their Characterization

Synopsis

Plasma as a medium has been proved to be very effective in deposition of thin films as well as for surface engineering and surface modification treatments [**1**]. Low pressure plasma assisted chemical vapor (CVD) deposition technique present significant advantages as compared to conventional CVD technique. Due to high internal energy of plasma medium, deposition can be done at lower substrate temperature. Further, there is uniform mixing of precursor vapors that results in uniform and dense coatings. Because of the presence of the energetic particles, the precursor fragmentation is effective that results in desired chemical reactions [**2**]. Radio frequency plasma enhanced CVD is one such technique. While RF power can be coupled to the plasma in an inductively coupled or capacitively coupled manner, here capacitively coupled RF plasma discharge at 13.56 MHz is used. These type of plasmas are characterized by plasma density of ~ 10^9 -10^{10} cm^{-3} and plasma potential of approximately 100 V. A 40 cm diameter stainless steel chamber is used for deposition. An impedance matching network is used to couple RF power to the electrode on which substrates are placed. Additional advantage of capacitively coupled RF plasma enhanced CVD process is that it is possible to self bias the substrate to a DC negative potential. Due to presence of negative self bias on the substrates and high plasma potential, the ions are accelerated towards the substrates leading to compact thin films.

In the present work capacitively coupled RF plasma has been used to deposit yttrium oxide (Y_2O_3) and yttria stabilized zirconia (YSZ) thin films by metalorganic chemical vapor deposition (MOCVD). β diketonate precursors, (2,2,6,6,tetramethyl-3,5-heptanedionate) yttrium (known as $Y(thd)_3$) is used for deposition of yttrium oxide while (2,7,7-trimethyl-3,5-octanedionate) yttrium (known as $Y(tod)_3$) and (2, 7, 7-trimethyl-3, 5-octanedionate) zirconia (known as $Zr(tod)_4$) is used for deposition of yttria stabilized zirconia thin films. Plasma assisted MOCVD has emerged as one of the promising techniques for deposition of thin films. MOCVD technique has various advantages like low deposition temperature, good conformal coverage, uniform coating of the substrate, possibility of large scale production and ease of compositional control in complex films. Different types of thin film coatings of oxides, carbides, borides, nitrides, silicides and chalcogenides can be deposited by MOCVD [**3, 4**].

Yttrium oxide is a refractory ceramic with high melting point (2410 °C). It is used as a corrosion resistant coating [**5**]. It has high dielectric constant (~18) and good lattice matching with silicon, hence Y_2O_3 is considered as a potential candidate for use in microelectronic industry [**6**]. Y_2O_3 has wide band-gap (~5.1 eV) and is transparent from near infrared to ultraviolet region of electromagnetic spectrum hence it finds application as antireflection and protective coating [**7**].

Zirconium oxide (ZrO_2) is a wide band gap (~5.1eV) material with high dielectric constant (~18). It is chemically inert. Hence ZrO_2 thin films are finding applications as dielectric material in microelectronic industry [**8**]. It exists in monoclinic form at room temperature and undergoes destructive phase transition with temperature rendering it useless for technological applications. Doping ZrO_2 with divalent or trivalent dopants can stabilize high temperature phases at room temperature. Fully stabilized zirconia finds applications in oxygen sensor and as electrolyte in solid oxide fuel cells (SOFC). Partially stabilized zirconia

(PSZ) is known for its mechanical properties and hence used as wear and fracture resistant coating [**9**].

The above mentioned oxide systems were chosen during the studies reported here because of their stated potential applications. The objective of this thesis is to deposit these films by plasma assisted MOCVD process characterize the deposited coatings and correlate the observed properties with the process parameters.

The investigations carried during the course of this thesis are organized into seven chapters. **Chapter 1** consists of introduction to plasma assisted CVD and about the oxide systems that are studied here. Structures of different phases of yttria and yttria doped/stabilized zirconia are discussed in brief. Literature review on yttrium oxide and yttria stabilized zirconia coatings, including different deposition techniques used along with characterization and applications of these coatings are discussed here. A brief discussion regarding working principles of characterization techniques that are used is also included. The discussion is on characterization techniques such as stylus profilometer, spectroscopic ellipsometry, glancing incidence X-ray diffraction (GIXRD), fourier transform infrared (FTIR) spectroscopy, X-ray spectroscopy (XPS), scanning electron microscopy (SEM), atomic force microscopy (AFM) and extended X-ray absorption fine structure (EXAFS).

Chapter 2 discusses about the experimental details. This chapter gives details about precursor selection, deposition system and experimental procedure. The substrates used for deposition were silicon, stainless steel (s.s.), quartz and tantalum. The substrates were cleaned by chemical method and then sputtered by argon plasma for 20 minute before deposition. Plasma of metal organic precursor vapors along with argon and oxygen gases is used for deposition. It is possible to control the flow of metal organic precursor vapors by controlling the temperature of the precursor.

Chapter 3 discusses about RF plasma enhanced MOCVD of yttrium oxide thin films. The films have been deposited by using plasma of Y(thd)$_3$ precursor vapors along with argon and oxygen gases. The Y(thd)$_3$ precursor temperature is maintained at 190 °C. The RF self bias is varied from -50 volt to -175 volt in steps of -25 volt and films (6 no.) are deposited keeping all other experimental parameters same. Depositions are carried for a period of one hour at a substrate temperature of 350 °C. The films were characterized by XRD, XPS, IR spectroscopy, spectroscopic ellipsometry, and SEM. The structural and optical properties of the films change with bias. The content of adsorbed moisture decreases for film deposited at -75 V as compared to film deposited at -50 V. However, beyond bias level of -125 volt, sputtering effects dominate and there is formation of nanocrystalline phase indicating degradation in crystallinity of the deposited films. The films deposited at -75 V and -125 V are oriented in (111) direction which is the preferred growth direction where surface energy is minimum. Refractive index of the film deposited at -150 V is highest due to nanocrystalline nature of the film. Films deposited at -75 V and -125 V are oriented along (111) direction and show similar value of refractive index. There is change of orientation for film deposited at -100 volt which is due to change in oxygen vacancy ordering. Change in orientation causes strain in the film resulting in decrease in thickness and refractive index of the film. The refractive index for film deposited at -175 V has decreased due to sputtering and further degradation of the crystal structure. The extinction coefficient for all the films is zero indicating that the films are transparent from near IR to UV range of the electromagnetic spectrum; a property useful in fabrication of antireflection and protective coating [**2**].

Chapter 4 gives details regarding the EXAFS analysis on the deposited Y_2O_3 films under different bias conditions. EXAFS measurements on these samples at Y K edge are carried out in fluorescence mode at the Scanning EXAFS Beamline (BL-9) at the INDUS-2 Synchrotron Source (2.5 GeV, 100 mA) at the Raja Ramanna Centre for Advanced Technology (RRCAT), Indore, India. For measurements in the fluorescence mode, the sample is placed at 45^o to the incident X-ray beam and the flourosecnce signal (I_f) is detected using a Si drift detector placed at 90^o to the incident X-ray beam. An ionization chamber is used prior to the sample to measure the incident X ray flux (I_0) and the absorbance of the sample ($\mu = \frac{I_f}{I_0}$) is obtained as a function of energy by scanning the monochromator over the specified energy range. The absorption spectra of the samples at Y K edge are recorded in the energy range 16960- 17650 eV.

It is observed that co-ordination number is higher for film deposited at -50 volt and thereafter decreases and remains constant with bias on the substrate. The bond length in general decreases with bias indicating decrease in hydroxyl content in the films. Film deposited at -100 volt shows abrupt decrease in bond length due to generation of compressive stress. This stress can arise due to increase in number of dangling bonds as orientation of film has changed to (100). The disorder factor is similar for films deposited at bias voltages from -50 to -125 V and is highest for films deposited at bias level beyond -125 volt due to dominance of sputtering effect. This result also corroborates with AFM measurements which indicate increase in root mean square roughness and entropy at high bias levels.

Chapter 5 describes about deposition and characterization of Y_2O_3 films deposited using two different β diketonate precursors; $Y(thd)_3$ and $Y(tod)_3$. The films were deposited at

RF self bias voltage of -75 volt on the substrates with 200°C precursor temperature and 350 °C substrate temperature. All other deposition parameters being same, the properties of the two films are compared with the help of various characterization techniques. The films were characterized by GIXRD, FTIR, XPS, spectroscopic ellipsometry and SEM. The octanedionate precursors are known for high volatility and less carbon contamination in the deposited films [**4**]. Due to high volatility of $Y(tod)_3$ precursor; the deposition rate is enhanced for the film deposited using $Y(tod)_3$ leading to increase in nucleation density and formation of nanocrystalline structure. The refractive index is enhanced for film deposited using $Y(tod)_3$ precursor.

Chapter 6 discusses about the deposition and characterization of yttria stabilized zirconia thin films by RF plasma MOCVD using $Zr(tod)_4$ and $Y(tod)_3$ precursors at self bias of -100 volts. The substrate temperature is maintained at 350 °C. Precursor $Zr(tod)_4$ is maintained at 220 °C while the temperature of $Y(tod)_3$ temperature is varied at 110 °C, 130 °C and 160 °C leading to 4 mol %, 5 mol % and 9 mol % of yttrium oxide incorporation in the films respectively. With the variation of yttria content in the film there is a variation in the deposited phase and the properties of the deposited films. The deposited films were characterized by GIXRD, FTIR, XPS, spectroscopic ellipsometry, AFM, EDAX, EXAFS and SEM**.** To study the mechanical behaviour, scratch adhesion test and measurement of coefficient of friction is done. The GIXRD results could not indicate about the exact amount of phases formed. However, phase identification is possible with the help of IR spectroscopy. The film with 4 mol % Y_2O_3 is a mixture of monoclinic and tetragonal phases, film with 5 mol % Y_2O_3 has majority of tetragonal phase while film with 9 mol % Y_2O_3 has cubic phase. The values of refractive indices obtained for the films are in conformity with the values reported in literature. The extinction coefficient is zero for all the three films for the investigated range from UV to near IR. Study of mechanical properties indicates that the film with 4 mol % yttria possess highest wear resistance. EXAFS analysis supports the above findings and gives an idea about the location of oxygen vacancy. Zr^{+4} ion is retaining its co-ordination while co-ordination of Y^{+3} ion has decreased to 6 indicating that oxygen vacancies are located near the Y^{+3} ion

Chapter 7 summarizes the important conclusions and findings of the present work. This chapter also discusses about the scope for the future work.

References:

1. J Reece Roth, '*Industrial Plasma Engineering, Vol- 2: Applications to Nonthermal Plasma Processing*', published by Institute of Physics Publishing (Bristol and Philadelphia).

2. S. S. Chopade, S. A. Barve, K. H. Thulasi Raman, N. Chand, M. N. Deo, A. Biswas, Sanjay Rai, G. S. Lodha, G. M. Rao, D. S. Patil, '*RF plasma MOCVD of Y_2O_3 thin films: Effect of RF self-bias on the substrates during deposition*', Appl. Surf. Sci. 285P (2013) 524-531.

3. F. Maury, '*Recent Trends in the Selection of Metal-Organic Precursors for MOCVD process*', J. Phys. IV, 5 (1995), C5-449-C5-463.

4. Serej V. Pasko, Liliane G. Hubert-Pfalzgraf, Adulfas Abrutis, Phillippe Richard, Ausrine Bartasyte and Vida Kazlauskiene, '*New sterically hindered Hf, Zr and Y β-diketonates as MOCVD precursors for oxide films'*, J. Mater. Chem. 14, (2004) 1245-1251.

5. W. J. Varhue, M. Massimo, J. M. Carrulli, V. Baranauskas, E. Adams, '*Deposition of* Y_2O_3 *by plasma enhanced organometallic chemical vapor deposition using an electron cyclotron resonance source'*, J. Vac. Sci. Technol. A 11 (1993) 1870-1874.

6. J. J. Araiza, M. A. Aguilar-Frutis, C. Falcony, '*Optical, electrical and structural characteristics of yttrium oxide films deposited on plasma etched silicon substrates'*, J. Vac. Sci. Technol. B 19(6) (2001) 2206-2211.

7. G. Alarcón-Flores, M. Aguilar-Frutis, M. García-Hipolito, J. Guzmán-Mendoza, M. A. Canseco, C. Falcony, '*Optical and structural characteristics of* Y_2O_3 *thin films synthesized from yttrium acetylacetonate'*, J. Mater. Sci. 43 (2008) 3582-3588.

8. Cheol Seong Hwang, Hyeong Joon Kim, '*Deposition and characterization of* ZrO_2 *thin films on silicon substrate by MOCVD'*, J. Mater. Res. 8 (6) (1993) 1361-1367.

9. D. Majumdar, D. Chatterjee, '*X-ray photoelectron spectroscopic studies on yttria, zirconia and yttria-stabilized zirconia'*, J. Appl. Phys. 70 (2) (1991) 988-992.

Monitoring / Doctoral Committee:

S. No.	Name	Designation	Signature	Date
1	Prof. K. Dasgupta	Chairman	KDasgupta	12/8/14
2	Prof. D. S. Patil	Guide & Convener	DSPatil	12/8/14
3	Prof. Pushan Ayyub	Member	Pushan Ayyub	12/8/14
4	Prof. N. K. Sahoo	Member	Sahoo	12/8/14

List of figures

Chapter-1

Chapter-2

Chapter-3

Chapter- 4

Chapter-5

Chapter-6

List of tables

Chapter 1

Introduction

This thesis reports on deposition and characterization of yttrium oxide (Y_2O_3) and yttria doped zirconia (YSZ) thin films. Both materials are refractory ceramics having important technological applications. The deposition of these thin films is carried out by capacitively coupled radio frequency (RF) plasma enhanced metalorganic chemical vapor deposition (MOCVD). Deposition of Y_2O_3 and YSZ coatings is also reported in literature using various other techniques but there are very few reports on deposition of these materials by RF plasma enhanced CVD process. Plasma as a deposition medium ensures uniform mixing of precursors and presence of highly energetic plasma species enables deposition of these coatings at lower substrate temperature. It can be seen from present work that Y_2O_3 and YSZ thin films deposited by process of RF plasma enhanced CVD are uniform, with good adhesion with the substrates and are nearly stoichiometric. The RF self bias on the substrate during deposition plays an important role in deciding the properties of the deposited films.

This chapter gives a brief introduction on the topic of thesis. A brief discussion on plasma, plasma sources and application of plasma sources is given. Various methods for deposition of thin films are described. A short introduction to RF plasma enhanced CVD and its advantages are given followed by discussion on yttria and yttria doped zirconia ceramics including their different phases and applications. Previous reports on deposition and characterization on these oxide coatings are also described in the section on literature review. A short description about the working principles of different characterization techniques is also included followed by thesis organization.

1.1 Plasma

Plasma is considered as the fourth state of matter which consists of ions, electrons and neutrals. The word ‘plasma’ is derived from the Greek word plásma meaning something that can be molded or fabricated. The flash of lightning bolt in the sky, fluorescent lamps, neon signs are some examples of plasma that we encounter in day to day life. The stellar interiors, atmosphere, gaseous nebulae consists of plasma.

The earliest work on plasma was reported by Langmuir, Tonks and co-workers in 1920’s. They were working on vacuum tubes that would carry large currents and hence had to be filled with ionized gas. Plasma can be defined as a quasi-neutral gas of charged particles and neutrals which exhibit collective behavior [**1**]. The separation of charges in the plasma can result into localized electric fields, but as the total number of positive and negative charges is same, overall the plasma is neutral; hence it is defined as a quasi-neutral gas. The motion of charged particles set up currents and fields which affect the motion of other charged particles which are at a distance. The constituents of plasma also show collective behavior.

The Saha ionization equation (1.1) gives the amount of ionization occurring in a gas at thermal equilibrium.

$$\frac{n_i}{n_n} \approx 2.4 \times 10^{21} \frac{T^{3/2}}{n_i} e^{-U_i/KT} \qquad (1.1)$$

Here (n_i) and ($n_{n)}$ are the densities (number per m^3) of ionized atoms and of neutral atoms, T is the gas temperature in °K, (U_i) is the ionization energy of the gas and K is the Boltzmann’s constant.

From the above equation, it can be seen that at room temperature, the fractional ionization produced is of order of $n_i/n_n \approx 10^{-122}$ which is considerably low. This fraction becomes considerable only when U_i becomes few times KT and the gas reaches plasma state [**1**].

A gas in thermal equilibrium has particles of all velocities and the most probable distribution of the velocities is known as Maxwell's distribution. Thus at any given temperature there are some particles having energy higher than the average energy and these are responsible for ionization of gas through collisions with stray electrons and with other neutrals. Depending on pressure and density of species, the plasma can be broadly classified as thermal and non thermal plasma. In case of thermal plasma due to high pressure there are frequent collisions between the plasma species, thus equalizing the temperature of all plasma species. In this condition the plasma is in local thermal equilibrium (LTE). On other hand, in case of non thermal plasma, as the pressure is low, energy exchange between ions and electrons is less, resulting in two different temperature distributions for the ions and electrons and hence the plasma is in non-LTE. There are few exceptions like dielectric barrier discharge and atmospheric glow discharge, where the temperature distribution depends both on pressure and the distance between the electrodes (frequency of the power supply). Owing to high gas temperature associated with LTE systems, these systems are used for applications such as cutting, welding, spraying, etc. In such systems the plasma power density is in the range of 100 W/cm^3 to above 10 KW/cm^3 whereas non LTE systems are used for various processes such as thin film deposition, surface modification, etching and generally have power density in the range of 10^{-4} to a few tens of watt per cm^3 [**2**].

The overall characteristics of plasma state is decided by the nature of precursors, pressure of gas inside the chamber, power fed into plasma, frequency of power supply used and the configuration of electrodes. Depending on these parameters different types of plasma discharge systems can be configured. Some non-LTE systems and their applications are discussed here in brief.

1.2 Types of plasma sources

1.2.1 *Direct Current (DC) discharge*

Here a DC electric field is applied between two electrodes that lead to acceleration of stray electrons. The accelerated electrons by way of inelastic collisions excite the atoms, ionizing them. The ions bombard the cathode, causing emission of secondary electrons. These electrons are responsible for sustaining the discharge.

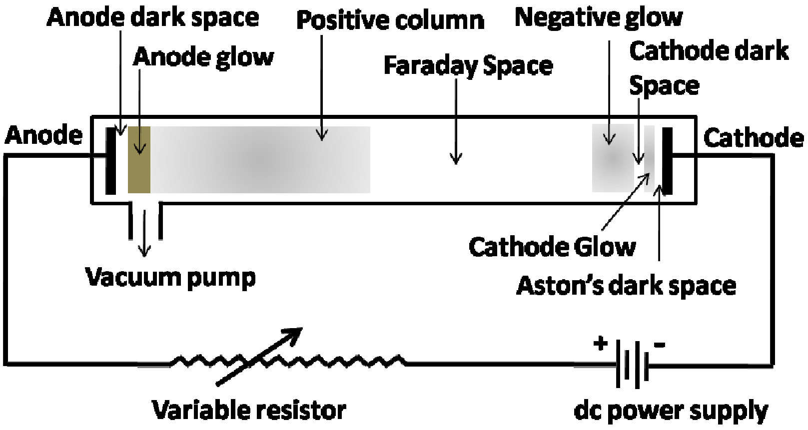

Figure 1.1: Schematic of DC plasma discharge [Ref-**3**]

The de-excitation within the visible region causes the discharge to glow. The DC discharge is characterized by different regions as shown in **Figure 1.1** and there is change of electric field strength as one goes from cathode to anode. The region adjacent to cathode is characterized by a strong electric field called the cathode dark space; it arises due to the sheath region, where recombination of charges does not take place. Next is the negative glow region, it is the brightest region of the entire discharge as it has high density of both electrons and ions. When the distance between anode and cathode is relatively longer, two more regions known as the Faraday dark space and the positive column are present. In Faraday dark space, the electron energy and axial electric field is small. The positive column has low net charge density but sufficient electric field to maintain ionization. The anode glow is slightly brighter than the positive column. The anode dark space has negative charge density and a higher electric field as compared to the positive column. The DC discharge can operate over a wide range of pressures from 1 Pa to atmospheric pressure. The voltage used in the range 300 to 1500 V or more depending on the electrode configuration and the current is in the range of milli ampere [**4**].

1.2.2 *Radio Frequency (RF) discharge*

For sustaining the DC discharge, both the electrodes should be conducting. While using DC discharge for applications like thin film deposition of dielectric material, there will be a charge accumulation on the electrodes resulting in extinction of glow discharge. To overcome this barrier the electrodes are applied a varying electric field. The electrodes alternately change polarity and the accumulated charge can be fully or partially neutralized. The frequency used should be high enough so that the half the period of applied voltage is less than the time required for electrode to charge up. Otherwise there would be a series of short lived discharges with electrodes successively taking the opposite polarities instead of a quasi continuous discharge.

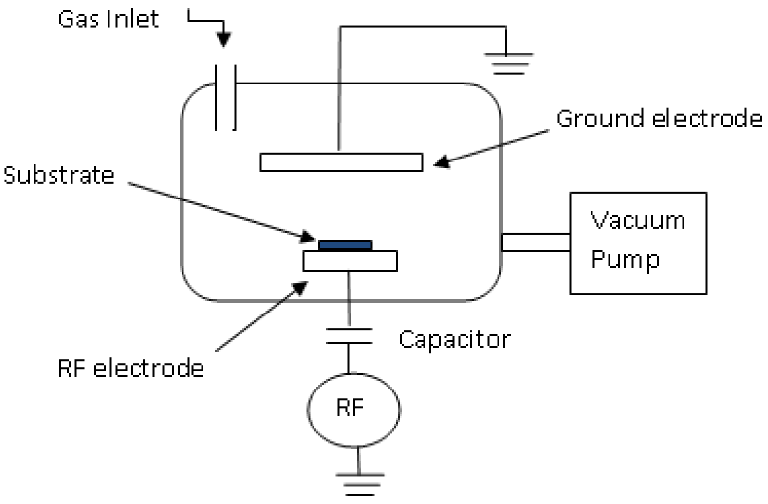

(a)

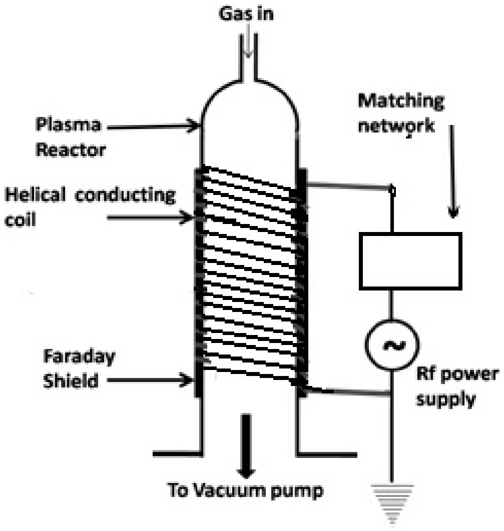

(b)

Figure 1.2: Schematic of (a) Capacitively coupled RF discharge (b) Inductively coupled RF discharge [Ref-**4**, **3**]

The frequencies used are generally in radio frequency range of 1to 100 MHz **[5]**. At these frequencies the electrons can respond to the high frequency field but the ions due to their heavy mass cannot follow the field variations. While using radio frequency for creating discharge, two types of configurations are possible, inductively coupled plasma and capacitively coupled plasma. Inductively coupled plasma configuration leads to a high electron number density and low plasma potential that has advantage for semiconductor processing. Capacitively coupled plasma generation leads to a relatively low plasma density but high plasma potential. Further, the capacitively coupled plasma when coupled to a substrate immersed in plasma can be used for development of a self bias on the substrates. This has a very large number of applications in plasma based material processing. The generation of self-bias voltage on the substrates can be attributed to different response times of electrons and the ions to the applied RF field.

The self-bias DC voltage is formed when the electrodes have different size and a coupling capacitor is used between the electrode and RF power supply or when one of the electrodes is non conducting. The detailed mechanism of self bias generation is discussed in chapter-2.

1.2.3 *Pulsed DC glow discharge*

For these discharges, a pulse voltage of order of milli- or microseconds is applied to the electrode. A pulsed power supply can operate at higher currents and higher peak voltages for the same average power as in DC glow discharge, hence higher instantaneous ionization, sputtering is possible. Typically the peak voltage used is of the order of 500-800 V and pressure is ~100 Pa. In case of pulsed power discharges, the “power on” period is smaller than “power off” period. Because of less electrical power consumed, excess heating of the substrates is avoided. As compared to RF discharges, pulsed DC discharges have advantage that they do not require impedance matching network.

1.2.4 *Atmospheric pressure glow discharge (APGD)*

In this case a glow discharge is created between two electrodes (that may be covered by an insulating layer). A gas flow is maintained through the discharge volume and an alternating voltage of ~ 20 KV having frequency in the range of 1-30 KHz is applied. Distance between electrodes is few millimeter. The type of gas decides about the stability of the glow. For example, helium can give rise to stable discharge while with the use of gases like argon, oxygen and nitrogen, transition to filamentary glow discharge takes place. However operation in homogeneous glow discharge is possible by changing the electrode configuration. Main advantage is absence of vacuum condition; that makes the processing of high vapor pressure materials like rubber, textiles, biomaterials etc easier.

1.2.5 *Dielectric barrier discharge (DBD)*

This is similar to atmospheric pressure glow discharge. Basic difference between APGD and dielectric barrier discharge is that APGDs, are characterized by only one current pulse per half cycle while, DBDs consist of micro discharge filament of nanosecond duration. Two basic DBD configurations can be distinguished as the volume discharge and the surface discharge. In case of volume discharge, the system consists of two parallel plates; the micro discharges take place in thin channels spread randomly over the electrode surface. The surface discharge consists of number of surface electrodes on a dielectric layer and a counter electrode on the reverse side. There is no clearly defined discharge gap. The nanosecond discharge of DBDs is due to charge buildup at the dielectric surface within few nanoseconds after breakdown. This reduces the electric field at the position of discharge to such an extent that the charge current is interrupted. Due to the limited charge transport and energy dissipation, heating of gas is avoided leading to utilization of electron energy in exciting and ionizing the atoms and molecules.

1.2.6 *Electron cyclotron resonance (ECR)*

These discharges are created by setting electrons in resonance with the applied microwave field owing to the interaction between the applied electric and the magnetic field. The frequency of gyration of charged particles around the magnetic field is independent of velocity of particles. The DC magnetic field is produced by one or more electromagnetic windings and varies in the axial direction. A linearly polarized microwave field is applied axially through a dielectric wall to the plasma. This field can be decomposed into two circularly polarized waves rotating in opposite directions, namely, left handed circularly polarized (LHP) and right handed circularly polarized (RHP).

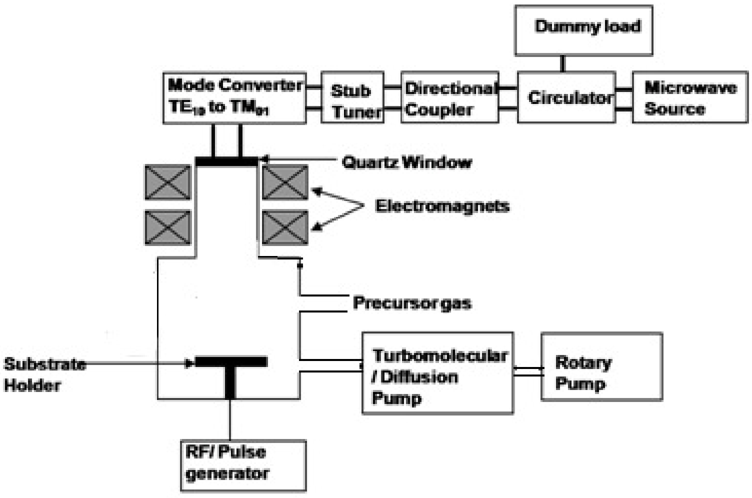

Figure 1.3: Schematic of ECR plasma discharge system [Ref-**3**]

The electric field of RHP wave rotates in the right handed direction around the magnetic field with a frequency ω while the electrons also gyrate in same manner with a frequency ω_c . When the magnetic field is such that $\omega = \omega_c$, the electrons continuously gain energy along a circular path. Hence there is resonance between the microwaves and the electrons and maximum power is absorbed. The LHP field on the other hand produces oscillating force whose time averaged value is zero and does not lead to any energy gain. However, the energy gained by electrons from the RHP wave is sufficient for the electrons to cause ionizing collisions. The ECR reactor essentially consists of two regions, the resonance region and the process region. The plasma flows along magnetic field lines from resonance region to the process region [**2**].

1.3 Application of plasma sources

With advances in modern technology plasma sources are finding a lot of applications in a variety of fields. The technologically important characteristic feature of non LTE plasma discharges is the role played by the active plasma species. Active plasma species promote reactions that are thermodynamically allowed but kinetically hindered or would normally require high temperatures, to occur at comparatively lower temperature. The active species produced by electron neutral collision includes neutral as well as charged reactive species. The neutral species include reactive atomic species, free radicals, light molecular fragments such as CH_2, heavy molecular fragments which can form complex compounds on the surfaces and promote branching and cross-linking of molecules, excited molecular states. The charged species include electrons, ions and molecular ions such as OH^-. The ions can be positive or negative. Positive ions are produced by ionization and charge exchange, while formation of negative ions is generally not possible under vacuum conditions and take place in atmospheric pressure plasmas by attachment of electrons. Use of plasma processing also contributes to reduction in pollutants and environmental contaminants. Further use of plasma in various processing also helps in increasing the energy efficiency.

Some applications of plasma discharge based processing are listed,

1.3.1 *Surface modification*

Interaction of plasma with surfaces has been put to various technological applications. These include,

1.3.1.1*Plasma surface treatment or surface activation*

Plasma can be utilized for surface decontamination, sterilization, enhancing the surface energy, improving the adhesive and cohesive properties, altering the surface finish of the surface of the material. Specific applications of plasma surface cleaning include improving the wettability, wickability and printability of fibers, films and fabrics, dewaxing of wool or other animal fibers.

1.3.1.2 *Plasma ion implantation*

In this process energetic ions are produced by acceleration across a plasma sheath surrounding the substrate and implanted into the surface. Plasma ion implantation has been utilized for enhancing the wear resistance of drill bits. The corrosion resistance and pitting potential of aluminum and stainless steel is enhanced by plasma ion implantation.

1.3.1.3 *Sputter deposition of thin films*

Here energetic ions sputter atoms from target which are re-deposited as a thin film on a substrate surface. These sputter coated films have large industrial applications.

1.3.1.4 *Plasma enhanced chemical vapor deposition (PECVD)*

In late 1960s use of plasma for deposition of thin films in microelectronics industry was appreciated. In this process, active plasma species of the precursors react to form a thin film on the substrate. Films deposited by PECVD are finding applications in various areas like microelectronic industry, decorative and ornamental coatings, corrosion resistant coating, protective layer for optical components and in many other areas.

1.3.2 *Plasma displays*

Here, the discharge gas is usually a mixture of rare gases. The discharge forms plasma that emits light in visible and ultraviolet (UV) region of electromagnetic spectrum. In case of monochrome plasma displays, visible light can be used directly, while in case of color plasma displays, UV light is used to excite phosphor. The discharge can be operated in alternating current (AC) or direct current (DC) mode.

1.3.3 *LASERS*

Gas discharges can be used for making lasers. Here the gas at reduced pressure is contained within a glass discharge tube with mirrors at the end of the tube. Anode and cathode can be placed at both ends of the tube. The cathode can also have a hollow structure with anode rings at the end. Few examples are atomic lasers (He-Ne laser, copper vapor laser) and molecular lasers (CO_2, N_2, excimer laser).

1.3.4 *Production of ozone*

Ozone production is typical application of DBDs or high pressure gas discharges. Ozone can be generated from oxygen, air or from N_2/O_2 mixtures. First the O_2 molecules are dissociated by electron impact and by reaction with nitrogen atoms or excited N_2 molecules. Ozone is then formed by reaction of O_2 molecules with oxygen atoms. Major application of ozone is in water purification and pulp bleaching. In field of organic synthesis, applications include ozonation of oleic acids and production of hydroquinone, piperonal, certain hormones, antibiotics, vitamins, flavors and perfumes.

1.3.5 *Environmental applications*

Thermal plasma sources can be used for destruction of hazardous wastes. With the help of thermal plasma, organic waste can be destroyed with high efficiency, metals can be recycled, heavy metals and low level radioactive materials can be vitrified. The non-thermal plasmas mainly used for environmental applications are high pressure discharges such as DBDs and pulsed corona discharges. Many harmful organic compounds are readily attacked by exciting species, free radicals, electrons, ions and UV photons generated in DBDs.

1.3.6 *Biomedical applications*

Plasma is used to enhance the biocompatibility of materials. Plasma sterilization of biological samples is gaining importance due to high efficiency of destruction of harmful microbes.

1.3.7 *Particle sources*

Since plasma consists of electrons, ions, excited atoms and radicals, it can be used as primary source of these particles [**2**].

1.4 Deposition of thin films

Thin films have been used since centuries from applications ranging from decorative coatings to protective layers. Thin films have left no field untouched and their applications can be widely seen in areas such as optics, magnetic materials, microelectronics, displays, biomedical applications, automobiles, construction, etc. By coating the base material, with thin film, a surface with properties significantly different from the bulk can be obtained. This provides the flexibility of choosing the base material according to requirements such as mechanical support, stability and cost. Thin films are routinely used to protect the materials from corrosion, excess heat, scratch, wear and harmful chemicals. Thin films with required optical and mechanical properties can greatly enhance the performance of the device in which they are used.

Various deposition methods have evolved over a period of time catering to different requirements. Selection of deposition process will depend on cost effectiveness, control of film thickness and microstructure, ability to acquire desired stoichiometry at required temperature, availability of suitable precursors and control on film substrate interface and defects created in the deposited films. The deposition techniques for thin films can be broadly categorized into two groups such as physical vapor deposition and chemical deposition methods.

1.4.1 ***Physical vapor deposition (PVD)***

Physical vapor deposition is widely used for depositing thin films. This method involves evaporation of material to be deposited, transport of vapor onto the substrate and finally condensation of vapors on the substrate to form thin films. Vaporization of the material to be deposited is either achieved by thermal evaporation or by sputter deposition.

In case of thermal evaporation, the material to be deposited (also known as source) is heated above its melting point in high vacuum and the vapors then condense on the substrate. The evaporation of the source material can be achieved by various means such as resistive heating, electron beam, high power laser beam, pulsed laser beam or by RF heating.

In case of sputter deposition, the source material is bombarded by highly energetic noble gas ions in a vacuum chamber. The noble gas atoms hit the source material and eject atoms. These ejected or sputtered atoms are transferred to the substrate and condense to form thin films. Different types of sputter deposition techniques are DC sputtering, RF sputtering, magnetron sputtering and ion beam sputtering.

The disadvantage of physical vapor deposition technique is that it is a line of sight technique and can result in uneven thickness of the deposited films. Coating of complex shape structures cannot be done.

Molecular beam epitaxy (MBE) is another important PVD technique. MBE is a highly sophisticated technique for the growth of single-crystal epitaxial films by means of solid-source evaporation in an ultra-high vacuum environment (Knudsen effusion cells). The process provides high degree of reproducibility as well as flexibility and accuracy. Furthermore, it allows fabrication of intricate alloy and super lattice structures [**6**]**.**

1.4.2 *Chemical deposition (CD)*

The CD process is based on a thermal decomposition of starting materials, on a heated substrate. Chemical reaction is an essential characterization of this method. Broadly on the nature of deposition medium used the chemical deposition technique can be classified into two groups- i) methods involving liquid phase reactions and ii) methods involving gas phase reactions.

i) Liquid phase chemical reaction methods

The liquid phase reactions methods are electrode less deposition, anodisation, liquid phase epitaxy, spin coating, spray pyrolysis, etc.

Some of the liquid phase reaction methods are discussed below,

a) Spray pyrolysis technique

This process involves generation of droplets from spray solution (atomization) and spraying it on the substrates. For this normally, air blast, ultrasonic or electrostatic techniques are used. After leaving atomizer droplets undergo physical and chemical changes while travelling through ambient conditions and are deposited on the substrate.

This method was introduced by Chamberlin and Skarman in1966 for deposition of CdS thin films for solar cell applications. Since then, spray pyrolysis has been used for deposition of SnO_x, InO_3, PbO, ZnO_3, ZrO_2, YSZ, etc.

Advantages of this method are,

- Cost effective and easily performed.
- Complex geometry substrate can be coated.
- Uniform and high quality coating can be obtained.
- Coatings are reproducible and technique is useful for mass production.

b) Spin coating

This process is used to deposit uniform thin films on flat substrate. Generally a small quantity of coating material is applied on the center of the substrate, which is spinning at low speed or not spinning at all. The substrate is then rotated at high speed in order to spread coating material by centrifugal force. While fluid spins off the edges of the substrate, rotation is continued until desired film thickness is achieved. The applied solvent is volatile and it simultaneously evaporates. The thickness of the coating depends on viscosity and concentration of the solution. Higher the speed of spinning, thinner is the film. Spin coating is widely used in deposition of oxide layer using sol-gel precursors. This process is also used in photolithography to deposit layer of photo-resist material.

c) Electrode less deposition

In this method deposition of film is directly done by chemical reaction without application of any electrode potential. Chemical reaction can occur with or without catalyst. This method has been used to deposit several metals, e.g. Ni, Co, Pd, Au etc and oxide films.

The basic principle used here is to have controlled homogeneous precipitation of metal hydroxide and corresponding oxide film is prepared by annealing in air or vacuum [7].

Advantages of this method are,

- It is simple and economical technique.
- Does not require high temperature.
- Large area deposition is possible.

d) Liquid phase epitaxy

This method is used to grow semiconductor crystal layer from melt on solid substrates. This occurs at temperature well below the melting point of deposited semiconductor. The semiconductor is dissolved in melt of another material. At condition close to equilibrium between dissolution and deposition, deposition of semiconductor is fast and uniform. Most used substrates are InP, glass and ceramic. To facilitate nucleation and avoid tension in grown layer the thermal expansion coefficient of the film should match with that of the substrate.

ii) ***Chemical vapor deposition***

The chemical vapor deposition (CVD) techniques are very popular for uniform deposition and coating of complex structures. Some of the CVD based methods are discussed below.

a) Atomic layer deposition (ALD)

In this technique, first the precursor is pulsed into the reaction chamber. Followed by its chemisorption on the surface of the substrate, here it forms a monolayer of the precursor on the substrate. For complete substrate-surface saturation the pulsing time needs to be determined. In the second step, the reactor is purged with an inert-gas to remove the unreacted precursor and in next step; the reactant is introduced into the reactor. The reactant reacts with the first precursor to form the desired material. In the last step the excess of the reactant and some by-products of the reaction are removed by subsequently purging with an inert-gas. The substrate temperature is a very important parameter in the ALD process. Advantages of the ALD technique are a precise film thickness control of the coatings and the possibility to coat substrates of different geometries resulting in conformal coverage. One drawback of this technique is the low growth rate (few Å per cycle), which would need long deposition times if thick films are required. Further, special types of precursors are required that possess a sufficient volatility combined with a high reactivity within the desired deposition process.

b) Metal organic chemical vapor deposition (MOCVD)

Metalorganic precursors are bulky molecules consisting of metal atom attached to organic ligands consisting of carbon, hydrogen and oxygen. The term MOCVD was coined by Manasevit who was the first to describe the use of metalorganic compounds for deposition of semiconductors in the year 1968 [**8**]. Precursors used for MOCVD should have high vapor pressure at low temperatures and higher decomposition temperature otherwise the precursor can undergo premature decomposition and as a consequence result into non uniform coating and blockages in the precursor delivery lines [**9**]. Besides this, the other desirable properties of required precursor are non toxic nature, air stability, easy handling and purity of deposition [**8**].

MOCVD technique has various advantages like low deposition temperature, good conformal coverage, uniform coating of the substrate, possibility of large scale production, ease of compositional control in complex films. Many different types of thin film coatings such as oxides, carbides, borides, nitrides, silicides and chalcogenides can be deposited by MOCVD [**9, 10**].

c) Plasma enhanced chemical vapor deposition (PECVD)

Due to high internal energy state of plasma medium, deposition at lower substrate temperature is possible in PECVD compared to the conventional CVD methods. An early commercial use of PECVD technique was made in deposition of silicon nitride thin films used for the passivation and encapsulation of completely fabricated microelectronic devices. In presence of plasma reaction barrier is reduced and reactions occur at lower temperature hence excess heating of substrates is avoided. Due to reactive plasma species such as ions, electrons, neutrals, radicals a large variety of reaction pathways are available as compared to the thermal CVD techniques. The ions in plasma help in densification of films [**11**].

1.5 Deposition process used in present work

In the present work, capacitively coupled RF plasma enhanced metalorganic chemical vapor deposition technique is used for the deposition of yttrium oxide (Y_2O_3) and yttria stabilized zirconia (YSZ) coatings. Precursor (2,2,6,6-tetramethyl-3,5-heptanedionate)yttrium known as $Y(thd)_3$ is used for deposition of Y_2O_3 coatings while (2, 7, 7-trimethyl-3, 5-octanedionate) yttrium (known as $Y(tod)_3$) and (2, 7, 7-trimethyl-3, 5-octanedionate) zirconia (known as $Zr(tod)_4$) are used for the deposition of YSZ coatings.

The substrates are placed on the heated electrode connected to the RF generator through an impedance matching network. Generation of RF self bias voltage is an added advantage of capacitively coupled RF discharges. The bias level on the substrates during deposition is a crucial experimental parameter since it decides about the energy and flux of ions bombarding the substrates. The detailed experimental procedure is discussed in chapter-2.

Advantages of RF plasma enhanced chemical vapor deposition

- Deposition of insulating coatings is possible which is not possible with DC plasma deposition system.
- The self generated DC voltage on the substrates act as a source of acceleration for the ions leading to uniform and dense film growth.
- Very high level of vacuum is not required for the operation.
- Unlike the microwave ECR plasma deposition process, this deposition technique is tolerant to minor pressure fluctuations.
- The system can be scaled up for industrial purposes.

1.6 Significance of yttria and yttria stabilized zirconia thin films

There are numerous technological applications of these coatings owing to magnificent properties possessed by yttria and yttria stabilized zirconia.

1.6.1 *Yttrium Oxide*

Yttrium oxide is also known as yttria. It is a refractory white ceramic with high melting point 2410 °C. Yttria has a bixbyite structure. Yttria was discovered in the year 1794 by Gadolin in a quarry located at Ytterby in Sweden. It has technologically important properties. It has large optical band gap (5.5eV) so it is transparent from near infrared to ultraviolet region of electromagnetic spectrum. Y_2O_3 has high refractive index (~1.7-2).

Yttrium oxide has high dielectric strength (~3.5 MV/cm), high dielectric constant (9-19) and good lattice constant matching with silicon [**12**].

i) ***Polymorphic forms of Y_2O_3***:

Yttrium oxide exhibits four polymorphic forms,

a) Cubic Y_2O_3 (C-type)**:** This is the stable structure found at ambient conditions with a lattice constant of ~10.6 Å. The structure is similar to CaF_2 structure. Each yttrium ion is surrounded by eight oxygen ions located at eight corners of cube.

b) Cubic Bixbyite structure**:** The distortion in cubic phase produces the fluorite structure, also called as the bixbyite structure with lattice constant ~ 5.2 Å, space group T_h^7 (Ia3). The C-type cubic phase transforms to bixbyite at temperature of 2308 °C. There are 32 yttrium and 48 oxygen ions in unit cell which can be visualized in form of 64 minicubes. Yttrium ions are located at centre of each minicube. Each yttrium ion is surrounded by six oxygen atoms with two of the eight cube corners vacant. As shown in **Figure 1.4, t**here are two different sites, C_{3i} and C_2 from where oxygen ions are missing. In case of site C_{3i} the vacancies are arranged at the body diagonal while for C_2, the vacancies are arranged along the face diagonal [**13**]. A unit cell consists of 8 Y^{3+} C_{3i} sites (25%) and 24 Y^{3+} C_2 sites (75%) with each cation 6-fold co-ordinated. Each yttrium atom is bonded to 6 oxygen atoms in C_{3i} site by equal bond length of ~ 2.28 Å while each Y atom in C_2 site is bonded to 3 pairs of oxygen atoms with three different bond lengths such as 2.243 Å, 2.274 Å and 2.233 Å.

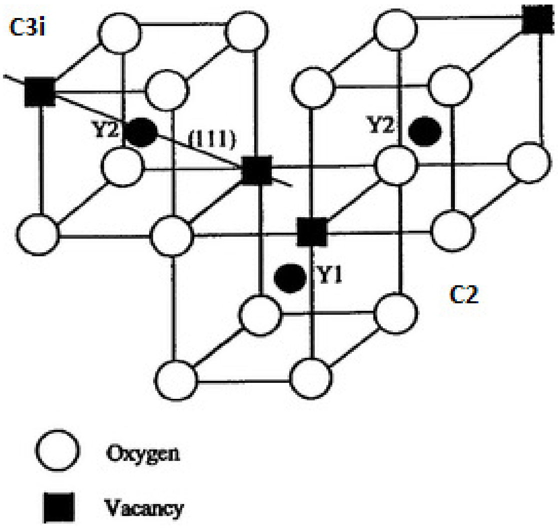

Figure 1.4: Local co-ordination of yttrium ion in bixbyite structure [Ref **14**]

***c) Hexagonal structure*:** The hexagonal (A-type) phase is generally reported at high temperature ~ 2325 °C and has lattice parameters a ~ 3.81 Å and c ~ 6.08 Å [**15**]. It belongs to the space group $P3_2/m1$. Here the yttrium ion is co-ordinated by 7 oxygen ions.

***d) Monoclinic structure (B-type)*:** This phase generally occurs at high pressures having lattice parameters, a ~ 13.91 Å, b ~ 3.483 Å and c ~ 8.593 Å [**15**]. In this phase yttrium ion generally has 6 fold or 7 fold anion coordination. The cubic to monoclinic phase transition occurs at pressure greater than 13 GPa. This transition also occurs at high temperatures. Under high pressure, the cubic crystal will be compressed resulting in shortening of Y-O bond length. The cubic structure loses stability and a high density phase is formed. The covalent nature of bonds increases with decrease in Y-O bond length. The Y-O bond force constant increases by 20%, Y-O-Y by 25% and O-Y-O by 7% [**13**]. There is transformation from cubic to monoclinic phase, when the particle size decreases below 10 nm.

ii) Applications of Yttria

Yttrium oxide has been used for various applications ranging from corrosion and scratch resistant to optics. It is used as protective coating in reactive environments. As yttria is a refractory material with low neutron absorption, it can be used as structural material for nuclear reactors. It is used as component of sintering aids in silicon nitride, alumina and as a stabilizer in zirconia and in alumina-zirconia abrasives. Yttria is also used as high temperature refractory for continuous casting nozzles and as jet engine coatings**.** Due to the presence of oxygen vacancies, in yttrium oxide structure, it is used as oxygen sensor in automobile industry and for stabilization of zirconia [**16**].

Due to high refractive index of Y_2O_3, it is suitable as wave guiding material and a host matrix for doping of rare earth atoms. Eu-doped Y_2O_3 is a typical material well known as a red phosphor used in fluorescent lamps, cathode ray tubes, plasma display panels, field emission displays, etc [**17**, **18**].

Refractive index and band gap are important parameters for optical waveguide devices. Higher value of refractive index enables confined optical transmission in the waveguide, thus increasing the efficiency of pumping and amplification [**19**]. As yttrium oxide is transparent from near infrared to UV region of electromagnetic spectra, it is also used as antireflection and protective coating for optical instruments. Yttrium-iron garnets are used as components in microwave radars for control of high frequency signal. With aluminum oxide, yttrium forms yttrium-aluminum garnet, which is used as solid state laser.

As the size of microelectronic devices is decreasing, search for materials with higher dielectric constant compared to silicon dioxide is gaining ground. Continuous scaling down of complementary metal-oxide semiconductor devices has pushed SiO_2 to its physical limits due to its excessive direct tunneling current. Higher dielectric constant material will facilitate fabrication of layers without allowing leakage current to flow [**20**]. Due to its high dielectric constant and good lattice constant matching with silicon, Y_2O_3 is considered as potential candidate for replacement of SiO_2 as gate material in microelectronic industry **[21].** Y_2O_3 is also used as an epitaxial buffer layer for deposition of high temperature superconductors such as $YBa_2Cu_3O_x$ on silicon. Properties required for the buffer layer are minimal chemical reaction between the two layers, relatively low electrical permittivity and a small lattice mismatch between silicon substrate and the deposited $YBa_2Cu_3O_x$ film [**22**].

1.6.2 *Zirconia*

The most commonly occurring natural form of zirconia is baddeleyite with a monoclinic crystalline structure which was first described in 1892 and named after Joseph Baddley. Zirconium oxide (ZrO_2) is a wide band gap (~5.1 eV) material with high dielectric constant (~18) and is chemically inert [**23**]. Zirconia undergoes phase transformation with temperature and the monoclinic form occurring under ambient conditions is transformed to tetragonal and cubic phases at higher temperatures.

i) *Polymorphic forms of zirconia*

Zirconia exhibits following polymorphic forms,

a) Monoclinic phase

It is the naturally occurring form of zirconia at room temperature and ambient pressure. This structure belongs to $P2_1/c$ space group with lattice constants a ~ 5.156 Å, b ~ 5.191 Å and c ~ 5.304 Å shown in **Figure 1.5**. It consists of four ZrO_2 unit cells with a density of 5.83 g/cc [**16**].

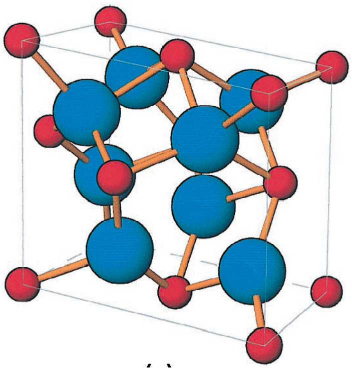

Figure 1.5: Monoclinic ZrO_2 structure [Ref **24**]

Monoclinic to tetragonal phase transition occurs at temperature of 1170 °C. The reverse transformation occurs at 900 °C and is associated with a 4 % volume increase and is martensitic in nature. The martensitic transformation is diffusion less and occurs by co-operative movement of set of atoms across an interface causing shape change and sound. Atoms frequently move less than an interatomic distance and hence nearest neighbors are maintained as far as possible during the change in crystal structure. Generally, there is a temperature hysteresis and polymorphism associated with martensitic transformation [**25].**

b) Tetragonal phase

This structure belongs to $P4_2/nmc$ space group with lattice constants a ~ 3.64 Å, b ~ 3.64 Å and c ~ 5.27 Å shown in **Figure 1.6**. It consists of two ZrO_2 unit cells. The tetragonal phase consists of three forms, t, t' and t".

The t form is undistorted and stable structure. This form can transform directly to monoclinic phase. The t' is metastable and has a distorted cubic structure. In this crystal lattice, alternate columns of oxygen ions are shifted in up or down directions by a small value (δ). This distortion causes four oxygen atoms to move near zirconium atom and four oxygen atoms to move away from the zirconium atom. Each four oxygen atoms form tetrahedra around the zirconia atom. For the t” form, the lattice parameters are same as that of cubic but the oxygen atoms are shifted in up and down direction alternately. Due to shifting of oxygen atoms, two types of tetrahedra are formed one elongated and one shortened giving two nonequivalent Zr atoms in the tetragonal structure. When the particle size of zirconia is small enough, tetragonal phase can be formed at room temperature. The tetragonal to cubic phase transition occurs at 2370 °C [**26**].

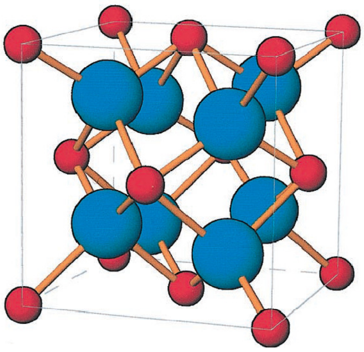

Figure 1.6: Tetragonal ZrO_2 structure [Ref-**24**]

c) Cubic phase

This form exists above 2370 °C. It has a fluorite structure (CaF_2) with space group *Fm*3*m* and lattice constant a ~ 5.15 Å. The crystal structure is shown in **Figure 1.7**.

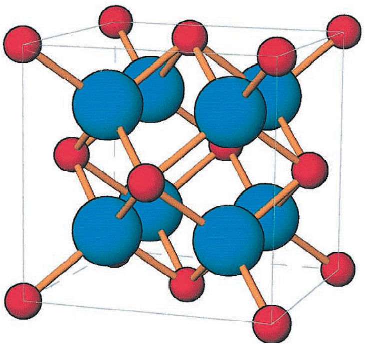

Figure 1.7: Cubic ZrO_2 structure [Ref-**24**]

In this structure each zirconium atom is co-ordinated by eight oxygen atoms and each oxygen atom is tetrahedrally coordinated by zirconium atoms. The fluorite structure remains stable over a range of compositions from Zr_2O_3 to ZrO_2 [**26**].

ii) Stabilization of zirconia

The cubic ZrO_2 does not occur at room temperature due to smaller ionic radius (0.632) of $R_{Zr^{+4}}$ / $R_{O^{-2}}$ than required (0.732) for the eight fold co-ordination [**27**]. The phase transformation with temperature is accompanied by volume change. This renders ZrO_2 coatings useless from technological point of view. To stabilize the high temperature phases at room temperature, zirconia is doped with larger cations to expand the lattice or by doping with lower valence cations, so that oxygen vacancies could be created or combination of both the effects takes place. The oxygen vacancies reduce the average co-ordination number and the oxygen sub lattice relaxes towards cubic symmetry. Some of the dopants used to stabilize zirconia are given below,

a) Trivalent dopants

The solubility of trivalent cations in ZrO_2 depends on the match of cation ionic radii and the similarity of cation and oxygen anion sub lattice between the dopants and ZrO_2.

The structure of rare earth oxides vary with the cation radius. The oxides of La, Ce, Pr and Nd have hexagonal structure. On the other hand, oxides with smaller cation radii such as Sm, Eu and Gd exhibit both monoclinic and cubic form. The interaction of dopants with ZrO_2 lattice is different for different dopants. For example, La^{3+} has a strong tendency to segregate as pyrochlore $La_2Zr_2O_7$. Doping with Pr_2O_3, results in mixtures of tetragonal phases at dopant levels above 15 mol %. Doping with oxides of Nd and Sm results in structural distortion as compared to doping using Gd_2O_3. For oxide of Sc, there is a tendency for segregation of rhombohedral β-phase above 10 mol %. Y_2O_3 has been found to be the best option for high temperature applications. Y_2O_3 as dopant imparts better mechanical and chemical stability to zirconia [**28**].

b) Divalent dopants

Alkaline earth metal oxide dopants such as CaO, MgO create two vacancies per cation. However, the dopant charge mismatch could create structural instability and phase segregation at high temperature.

c) Transition metals and Al^{3+}

Al^{3+}, Fe^{3+}, Cu^{2+} and Ni^{2+} are stable in ZrO_2. But on calcination above 800 ºC, phase segregation occurs and m-ZrO_2 forms on cooling.

d) Tetravalent dopant

Tetravalent cations stabilize cubic phase by expanding the ZrO_2 lattice. So the dopant size must be greater than Zr^{4+} (0.84 Å). Practically, due to low cost and toxicity, CeO_2 is preferred. Formation of cubic phase requires ~ 70 % CeO_2 while for tetragonal phase stabilization 30 % CeO_2 is required. Ce can be preserved as Ce^{3+} through facile Ce^{4+}/Ce^{3+} redox reaction that creates oxygen vacancies in ZrO_2 [**27**].

iii) Stabilized forms of zirconia

Variation of phases with dopant concentration of yttria is shown in the **Figure 1.8**. Depending on yttria content, various phases can be deposited. Below 3 mol % yttria, monoclinic phase is present. In the region from 2-6 mol % yttria content, partially stabilized zirconia is produced. Above 8 mol % yttria, fully stabilized zirconia is formed. Cubic like t” phase (a/c equal to unity) formed at ~ 8 mol % yttria which cannot be distinguished by XRD but have been identified from Raman spectroscopy and electron diffraction studies.

For yttria content between 15-40 mol %, mixtures of cubic Y_2O_3 doped ZrO_2 solid solution and segregated micro domains of $Y_4Zr_3O_{12}$ have been proposed. Crystallization of $Y_4Zr_3O_{12}$ has been observed for yttria content greater than 40 mol % [**27**].

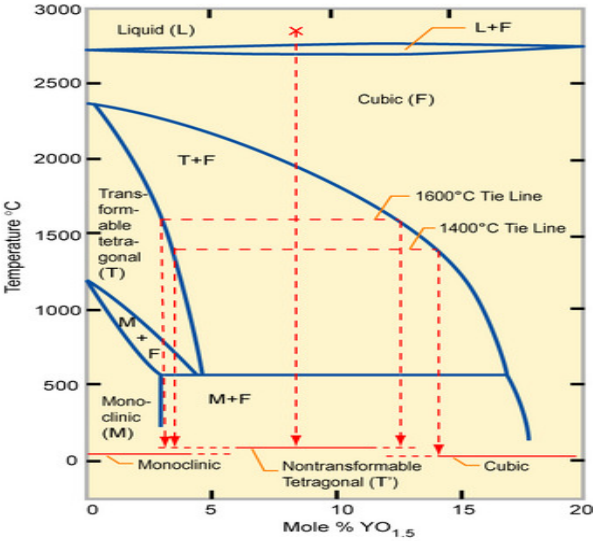

Figure 1.8: Phase diagram of yttria stabilized zirconia [Ref **29**]

a) Single phase polycrystalline tetragonal ZrO_2

Fine grain ZrO_2 (less than 0.5 µm) with small concentration of stabilizing dopant would contain up to 98 % of metastable phase. For this phase, strength increases with decrease in content of monoclinic phase. It has been found that particles with grain size less than 0.3 µm exhibit highest strength and toughness. The grain size effect is controlled by concentration and type of dopant ion, that determines degree of tetragonality (lattice ratio c/a is greater than 0.1) and thermal expansion anisotropy (c versus a direction). In general high tetragonality results in a less stable material. Anisotropic thermal expansion for c and a axis can influence residual strengths in tetragonal grain. Higher residual stress can lower nucleation stress threshold for tetragonal to monoclinic transformation in presence of strain energy. At similar grain size and dopant concentration yttrium is a stronger stabilizer than cerium and titanium. [**30**]

b) Partially stabilized zirconia (PSZ)

Doping zirconia with 3-5 mol % yttria results in mixture of monoclinic and tetragonal phases. Phase constituent studies of zirconia doped with yttria in the concentration range of (2.8-4.0 mol %) indicate two tetragonal zirconia phases with varying degree of tetragonality. Both phases have slightly distorted fluorite structure and differ in the ratio of their lattice parameters. For the t-phase, the c/a ratio ~ 1.1014-1.015 while for other t'-phase the c/a ~ 1.004-1.005 [**31**]. The yttrium rich t' is not transformable while lower yttrium content undergoes martensitic transformation to monoclinic phase under mechanical stress.

Milovichi et al. [**31**] have reported that micro hardness does not change for the different tetragonal phases but there is noticeable decrease in fracture toughness with increasing dopant concentration due to decrease in volume fraction of transformable tetragonal phase. PSZ has high wear and scratch resistance. It has good impact resistance. It is resistant to corrosion, chemical attack and thermal shock. PSZ has high melting point and low thermal conductivity. On application of external stress, the tetragonal phase transforms to monoclinic phase and there is ~ 4 % volume increase. This produces compressive stress in the film, arresting crack propagation and thus imparts fracture toughness to the material.

c) Fully stabilized Zirconia (YSZ)

Zirconia can be stabilized in cubic form at room temperature by addition of ~ 8 mol % Y_2O_3. Some Zr^{+4} ions are replaced by Y^{3+} ions. As Zr has valency +4 and Y has valency +3 so vacancies are generated for charge compensation. One vacancy is generated for every two yttrium ions. YSZ is a solid solution in cubic fluorite structure with yttrium and zirconium on face centered cubic cation lattice (**Figure 1.9**). The oxygen ions and vacancies are located on simple cubic anion lattice. In cubic fluorite structure, each cation is in centre of cube of eight anions and each oxygen ion or oxygen vacancy is in centre of cation tetrahedron. The vacancies become mobile at high temperature ~ 600 °C and act as ion conductor. Cubic YSZ has low thermal conductivity, is chemically inert and brittle [**32].**

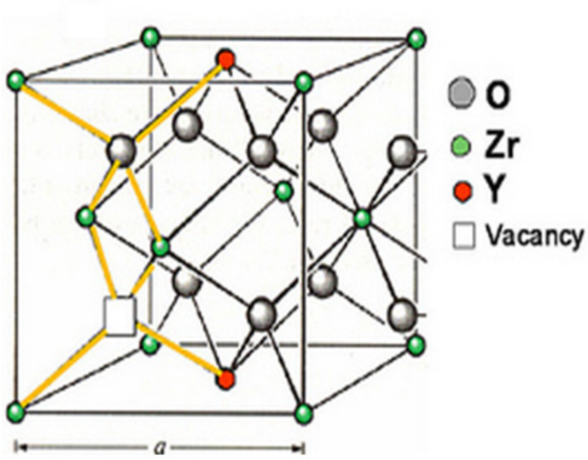

Figure 1.9: Structure of YSZ **[Ref-33]**

iv) Applications of stabilized forms of zirconia

The stabilized forms of zirconia have numerous technological applications.

a) Applications of PSZ

PSZ is used as coating for cutting tools and dies. It is used in manufacture of knives, scissors and blades. As PSZ is wear resistant, it is used for bearings and linings, in pump parts and in grinding media

b) Applications of YSZ

YSZ coatings are used as refractory in jet engines. As it is hard and chemically inert, it is used as tooth crown. YSZ is used as thermal barrier coating in gas turbines. As YSZ is electro ceramic, it is used as solid electrolyte in fuel cells and as sensor to determine oxygen content in exhaust gases and to measure pH value in high temperature water. Cubic zirconia is used in jewellary. YSZ doped with rare earth materials can act as a thermographic phosphor and luminescent material. It is used as a high precision alignment sleeve for optical fiber connector ferrules [**32**].

1.7 Review of Literature

1.7.1 *Yttria based thin films*

Due to the immense technological applications of Y_2O_3, research and development on Y_2O_3 coatings was carried out by various groups. A large variety of deposition processes have been used to deposit yttrium oxide. Literature indicates that Y_2O_3 have been deposited by spray pyrolysis **[34]**, thermal oxidation **[21**], thermal CVD in atmospheric pressure [**35]**, low pressure CVD **[36]**, plasma assisted CVD **[37]**, metal organic CVD [**22**], molecular beam epitaxy **[38]**, atomic layer deposition **[39]**, electron beam evaporation **[40]**, ion beam assisted deposition **[41]**, pulsed laser deposition **[42,43]** and radio frequency sputtering **[44,45]**. Metal-organic precursors have been extensively used for deposition of Y_2O_3 thin films. Deposition of Y_2O_3 thin films by $Y(thd)_3$ metal-organic precursors have been reported earlier by different researchers [**22, 46, 37**, **47**, **48, 49**]. G. Alarcon-Flores et al. [**12**] studied the decomposition characteristics of Y(acac) precursor. Stoichiometric Y_2O_3 deposition with less carbon contamination was reported by T. T. Van [**50**] by ALD process using $Y(thd)_3$. There have been few reports on deposition of plasma enhanced MOCVD of yttrium oxide thin films. Durand et al. [**47**] have used pulsed liquid- injection plasma enhanced MOCVD and studied the interface formation. Varhue et al. [**22**] utilized ECR plasma source and reported deposition of (111) oriented Y_2O_3 films while Barve et al. studied the effect of deposition parameters on the Y_2O_3 thin films deposited by ECR plasma source [**48, 51**]. There are very few reports on RF plasma enhanced MOCVD of Y_2O_3 thin films. for e.g. Niu et al. deposited yttrium oxide thin films using two different precursors, [Y(HFAA)$_3$] and Y(thd)$_3$ by RF plasma enhanced MOCVD and studied the interface formation [**37**]. In this thesis RF plasma enhanced MOCVD of Y_2O_3 thin films is reported. This includes characterization of coatings and correlation of coating properties with the plasma process parameters.

The structure of yttrium oxide was studied both theoretically as well as experimentally by various research groups. The lattice parameter and dislocation density of undoped yttrium oxide single crystal was determined by F. Hanic and co-workers [**52**]. Vibration spectroscopy was extensively studied and assignment of infrared spectra [**53**] and Raman spectra [**54**] was done. The presence of oxygen vacancies in bulk affects the electrical and mechanical properties of Y_2O_3. The study of oxygen vacancies in case of epitaxial grown Y_2O_3 thin films was carried on by A. Travlos et al. [**55**] and it was reported that the oxygen vacancies order in a super structure. The oxygen deficiency results in decrease in electronic gap by 0.8 eV.

The effect of variation of deposition parameters on the properties of Y_2O_3 thin films were studied by different research groups [**22**, **56**]. Cheng et al. [**57**] varied the O_2 pressure and temperature while depositing Y_2O_3 by pulsed laser deposition and found that the crystallinity improved with increase in substrate temperature. The structural transition from monoclinic to cubic phase was observed with increase in temperature by M. -H. Cho et al. [**58**]. Yttrium oxide has bixbyite structure so surface minimization favors growth along (111) direction. It was observed that there is change in orientation from (111) to (100) direction with oxygen partial pressure. The accommodation of internal stress was stated to favor growth along (100) direction [**59**]. Effect of deposition parameters on morphology and preferred growth direction was studied by other groups also [**60**, **61**]. Tustison et al. [**62**] have reported studies on stress developed in Y_2O_3 thin films. The effect of post deposition annealing on the structure and optical properties of Y_2O_3 thin films has been reported stating that there is reduction of defects and enhancement of refractive index as a result of high temperature annealing [**19**].

The optical and structural properties of Y_2O_3 thin films were studied extensively by several researchers [**12**, **44, 63, 43**]. The high refractive index and transparency over a wider range (near IR to UV) makes Y_2O_3 a useful material in field of optics. Rare earth ion doped luminescent materials have acquired significance. Luminescent materials have applications in many devices like lasers, waveguides, fiber-optic amplifiers, X-ray imaging, bioimaging, field emission, electroluminescent displays, etc. Y_2O_3 has high melting point, high thermal conductivity, good chemical stability which makes it a favorable candidate to serve as a laser material [**18**]. It is beyond doubt that the yttrium oxide thin films are promising for optical applications such as phosphors or laser waveguides. Y_2O_3 has been doped with rare earth elements such as Eu, Er, Tb, etc for these applications. Thullium doped Y_2O_3 was reported to produce high fluorescence intensities [**64**]. It is known that nanoparticles exhibit exotic properties that are not seen in the bulk material so their study acquires significance both from fundamental as well as technological point of view. Ramana et al. have reported enhancement in optical properties of nanocrystalline thin films as compared to the microcrystalline films [**65**]. Room temperature ferromagnetism has been reported in Y_2O_3 nanoparticles [**66**]. Tb-doped Y_2O_3 nanoparticles show increase in photo luminescent (PL) efficiency as compared to the bulk [**67**]. However, for achieving better (PL) efficiency and better resolved (PL) spectra, the dopant location and distribution in the host matrix needs to be precisely controlled.

Due to scaling down of microelectronic devices, alternate high dielectric constant materials to replace SiO_2 were sought and research on Y_2O_3 as a gate material gained ground. Due to its high dielectric constant, high electrical strength and good lattice constant matching with silicon, Y_2O_3 proved to be a suitable candidate for this purpose. However, the formation of interfacial SiO_2 layer proved to be detrimental and reduced the effective dielectric constant. Efforts were made to understand [**47**] and reduce formation of SiO_2 layer. For e.g Niu et al. pre-nitrided the silicon surface before deposition of Y_2O_3 [**37**], Durand et al. reported that high flow of reactive species would suppress the formation of SiO_2 interlayer [**47**]. While Chang Ki Lee and Hyung –Ho Park have reported that forming an interfacial yttrium silicate layer reduces the SiO_2 layer formation and improves the electrical properties [**68**].

1.7.2 *Zirconia based thin films*

As fully and partially doped zirconia have numerous technologically important applications, extensive research has been conducted by different groups. Several deposition methods have been reported in the literature for the deposition of Y_2O_3 stabilized ZrO_2 namely DC magnetron sputtering [**69**], pulsed laser deposition [**70**], co-precipitation method [**71**], plasma CVD [**72**], electron beam evaporation [**73**], metal-organic chemical vapor deposition (MOCVD) [**74**].

The type of dopant and its concentration effects on lattice parameter, average crystallite size were studied by Abbas et al. [**75**]. MOCVD of YSZ films with reduced carbon contamination was reported using β-diketonate precursors [**76**].

Besides dopant, other experimental parameters will also influence the deposition of yttria doped zirconia thin films. Effect of variation of deposition parameters on the film properties have been studied by Stamper et al. [**77**]. They studied the texturing of YSZ thin films as a function of substrate temperature and also effect of oxygen annealing on the crystal structure of the deposited films. Qiling et al. studied the influence of oxygen partial pressure and growth rate on refractive index of YSZ thin films [**78**]. Hartmanova et al. observed transition from amorphous phase to cubic phase with substrate temperature but could not observe monoclinic or tetragonal phase. They also measured the ionic conductivity and activation energy and found it equivalent to that reported for the bulk [**73**]. The effect of substrate temperature on optical and structural properties was studied by Boulouz et al. and they reported that substrate temperature has greater influence on pure ZrO_2 as compared to yttria doped films [**79**]. IR analysis was carried on nonstoichiometric yttria stabilized zirconia at elevated temperatures by Liu et al [**80**]. IR transmission spectra of pure and doped ZrO_2 nanoparticles with different particle sizes were measured by Z. Qian et al. [**81**] and observed that nanosized particles show broad and flat absorption bands. Detailed infrared and Raman studies were made on ZrO_2 doped with different yttria concentrations [**82**]. XPS studies were carried by D. Majumdar et al. and observed yttria segregation at the surface of tetragonal phase [**83**].

EXAFS studies were carried in detail by Ping Li et al. They studied the characteristic local structure, effect of yttrium oxide dopant on zirconium oxide structure [**84, 85**]. They have reported that Zr has different local structure in different phases, but the Y local structure remains the same. XANES and EXAFS study was carried in case of nanocrystalline YSZ to study the grain boundaries [**86**]. Martensitic phase transformation in partially stabilized zirconia imparts fracture toughness to the material. A. G. Evans et al. correlated the toughening associated with martensitic transformation with particle size distribution, chemical free energy and strain [**87**]. Technologically important properties of zirconia based films were studied by various research groups. S. Novak et al. have studied the structural changes caused by wear process and arrived on the conclusion that transformation of zirconia is the major wear determining factor [**88**]. M. S. Miller have reported the correlation of properties of PSZ with the deposition parameters [**89**] K. Miyazawa et al. have observed that oxidation resistance of zirconia thin films coated on stainless steel increases by increasing the yttria content [**90**]. S. Heiroth et al. observed that amorphous YSZ layers exhibit higher optical transmissivity, lower bandgap energy, reduced hardness and elastic modulii as compared to the crystalline YSZ [**91**]. Low thermal conductivity of YSZ is utilized for fabrication of thermal barrier coatings. Thermal barrier coatings are used to thermally insulate turbine engine blades from high temperature combustible gases within the gas turbine. These coatings enable higher engine operating temperature, higher thermal efficiency, higher cost effectiveness and longer lifetime for the turbine. Extensive work has been carried out on YSZ for use as thermal barrier coatings [**92**].

1.8 Characterization techniques used

The deposited films are characterized by various characterization techniques. Brief discussion about the characterization techniques used during the course of these investigations is given in this section.

1.8.1 *Infrared (IR) Spectroscopy*

IR spectroscopy is a powerful analytical tool for structural and compositional characterization of materials (both organic and inorganic) and is widely used in areas like material science, catalysis, medicine, biochemistry, forensic science etc. Change in vibrational modes of atoms in a molecule, are greatly influenced by the mass of atoms, their geometrical arrangement and strength of chemical bonds. A molecular vibration is IR active only when the interacting IR radiation causes modulation of molecular dipole moment. Vibration spectra will be observed only in heteronuclear diatomic molecules, as homonuclear molecules have no dipole moment. IR spectroscopy encompasses a spectral region from red end of visible spectrum (12,500 cm^{-1}; 0.8 μm) to microwave (10 cm^{-1}: 1000 μm) of the electromagnetic spectrum. Based upon both application and instrumentation it is conveniently divided into near IR (12500 cm^{-1} to 4000 cm^{-1}), mid-IR (4000 cm^{-1} to 400 cm^{-1}) and far IR (4000 $cm^{-1}$to 10 cm^{-1}) regions. The most fundamental molecular vibrations occur in mid-IR making this region richest in chemical information while overtones and combination of fundamental vibrations especially those involving hydrogen appear in the near-IR. On the other hand far IR region pertains to vibrations involving heavy atoms, lattice modes of solids and some rotational absorption of small molecules.

Currently most modern IR absorption instruments use Fourier Transform techniques with a Michelson interferometer. Unlike conventional IR instruments, in FTIR instrument all the frequencies are used simultaneously to excite all the vibration modes of different types of bonds/linkages present in the sample. This reduces the experimental time considerably. With these advantages measurement of transmission, reflection or even emission spectra has become significantly faster and with higher sensitivity than before.

1.8.2 ***X-ray photoelectron spectroscopy (XPS)***

XPS is a non destructive surface analysis technique probing a depth of ~10 nm of the sample. It is one of the three widely used electron spectroscopy techniques where X-ray photons, typically of the range 1200-1500 eV, knock out the electron from solid surfaces. The kinetic energy of the photoelectrons is measured with a suitable analyzer and detector. The kinetic energy of the emitted electron is given by equation no.(1.2), where E_k is the measured kinetic energy, $h\gamma$ is the energy of X-ray, E_b is the binding energy of the electrons in the solid and ϕ is the work function of the spectrometer (order of 4.5 eV).

$$E_k = h\gamma - E_b - \phi \qquad (1.2)$$

The X-ray source and spectrometer work function values are incorporated in the data acquisition software and finally the spectrum is displayed as binding energy against photoelectron peak intensity. The energy values of the photoelectrons are characteristic of elements. The quantification of elements is possible by measuring the peak area corresponding to the element and knowing its sensitivity factor. The binding energy and shape of the photoelectron peak can be analyzed precisely to find the chemical states of elements and their quantitative composition within the electron parameter depth of the solid.

It is found that photoelectron intensity depends on incident X-ray flux, number of atoms of the element of interest, cross-section of ionizing level, probability of no-loss escape of electrons, acceptance solid angle and detection of the instrument.

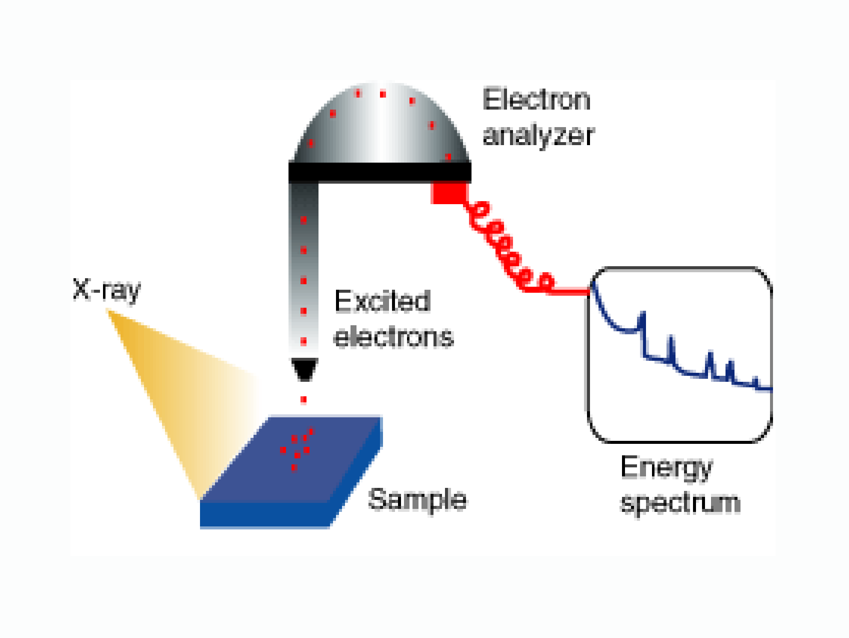

Figure 1.10: Schematic of XPS set-up [Ref **93**]

1.8.3 *Atomic force microscopy (AFM)*

AFM measures the topography of conductors, semiconductors and insulators with a force probe located within few Å of the sample surface. The main components of an AFM instrument are probe, piezoscanner and detection system. The probe used in AFM consists of a flexible cantilever and sharp tip. Depending on the sign of electrical voltage applied the piezoelectric scanner expands or shrinks, which is proportional to the voltage. The scanning is carried out by moving the sample under the tip by means of piezoscanner.

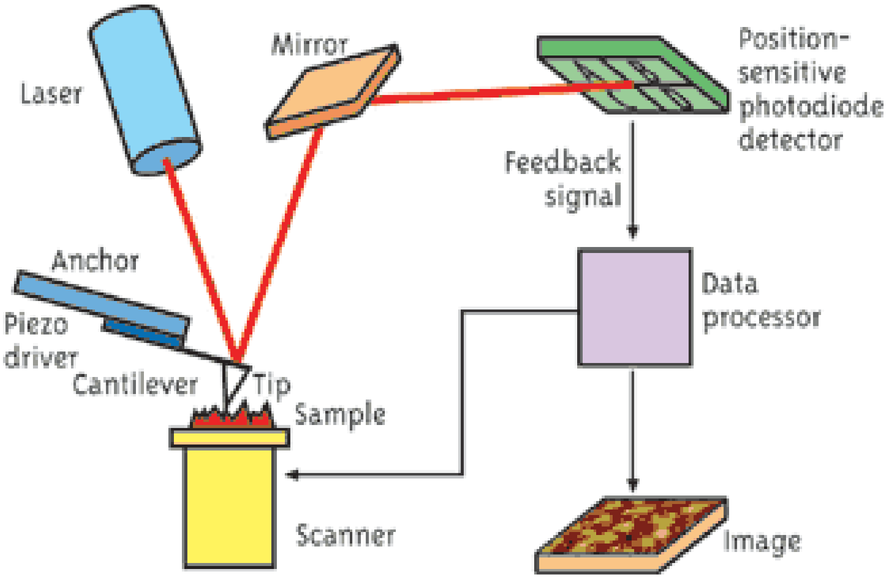

Figure 1.11: Schematic of AFM set-up [Ref **94**]

There are mainly two types of AFM modes, namely, the contact mode and semi contact/tapping mode, which are used for imaging the samples. In the contact mode, the force between the probe tip and substrate is repulsive and it is within the range of 10^{-8} to 10^{-7} N. The contact mode can obtain higher atomic resolution than the other modes but it may damage a soft material due to excessive tracking forces applied by the probe on the sample. Therefore soft cantilevers are used. In tapping mode the main interaction force between the probe tip and the sample is the Van der Waal's force and it is in the range of 10^{-10} to 10^{-12} N. Here, cantilever oscillates in the attractive region and its oscillation frequency gets modulated depending on the sample surface features. The probe tip is 5 to 150 nm above the sample surface. The resolution in this mode is limited by the interaction with the surrounding environment. In the tapping mode, rigid cantilevers are used. Use of sharper probe results in images with good resolution. Three dimensional surface imaging and determination of surface roughness is possible with AFM.

1.8.4 *X-ray diffraction (XRD)*

X-ray diffraction techniques are fundamental in understanding the structure of material under study. Better understanding of the structure further opens pathways for analyzing the properties exhibited by the material. X-ray diffraction principle is governed by Bragg's law (equation-1.3) which states that when X-rays of wavelength (λ) is incident on the surface with the interplanar spacing (d) of order of 1-100 Å , constructive interference of the diffracted rays gives rise to maximum intensity at certain angle (θ) which is called the Bragg's angle.

$$n\lambda = 2\mathrm{d}\sin\theta \qquad (1.3)$$

Where, n is integral multiple of λ

Generally for study of bulk material, θ-2θ (Bragg-Brentano) reflection geometry is used. Here the incidence angle is equal to the diffracted beam angle with respect to the sample surface. The device configuration enables high intensity diffracted beam from any particular set of crystalline planes to be focused on a slit in front of rotating detector. However, for greater angle of incidence, the X-rays can penetrate depths of few to several hundred micrometers inside the material. In case of thin film analysis, the beam penetration depth can be greater than the thickness of the film resulting in diffraction pattern dominated by the substrate peaks. By using grazing incidence configuration, the XRD measurements become more sensitive to the surface region of the film and the substrate contribution is minimized. In case of grazing angle X ray diffraction (GIXRD), a parallel monochromatic X-ray beam is incident on the sample at a fixed angle less than 2-3 degree and diffraction profile is recorded by detector scan only. By using this technique information regarding thickness, phase, change in composition with depth and microstructure can be obtained.

1.8.5 *Spectroscopic Ellipsometry*

Ellipsometry was first developed by Drude in the year 1887. Ellipsometry is an optical technique that measures change in polarized light upon reflection or transmission from the sample. When linearly polarized light is reflected from the sample, the perpendicular (s-) and parallel (p-) components experience a different attenuation and a phase shift according to the Fresnel equations. Therefore the reflected light is elliptically polarized as seen from **Figure 1.12**. This technique measures the amplitude ratio (Ψ) and the phase difference (δ) between (p-) and (s-) polarized light waves. When (Ψ) and (δ) values are obtained by scanning the wavelengths generally in UV/ visible region, variation of optical properties is obtained. Measurements in IR region have also been reported. Complex refractive index(ρ) for the sample is given by equation,

$$\rho = \frac{r_p}{r_s} = \tan(\Psi) e^{i\delta} \qquad (1.4)$$

Where r_p and r_s are the complex Fresnel reflection coefficients of the material for the p- and s- polarized light.

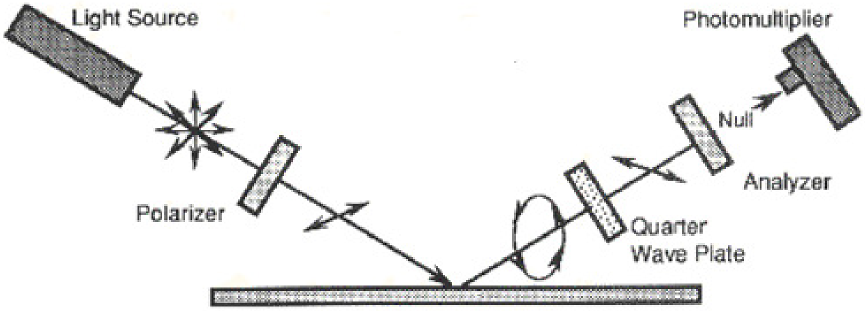

Figure 1.12: Schematic of Ellipsometry set-up [Ref **95**]

Spectroscopic ellipsometry is a non destructive and fast measurement technique. Advantages of this technique are high precision and thickness sensitivity (~ 0.1 Å). Determination of film thickness and optical constants is possible. Disadvantages are requirement of optical model in data analysis and difficulty in characterization of low absorption coefficient (< 100 cm^{-1}). The spot size of beam is typically several millimeters, leading to low spatial resolution of measurement.

1.8.6 ***Scanning electron microscopy (SEM)***

SEM is a non destructive technique that reveals information regarding the morphology of the material. In this technique high energy electrons (30-40 keV) are incident on the sample. Interaction of electron beam with sample surface emits secondary electrons (~ 50 eV) that are detected by appropriate electronics and analyzed further. In conventional SEM instruments, electron beam is thermionically emitted from electron gun fitted with a filament. Filaments are generally made of tungsten or lanthanum hexaboride. The filament is heated by passing electric current through it. When heat generated is greater than the work function of the material, electrons are liberated. Thermionic sources have relatively low brightness; there can be evaporation of cathode material and thermal drift during operation.

The use of field emission scanning electron microscope (FESEM) which is advanced type of SEM can avoid these problems. The field emission gun is usually a tungsten filament fashioned in shape of sharp tip. The emission is achieved by placing the filament in a high electric field gradient. The sharp tip of the filament (~100 nm) helps in concentrating the electric field such that the work function of the material can be overcome and there is emission of electrons. In case of FESEM variable apertures are used to refine the beam, smaller objective aperture sizes will produce images with spatial resolution 3 to 6 times better than conventional SEM. High quality, low voltage images are obtained with minimal charging of the sample. This eliminates necessity of coating insulating samples with a conducting layer.

1.8.7 *Energy dispersive X-ray analysis (EDAX)*

EDAX is complementary to SEM. The qualitative / quantitative measurement of elemental composition present in the sample is obtained by EDAX. This technique operates on principle of detection of characteristic X-rays emitted by atoms of elements when electron beam interacts with the sample. The basic components of EDAX are X-ray detector, pulse processor (to measure voltage corresponding to X-ray energies) and a computer. The size of voltage pulse is proportional to energy of X-rays. Elemental distribution maps or elemental line profiles can be obtained by EDAX.

1.8.8 *Scratch adhesion testing*

The scratch adhesion testing is used to determine the cohesive and adhesive strength of the samples by measuring the critical loads at which failures occur in the sample. In this method, a diamond indenter is drawn on a coated surface under increasing load (either stepwise or continuous) until at particular load known as critical load (L_c), where failure event occurs. If the failure event represents loss of coating-substrate adhesion then critical load is used as a qualitative measure to determine the coating substrate adhesion. However, in practice a range of failure modes can occur, some are dependent on adhesion, while others are dependent on plastic deformation and fracture within the coating. The study of these failure modes is important in assessing coating quality for tribological applications. The scratch track is studied with the help of reflected light microscopy and scanning electron microscopy.

1.8.9 *Stylus Profilometer:*

A stylus profilometer is an instrument used to measure the surface profile of thin films. Measurement of surface roughness and film thickness is done by using stylus profilometer. A diamond stylus is moved along the surface of the film at a constant velocity for a specified distance and under a specified force. The curvature of the diamond tip is typically 10 µm. The film is masked during deposition stage so that a step is formed. The step height is measured by the pickup system and recorded as the thickness of the film. A typical profilometer can measure small vertical features ranging in height from 10 nm to 1mm. The height position of the diamond stylus generates an analog signal which is converted into a digital signal stored, analyzed and displayed. The radius of diamond stylus ranges from 20 nm to 50 µm, and the horizontal resolution is controlled by the scan speed and data signal sampling rate. Smaller the tip radius of the stylus greater is the accuracy in the measurement.

1.8.10 *X-ray absorption Spectroscopy (XAS):*

When the incident X-ray energy matches the binding energy of the electron of atom within a sample, there is increase in absorption of X-ray. Here an absorption edge is observed due to drop in transmitted X-ray intensity. Each element has a set of unique absorption edges corresponding to different binding energy of electrons. The X-ray absorption spectrum is divided into two regions (**Figure 1.13**) namely, X-ray absorption near edge spectroscopy (XANES) and extended X-ray absorption fine-structure spectroscopy (EXAFS).

XANES is the region including pre-edge and the absorption peak. It is strongly sensitive to formal oxidation state and coordination chemistry of absorbing atom. While EXAFS deals with the measurement of fine structures in the X-ray absorption spectra from 50 to 1000 eV above the absorption edge of the atoms in a material.

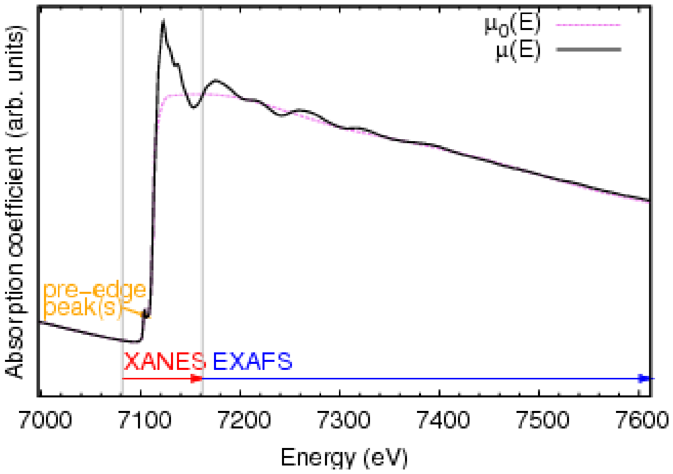

Figure 1.13: Absorption coefficient versus energy spectrum [Ref **96**]

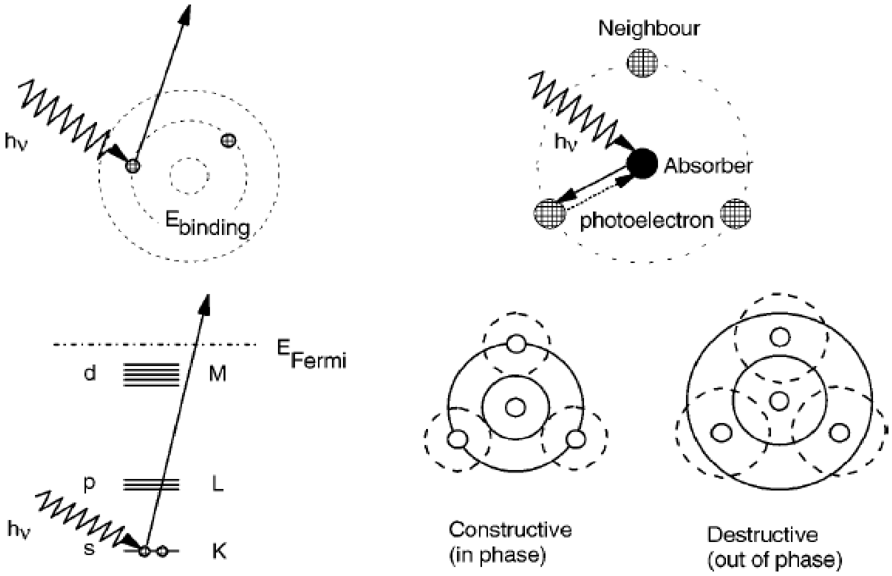

Figure 1.14: EXAFS principle [Ref **98**]

The interference of outgoing photoelectron with the scattered wave from surrounding atoms causes EXAFS (**Figure 1.14**). The regions of constructive and destructive interference are respectively seen as maxima and minima giving rise to oscillations in EXAFS. The fine oscillatory structure in the X- ray absorption spectra of a particular species of atom gives precise information regarding the radial arrangement of atoms around that element, the number and nature of neighboring atoms. With the advent of modern bright synchrotron radiation sources, this technique has emerged out to be most powerful for local structure determination which can be applied to any type of material viz. amorphous, polycrystalline, polymers, surfaces and solutions [**97**]. As synchrotron sources are bright, concentration of absorbing element required for analysis can be in few ppm.

1.8.11 *Thermo gravimetric analysis (TGA)*

In TGA, the weight of the sample is recorded as a function of time as temperature is increased at a controlled uniform rate. Loss of water of crystallization or volatiles is revealed as weight loss. Oxidation or adsorption of gas shows up as weight gain. TGA instrument consist of a high precision balance with a furnace programmed for linear rise of temperature with time. Sample is then heated either in inert atmosphere or vacuum.

1.9 Scope of work/ thesis

Since plasma is a dynamic medium having immense potential applications, the interaction of plasma with surfaces becomes complex. Considering the various technological applications of yttria and yttria stabilized zirconia coatings, deposition of these coatings with plasma medium assumes significance. There are various process parameters of capacitively coupled RF plasma enhanced MOCVD such as the choice of substrates, the nature of precursors, deposition pressure, oxygen partial pressure, distance between the electrodes, substrate temperature, temperature at which the precursors are heated and the self bias. All of these parameters affect the properties of the deposited films. It then becomes important to study the effect of these process parameters on the properties of deposited films to gain knowledge about the experimental conditions under which film with desired properties can be obtained. The correlation of some of these deposition parameters such as the self bias, precursors, temperature of precursors with the properties of the deposited films was done and understanding is sought on the role played by these key parameters in determining the physical and chemical properties of yttria and yttria stabilized zirconia thin films.

Thesis organization

The thesis is organized into seven chapters.

Chapter 1 gives a brief introduction about the oxides under study namely yttrium oxide and yttria stabilized zirconia. The chapter includes brief discussion on plasma, different types of plasma sources, application of plasma sources, various physical and chemical methods for thin film deposition. The different structures exhibited by Y_2O_3 and YSZ, their properties and applications are also discussed. A brief literature review on both the oxides is included along with description of working principles of different characterization techniques used.

Chapter 2 includes detailed experimental procedure for the deposition of Y_2O_3 and YSZ thin films by RF plasma enhanced MOCVD method. This chapter also includes short discussion on metalorganic precursors, mechanism of RF discharge and generation of RF self-bias voltage.

Chapter 3 gives details on deposition of Y_2O_3 thin films by RF plasma enhanced MOCVD method using $Y(thd)_3$ precursor. This chapter includes discussion on the effect of variation of RF self-bias (applied to the substrates) on the properties of Y_2O_3 thin films studied by using different characterization techniques.

Chapter 4 includes discussion regarding EXAFS and AFM analysis of Y_2O_3 thin films deposited using $Y(thd)_3$ precursor under the varying influence of RF bias on the substrates. This chapter highlights the correlation of EXAFS data with the properties of Y_2O_3 thin films obtained by various characterization techniques.

Chapter 5 includes comparative study on Y_2O_3 thin films deposited by RF plasma enhanced MOCVD using two different metalorganic precursors, namely, $Y(thd)_3$ and $Y(tod)_3$. The structure and properties of the films are studied and compared using different characterization techniques.

Chapter 6 illustrates the deposition of yttria stabilized zirconia thin films by RF plasma enhanced MOCVD process using $Zr(tod)_4$ and $Y(tod)_3$ precursors. Discussion on effect of variation of yttria content on the deposited phases and properties of deposited thin films is given in this chapter.

Chapter 7 includes summary and highlights the important conclusions and findings of the investigations reported in this thesis.

Chapter 2

Experimental Details

This chapter describes about the experimental details regarding the deposition of yttrium oxide (Y_2O_3) and yttria stabilized zirconia (YSZ) thin films by radio frequency plasma enhanced chemical vapor deposition (RF-PECVD) using metalorganic precursors. The chapter is divided into four sections. The first section describes the various metalorganic precursors that are used and their advantages. The second section gives details regarding the deposition system. Third section describes the significance of RF self-bias on the substrates during deposition. Deposition procedure for yttrium oxide and yttria stabilized zirconia coatings along with the cleaning procedure of the substrates is given in fourth section.

2.1 Metalorganic precursors

Generally, metalorganic precursors are compounds with a direct metal-carbon bond (sigma or pi). However precursors containing metal-oxygen, metal-nitrogen bond and even metal hydrides are also grouped under this category [**99**]. The decomposition of the precursor determines purity of the precursor and deposition rate of the films [**99**]. One of the major problems associated with metalorganic precursor is incorporation of carbon in the deposited film [**100**]. The way the precursor reacts can be modified by changing the ligands so that high purity, higher deposition rate can be obtained at lower temperature. Generally, it is observed that weak M-XC bond in precursor helps to reduce the amount of carbon incorporation in the deposited film. Intermolecular electrostatic forces tend to make the ionic molecules and polar molecules involatile. Larger the molecule, more it is polarizable, hence less is the volatility. However, larger ligands shield the metal centre and thus improve volatility. So a compromise has to be achieved between effectively isolating the metal center and avoiding too large ligands [**99**].

Efforts are focused in the direction for developing suitable precursors for MOCVD satisfying the required properties. Precursors for MOCVD can be classified into four categories; metal alkoxides, metal alkylamide, metal alkyls and metal β-diketonates.

Alkoxides: These compounds have higher vapor pressure than β-diketonates but are less stable. This results in lowering of deposition temperature. They are more susceptible to water and oxygen. Oligomerization is a chemical process resulting into finite degree of polymerization of monomers. To inhibit oligomerization in metal alkoxides containing large, highly positively charged metal atoms, bulky ligands such as tert-butoxide must be used. This helps in preparation of volatile mononuclear alkoxide. However, these precursors contain unsaturated four-co-ordinate metal centers and tert-butoxide ligand undergoes a catalytic hydrolytic decomposition reaction in presence of trace water. These complexes therefore are air and moisture sensitive. This limits their shelf-life.

Alkylamides: These compounds have been found good for deposition of both metal nitride and metal oxide thin films. The carbon and nitrogen impurities were found to reduce by increasing the substrate temperature and flow rate of oxygen during deposition.

β-diketonate: These compounds are known for their volatility and thermal stability. Oligomerization can be controlled by steric bulk of ligands, manipulation of Lewis acid-base reactions by intramolecular donor sites or by additional ligands.

The β-diketonate precursors are used for the current work as they satisfy most of the required properties. They are easy for handling, non toxic, non corrosive and have high vapor pressure usually 1-10 torr in 100-300 °C temperature range [**101**]. In the present study, (2,2,6,6–tetramethyl-3,5-heptanedionate) yttrium (commonly known as $Y(thd)_3$) and (2, 7, 7-trimethyl-3, 5-octanedionate) yttrium (known as $Y(tod)_3$) are used for deposition of Y_2O_3 while $Y(tod)_3$ and (2, 7, 7-trimethyl-3, 5-octanedionate) zirconia (known as $Zr(tod)_4$) are used for deposition of YSZ. The precursors were synthesized by ultrasound method. The details of precursor synthesis are given elsewhere [**102, 103**]. The thermo gravimetric analysis (TGA) on $Y(tod)_3$,$Y(thd)_3$ and $Zr(tod)_4$ precursors recorded at a pressure of 10^{-2} mbar is shown in **Figure 2.1(a)** , **2.1(b)** and **2.1(c)** respectively.

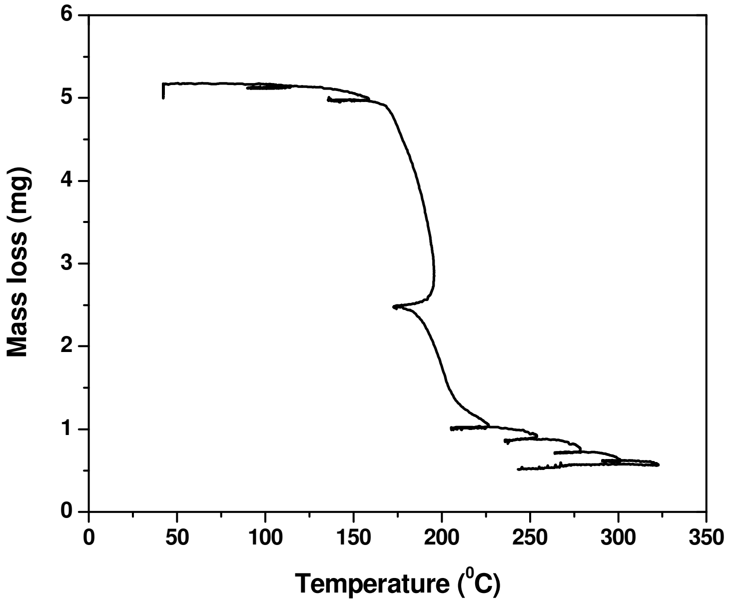

Figure 2.1(a): TGA plot of $Y(tod)_3$

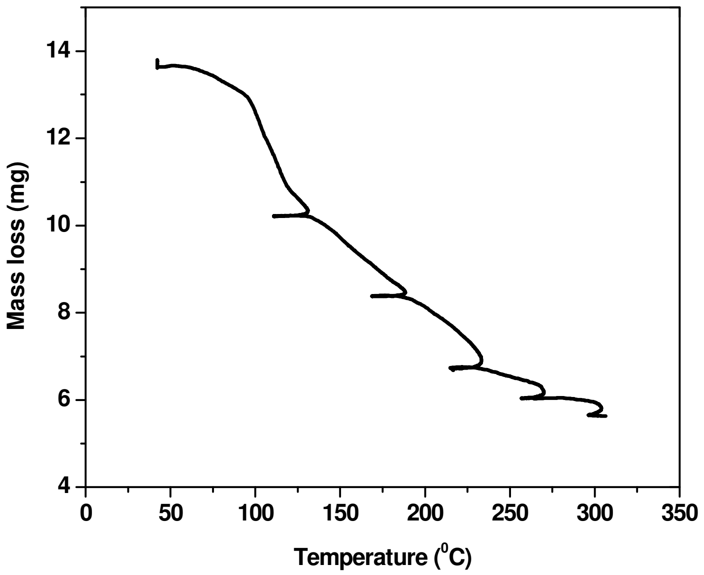

Figure 2.1(b): TGA plot of Y(thd)$_3$

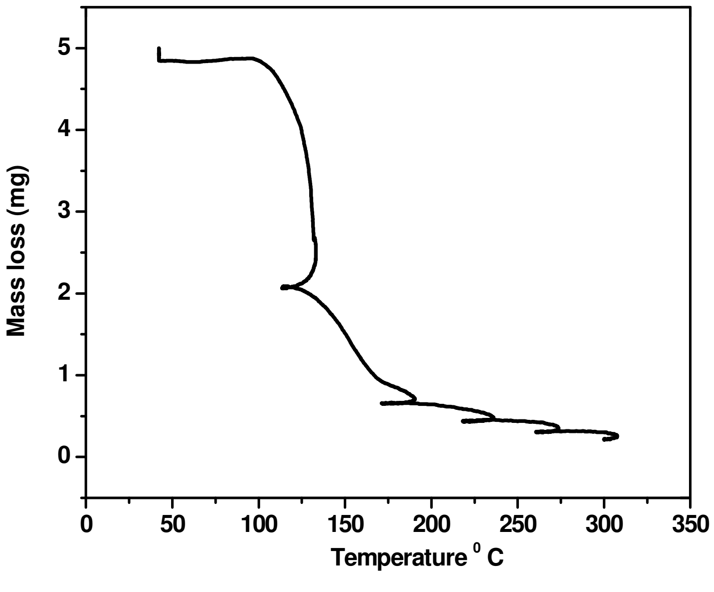

Figure 2.1(c): TGA plot of Zr(tod)$_4$

2.2 Deposition System

The schematic of the deposition system is shown in **Figure 2.2**.

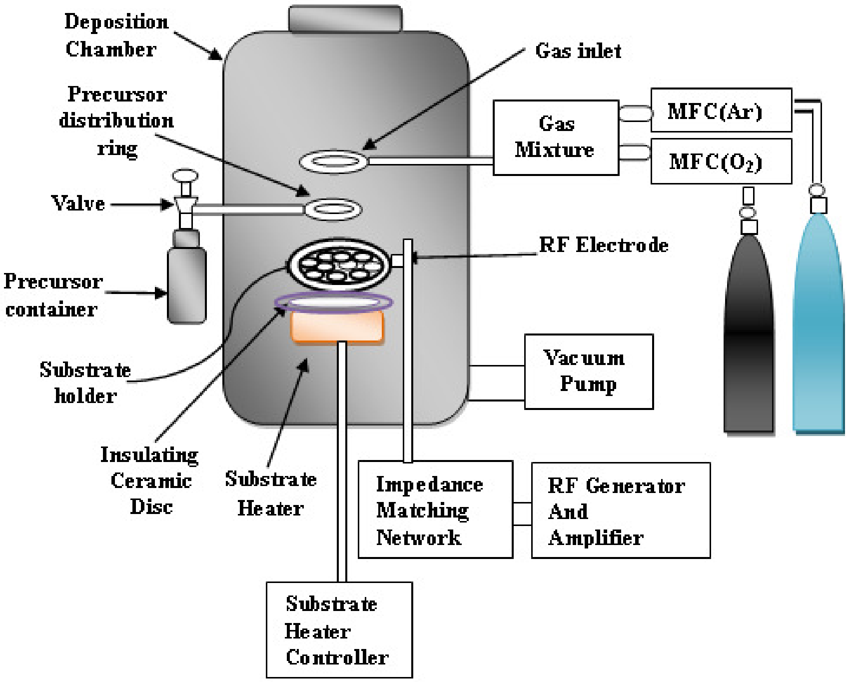

Figure 2.2: Schematic of deposition system for yttrium oxide thin films

The deposition is carried out in a cylindrical stainless steel chamber of 40 cm diameter and 50 cm height. The deposition chamber consists of a RF electrode and a substrate heater (capable of achieving a temperature of 700 °C) separated by a 3 mm thick ceramic ring. The ceramic ring acts as an isolator between the live RF electrode and grounded heater surface. The RF electrode is a S.S. plate with a concentric circular groove. This plate is fixed to a S.S. cylindrical rod; the other end of the rod terminates in a female type RF connector. The substrate holder is a circular S.S. disc with perforations in the form of mesh that fits into the groove of the RF electrode plate. The electrode and the heater arrangement along with the ceramic ring can be moved in the vertical (Z) direction.

The precursor vapors are fed into the deposition chamber by a heated S.S. tube of 6.35 mm diameter. The precursor vapors are fed into the plasma as a shower by a S.S. ring that has perforations for uniform distribution of the precursor. Argon and oxygen gases are fed separately into the deposition chamber. The flow of these gases into the plasma chamber is controlled by mass flow controllers. The substrates are placed on the RF electrode. Distance between the substrates and the precursor distribution ring is kept as 4 cm during all depositions that are reported here. The precursor powder was pressed into pellets using a mechanical press. The precursor pellet is placed inside the S.S. container. The container is connected to precursor delivery line (S.S. tube) with a gate valve in between. The gate valve helps in controlling the flow of precursor vapors. The precursor delivery tube and precursor distribution ring are kept heated during the deposition to avoid condensation of the precursor in the delivery line. This helps in avoiding unnecessary blockage and ensures uniform flow of precursor vapor into the deposition chamber. The flow rate of the precursor vapors can be controlled by varying the temperature of the precursor container. The heating of substrates, precursor delivery tube and precursor distribution ring is achieved using a programmable heater controller.

RF signal generator (make-Rhode & Schrawz) along with a dual stage amplifier is used to apply power to the substrates through impedance matching network. Industrially allocated frequency of 13.56 MHz is used. The circuit diagram for the impedance matching network is shown in **Figure 2.3**. This circuit consists of a parallel capacitor (C_1) and a series inductor (L). A series capacitor (C_2) acts as a blocking capacitor. The LC circuit matches the impedance of the chamber to the impedance of the RF generator (50 ohm). The blocking capacitor (C_2) stores charge and provides the DC self bias voltage. The self bias voltage is measured by an analog DC voltmeter (0-500 V). The capacitor and inductor values are determined with the help of Smith chart. Introduction to Smith chart and details regarding design of impedance matching network from Smith chart is given in Annexure I.

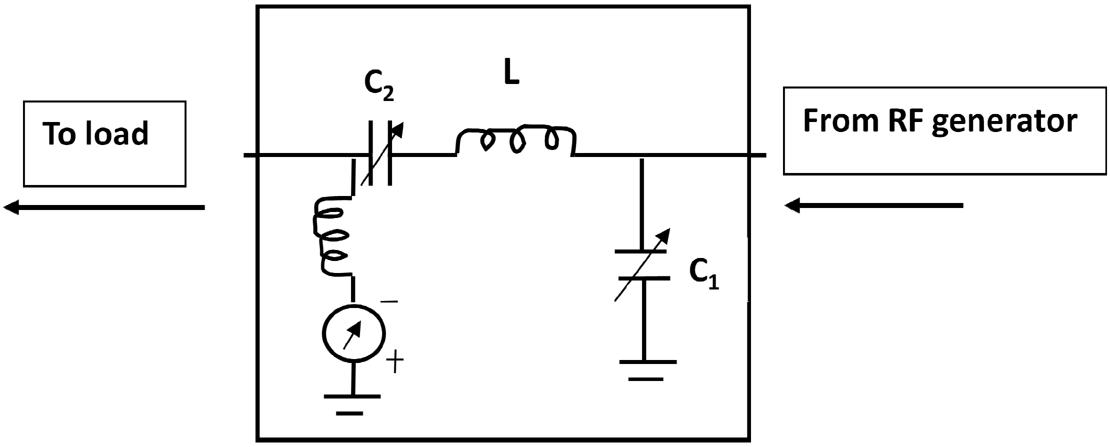

Figure 2.3: Impedance matching network

2.3 RF discharge

The process of RF discharge is collision dominated phenomena. In case of DC discharge, the electron can continuously gain energy, till it has sufficient energy to ionize the gas atom. However, in RF discharges the electrons can accelerate during half cycle and decelerate during the other half. Hence collisions play an important role, since after gaining maximum energy; the electron should transfer its energy to neutral atom. To achieve this condition, the pressure should be such that there should be probability of collision of neutral atom and electron, after electron has gained sufficient energy from the oscillating field. At low pressure, electron will keep on gaining and losing energy from the field, but the probability of collision will be less, as a consequence the breakdown field will increase. At high pressures, the collisions will be frequent and electrons will not be able to gain sufficient energy from the field thereby leading to rise in the breakdown field strength. Therefore minimum field strength occurs at a condition where the collision frequency (υ_c) approximately equals the angular frequency (ω) of the oscillating field. The maximum amplitude of electrons (x) should be smaller than the chamber dimension (L) such that, $x \approx L/2$. Beyond this limit, the charged particles will hit the chamber walls and present a major source of loss to the system [**5**].

The RF self bias plays a very important role as a deposition parameter. It is generated basically due to the different response time of ions and electrons to the varying high frequency (13.56 MHz) AC field. During the positive half cycle electrons are attracted to electrode and the blocking capacitor (C_2) gets charged. During the consequent negative cycle, ions being sluggish cannot respond to the high frequency field and lag behind. Thus, in subsequent cycles, as the ions lag behind and due to high mobility of electrons, the blocking capacitor gets negatively charged and a self bias DC voltage is generated. The self bias dictates the energy of the impinging ions on the substrate and associated fragmentation of the precursors. The bias voltage involves both ion energy and ion flux. The energetic ions enhance surface migration and help in desorption of loosely bound species leading to uniform and dense film growth. The energy of bombarding ions thus decides the plasma chemistry and hence influences the properties of the deposited films. However high bias voltage levels can lead to resputtering or introduce distortions in the structure of films. The compressive stress developed is directly proportional to the bias value. The optimum bias voltage required will depend on the nature of material to be deposited and the type of application being focused on [**104**]. Depending on the dimensions of electrode and deposition system, the power required to achieve a particular bias voltage will vary. For a given system, bias increases with power supplied and decreases with the pressure in the chamber.

2.4 Deposition Procedure of Y_2O_3 and YSZ thin films

The substrates used for deposition were silicon (100), quartz, stainless steel and tantalum. The average roughness values of uncoated substrates were 1.5 nm (silicon), 1.7 nm (quartz), 0.03 μm (stainless steel) and 0.05 μm (tantalum). Silicon wafer was cut with the help of diamond cutter into pieces of required dimension. The dimension of quartz and tantalum coupons was 1cm x 1 cm. Mirror polished 10 cm diameter steel discs were also used as substrates.

Silicon substrates were cleaned with standard RCA cleaning procedure. This procedure consists of following steps,

i. Organic clean: The substrates were placed in solution of $H_2O:H_2O_2:NH_4OH$ in proportion of 5:1:1 and kept heated at 75 °C for 20 minute. Insoluble organic contaminants are removed. Then substrates are rinsed ultrasonically in de-ionized (DI) water for 15 minute.

ii. Ionic clean: Then substrates are heated in a solution of $H_2O:H_2O_2$: HCl in proportion of 6:1:1 at 75 °C for 20 minute. This removes ionic and heavy metal atomic contaminants. Then the substrates are rinsed ultrasonically in deionised water for 15 minute.

iii. Finally, the silicon substrates are dipped in solution of H_2O: HF in proportion of 50:1 for few seconds and then rinsed in deionised water for 15 minute.

The RCA procedure does not attack silicon and only a thin layer of silicon dioxide is removed.

The quartz, tantalum and stainless steel substrates were first washed with soap solution to remove traces of machining oil and then ultrasonically cleaned in de-ionized water. This was followed by ultrasonic rinse in methanol for 20 minutes. All the substrates were dried with help of IR lamp before transferring to the chamber.

After placing the cleaned substrates on the RF electrode, the chamber along with the precursor container and gas delivery lines were evacuated to a base pressure of 1 x 10^{-2} mbar using a rotary vacuum pump. The precursor container was then slowly heated to a desired temperature. The delivery lines and precursor distributor ring were also heated to avoid condensation of precursor in its path (this is necessary to achieve proper flow of precursor without any blockage in the delivery lines). The substrates were then heated to a temperature of 350 °C with the help of substrate heater. Prior to the deposition, the substrates were sputter cleaned using plasma of argon gas at a substrate bias of -125 V for 20 minutes. For deposition, plasma of argon (2 sccm), oxygen (10 sccm) and precursor vapors was used. Argon being a heavy atom assists in fragmentation of bulky precursors and bombarding of the growing film surface. The bombardment also helps in removal of loosely bonded species, resulting in film densification. Additional oxygen supply during deposition results in films with good stoichiometry and decrease in carbon incorporation [**76**]. All depositions were carried out for time duration of 60 minutes.

2.4.1 Deposition of Y_2O_3 coatings

Using the above procedure, yttrium oxide thin films were deposited. Two sets of studies were carried out regarding the deposition of Y_2O_3 coatings.

i) Effect of RF self bias on the properties of the Y_2O_3 thin films: To study the effect of RF self bias on the properties of the films, a series of six films were deposited by varying the self bias voltage on the substrates from -50 V to -175 V in steps of -25 V keeping all other experimental parameters same. The precursor used was, (2,2,6,6-tetramethyl-3,5-heptanedionate)yttrium known as $Y(thd)_3$. The actual experimental details and characterization of the deposited films are discussed in chapter 3.

ii) Comparison of heptanedionate and octanedionate precursors: Yttrium oxide thin films were deposited using two different metalorganic precursors, viz, $Y(thd)_3$ and $Y(tod)_3$ by process of RF plasma assisted CVD described above. The discussion on experimental deposition parameters and characterization of the thin films are discussed in chapter- 5.

2.4.2 Deposition of Yttria stabilized zirconia coatings

The schematic of the deposition system for deposition of YSZ thin films is shown in **Figure.2.4**.

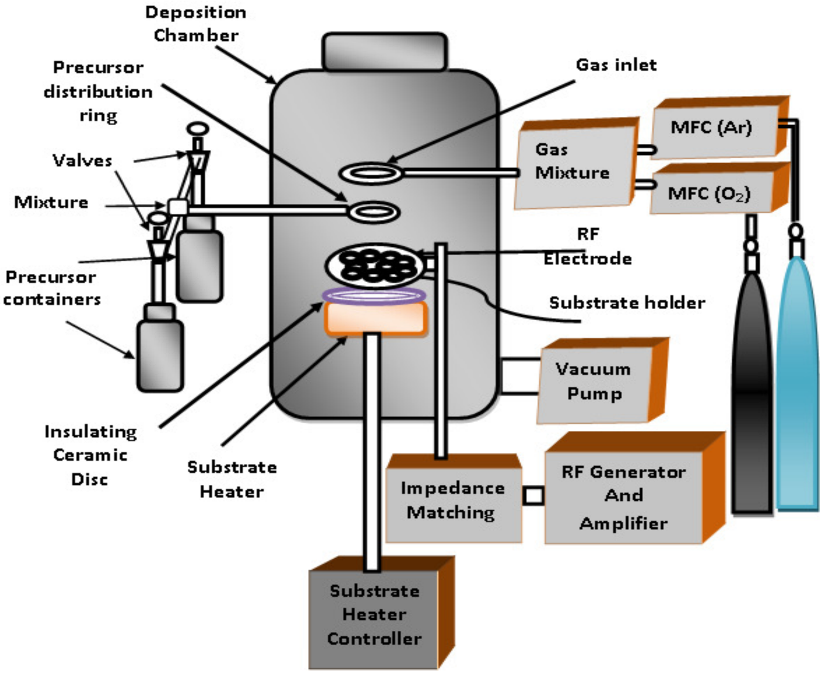

Figure 2.4: Schematic of deposition system for YSZ thin films

The deposition system for YSZ coatings is similar to that of the Y_2O_3 coatings except that there are two separate precursor containers. For deposition of YSZ coatings, (2, 7, 7-trimethyl-3, 5-octanedionate) yttrium (known as $Y(tod)_3$) and (2, 7, 7-trimethyl-3, 5-octanedionate) zirconia (known as $Zr(tod)_4$) are used. $Y(tod)_3$ and $Zr(tod)_4$ powders are placed in pellet form in two separate containers. The deposition procedure is similar to that of Y_2O_3. Here $Zr(tod)_4$ is kept at constant temperature of 220 °C and three different films are deposited by maintaining the temperature of $Y(tod)_3$ containing precursor at three different temperatures; 110 °C, 130 °C and 160 °C to study the associated phase changes with variation of yttria content in the films. Three films were deposited by varying the yttria content in the films. The effect of variation of yttria content on the properties of zirconia is studied and details are discussed in chapter-6.

Chapter 3

Deposition and Characterization of yttrium oxide (Y_2O_3) thin films

This chapter describes about the deposition of yttrium oxide thin films by RF plasma enhanced MOCVD technique using $Y(thd)_3$ precursor. Keeping all other experimental parameters constant, the RF self-bias on the substrate is varied during deposition. The effect of RF self-bias on the substrates on the properties of Y_2O_3 thin films is studied by using different characterization techniques.

3.1 Introduction

The properties of yttrium oxide thin films depend upon the deposition procedure used. Various deposition parameters such as oxygen partial pressure, nature of the precursor, flow rate of precursor, substrate morphology and deposition time will define the properties of the deposited thin films. The surface morphology, roughness and refractive index are closely related to the structure, internal stress and defects [**105**]. Earlier, researchers have varied the deposition parameters and studied effect on the properties of Y_2O_3 films. For instance, Cheng et al. have studied the effect of substrate temperature and oxygen pressure variation during deposition of Y_2O_3 by pulsed laser deposition [**57**]. There are very few reports [**37, 20**] on Y_2O_3 deposition by RF plasma enhanced MOCVD and effect of systematic RF self-bias variation on the properties of Y_2O_3 thin films has not been reported. In the present chapter, the effect of RF self-bias variation on the properties of Y_2O_3 thin films is discussed. The self bias on the substrate is a reliable parameter since it involves both energy and flux of the ions. Bombarding the film surface with energetic ions can lead to film densification. But beyond a certain bias level, with increase in bombarding energy of ions, there can be undesirable effects like re-sputtering, increase in compressive stress or structural distortions in the films

[**104**]. Hence, study of effect of bias variation on the substrates on the properties of Y_2O_3 acquires significance. The generation mechanism of RF bias on the substrate is already discussed in chapter 2. The significance of self bias in the deposition process is highlighted in the previous chapter.

3.2 Experimental details for deposition of yttrium oxide thin films under influence of varying bias

To study the effect of RF bias (on the substrate) on the properties of Y_2O_3 thin films, the RF self bias is varied in steps of -25 V starting from -50 V to -175 V. A series of six thin films were deposited at, -50 V (film A), -75 V (film B), -100 V (film C), -125 V (film D), -150 V (film E) and -175 V (film F) bias. All other experimental parameters were kept constant. A (2,2,6,6–tetramethyl-3,5-heptanedionate) yttrium commonly known as $Y(thd)_3$ precursor heated at 190 °C is used for the deposition. This precursor has a vapor pressure of 0.5 mm Hg at 95 °C [**22**]. The TGA plot showing the vaporization characteristics for the $Y(thd)_3$ precursor is given in chapter-2 (**Figure 2.1** (**b**)). Silicon (100), quartz and tantalum substrates were used for deposition. The detailed cleaning procedure of substrates and schematic of deposition system is given in chapter 2 (**Figure 2.2**).

After placing the cleaned substrates on the RF electrode, the chamber along with the precursor container and gas delivery lines are evacuated to a base pressure of 1×10^{-2} mbar pressure using a rotary vacuum pump. The delivery lines (170 °C) and precursor distributor ring (190 °C) are heated to avoid condensation of precursor in its path (this is necessary to achieve proper flow of precursor without any blockage in the delivery lines). The substrates are then heated to a temperature of 350 °C with the help of programmable heater controller.

Prior to starting the deposition, the substrates are sputtered cleaned using plasma of argon gas (flow rate 5 sccm) at a substrate bias of -125 V for 20 minutes. The precursor container is then slowly heated to a temperature of 190 °C. For deposition, plasma of argon (2 sccm), oxygen (10 sccm) and $Y(thd)_3$ vapors is used. Depositions are carried out by varying the substrate bias (-50 V to -175 V in steps of -25 V) levels by keeping all other parameters constant. All depositions were carried out for time duration of 60 minutes. The final operating pressure was ~ 2 x 10^{-2} mbar.

.

3.3 Characterization of yttrium oxide thin films

To study the effect of bias variation on the properties of Y_2O_3 thin films, the deposited coatings were characterized by GIXRD, XPS, FTIR, FESEM and spectroscopic ellipsometry. GIXRD was carried out using a Cu K_α radiation source and Bruker D8 Discover model. The incident (grazing) angle was fixed at 1.8°. The scans were taken in 2θ range of 10°-90° with scan step of 0.02° per 3 second. XPS was done with SPECS Gmbh spectrometer with Phoibos 100 MCD energy analyzer. The scans were taken with Al K_α (1486.6 eV energy) with a pass energy of 22 eV. Infrared spectra were recorded in the region of 120-600 cm^{-1} at 4 cm^{-1} spectral resolution using Bruker Vertex 80 V FTIR spectrometer configured with KBr and Mylar multilayer beam splitters and liquid nitrogen cooled DTGS detectors. An 11° reflection accessory was used for the measurements. FESEM was done by using Carl Zeiss make, model no. ULTRA 55. Ellipsometric studies were carried out with a phase modulated spectroscopic unit (model UVSELTM 460 ISA JOBIN-YVON, SPEX) in the range 300-1200 nm. Thickness measurement was done using (make- Dektak, model- 150 Veeco) stylus profilometer. The characterization results obtained are as follows.

3.3.1 *Thickness measurement*

Thickness values of films measured by stylus profilometer are given in **Table 3.1**. It is seen that film thickness varies with substrate bias during deposition and is maximum for film B.

Film	**Bias (Volt)**	**Thickness (nm)**
A	-50	140
B	-75	250
C	-100	65
D	-125	200
E	-150	108
F	-175	75

Table 3.1: Thickness measurement results on deposited films at various RF self bias voltages

3.3.2 *Spectroscopic Ellipsometry*

Figure 3.1 shows the variation of the refractive index with wavelength for the films that are deposited at different bias levels. All films show a fairly constant refractive index in the wavelength region of 600-1200 nm. As wavelength decreases below 600 nm, refractive index increases monotonically as reported in the literature [**43**]. The refractive index and extinction coefficient are actually related to band gap absorption and the behavior of optical constants in case of Y_2O_3 represent behavior of wide band gap insulators [**105**]. There is a change of refractive index of the deposited films with bias.

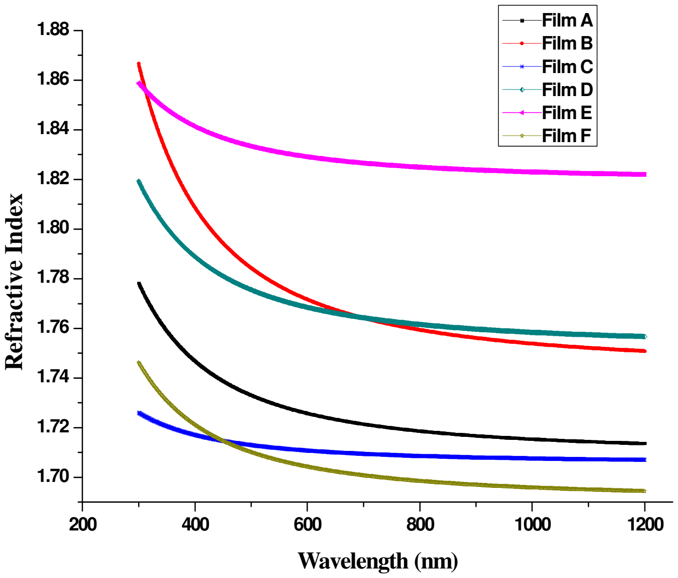

Figure 3.1: Variation of refractive index for films deposited at different RF self bias voltages

Film E shows the highest refractive index 1.83 at 500 nm wavelength followed by films B, D, A, C and F. The values of refractive index obtained are in agreement with the literature values and slightly less than the value for the bulk i.e. 1.947 at 500 nm. Yan et al. have reported refractive index value of 1.85 at 500 nm [**105**]. Wang et al. have studied the change of refractive index at three different annealing temperatures for films deposited by RF magnetron sputtering and observed that the refractive index increases with annealing temperature, supporting the argument that high temperature annealing results in release of voids and increases the mobility of atoms of the films resulting in formation of more close packed thin films enhancing the refractive index [**19**]. Zhang et al. deposited Y_2O_3 by pulsed laser deposition at two different temperatures and found the value of refractive index to be independent of temperature [**43**]. In the present study, for all the films extinction coefficient is zero in the wavelength range (300-1200 nm), indicating that all the films are transparent in the investigated wavelength range as shown in **Figure 3.2**.

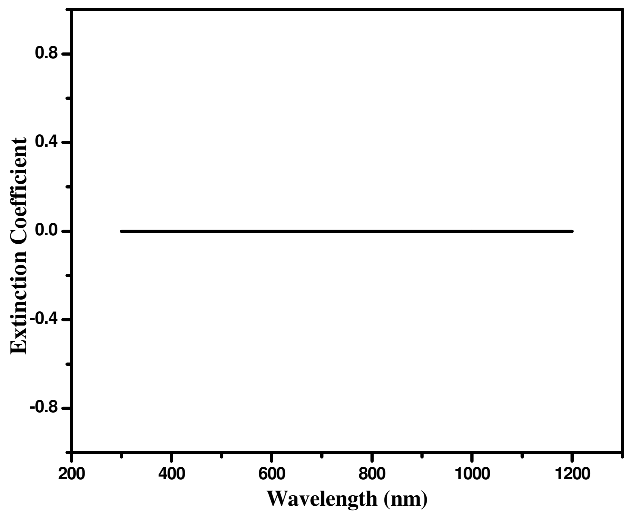

Figure 3.2: Variation of extinction coefficient for films deposited at different RF self bias voltages

3.3.3 *Grazing incidence X-ray diffraction (GIXRD)*

The GIXRD patterns taken on the films are shown in **Figure 3.3**. From the X-ray diffraction patterns, it is seen that the films A, B, C and D show deposition of Y_2O_3 with BCC structure. The diffraction lines corresponding to (222), (400), (440), and (622) reflections as indicated in JCPDF card No: 79-1716 do match well with the observed pattern. Films E and F that are deposited at higher bias level on the substrate show no preferred orientation and indicate that they are losing crystalline nature with the increase in the bias level (i.e. with the increase in the energy of the ions that are arriving at the substrates). Film A exhibits growth along (100) and (111) directions. While films B and D show texturised growth along (111) direction, film C show texturised growth along (100) direction. However earlier researchers had reported amorphous Y_2O_3 deposition at a substrate temperature in the range 350-450 °C by using plasma enhanced chemical vapor deposition [**37**].

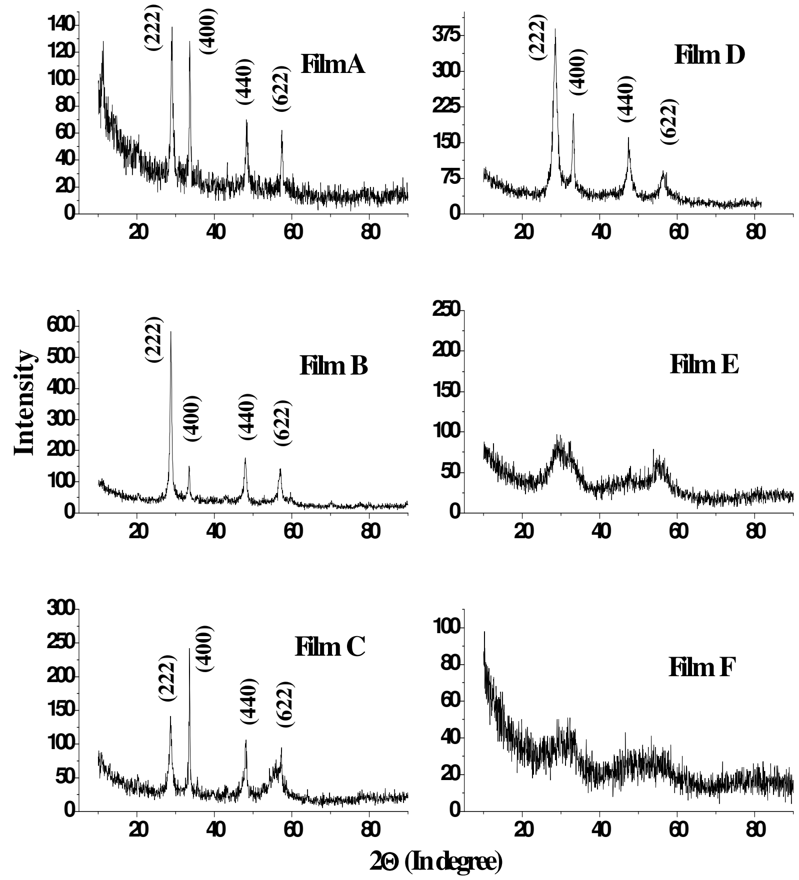

Figure 3.3: X-ray diffraction pattern for films deposited at different RF self bias voltages.

H. Fukumoto et al. have reported that the crystalline orientation of the films does not depend on substrate orientation. They observed that growth of (111) oriented Y_2O_3 is possible both on Si (100) and Si (111) but growth of Y_2O_3 (100) was not directly possible on Si (100). The co-ordination of yttrium ion was stated as the reason for this behavior [**106**]. Gaboriaud et al. have stated that amorphous SiO_2 interfacial layer may result in growth direction of Y_2O_3 not being influenced by the orientation of silicon substrate. The chances of

SiO_2 layer formation are enhanced as growth is carried in presence of oxygen at elevated temperature [**17**].

3.3.4 *X-ray Photoelectron Spectroscopy (XPS)*

The XPS scans were taken with pass energy of 22 eV. Peaks corresponding to Y 3*d*, O 1*s* are scanned in detail with 0.1 eV scan step. These peaks are deconvoluted by using XPS Peak fit 4.1 program. Details about the deconvoluted peaks are given in **Table 3.2**.

XPS peak	χ^2	**G:L ratio**	**FWHM (eV)**
Y 3*d*	1 to 2	5	<1.8
O 1*s*	1 to 2	15	<1.8

Table 3.2: Details of XPS peak deconvolution

The binding energy shifts were corrected using binding energy of physiadsorbed carbon at 284.6 eV as reference **[58]**. There are various reasons for shifting of binding energy, such as presence of electric field, charge transfer effect, environmental charge density and hybridization. Binding energy shift due to charge transfer occurs when removing a valence electron results in increase in core electron's potential. Y 3*d* deconvoluted peaks for films deposited at different RF self bias voltages are shown in **Figure 3.4**. The Y 3*d* core level is getting split into doublet (Y 3$d_{5/2}$ and Y 3$d_{3/2)}$ due to spin orbit coupling. The doublet has energy separation of 2.1 eV and Y 3$d_{5/2}$ to Y 3$d_{3/2}$ areal intensity ratio is 1.5 [**107**].

Three different chemical environments are found for the yttrium atoms in all films. Peak pair with binding energy at ~156.8 eV and ~158.8 eV correspond to stoichiometric yttrium oxide, peak pairs with binding energy at ~157.8 eV and ~160 eV could be either Y-OH or Y-OC bonds. Y-OC will shift the Y 3*d* doublet to higher binding energy due to higher electro negativity of carbon [**47**]. Peak pairs with lower binding energy ~155.8 eV and ~158 eV indicate presence of reduced yttrium oxide [**49**]. This suggests that there is a small degree of nonstoichiometry on the surface of the films and the degree of nonstoichiometry changes with the bias voltage.

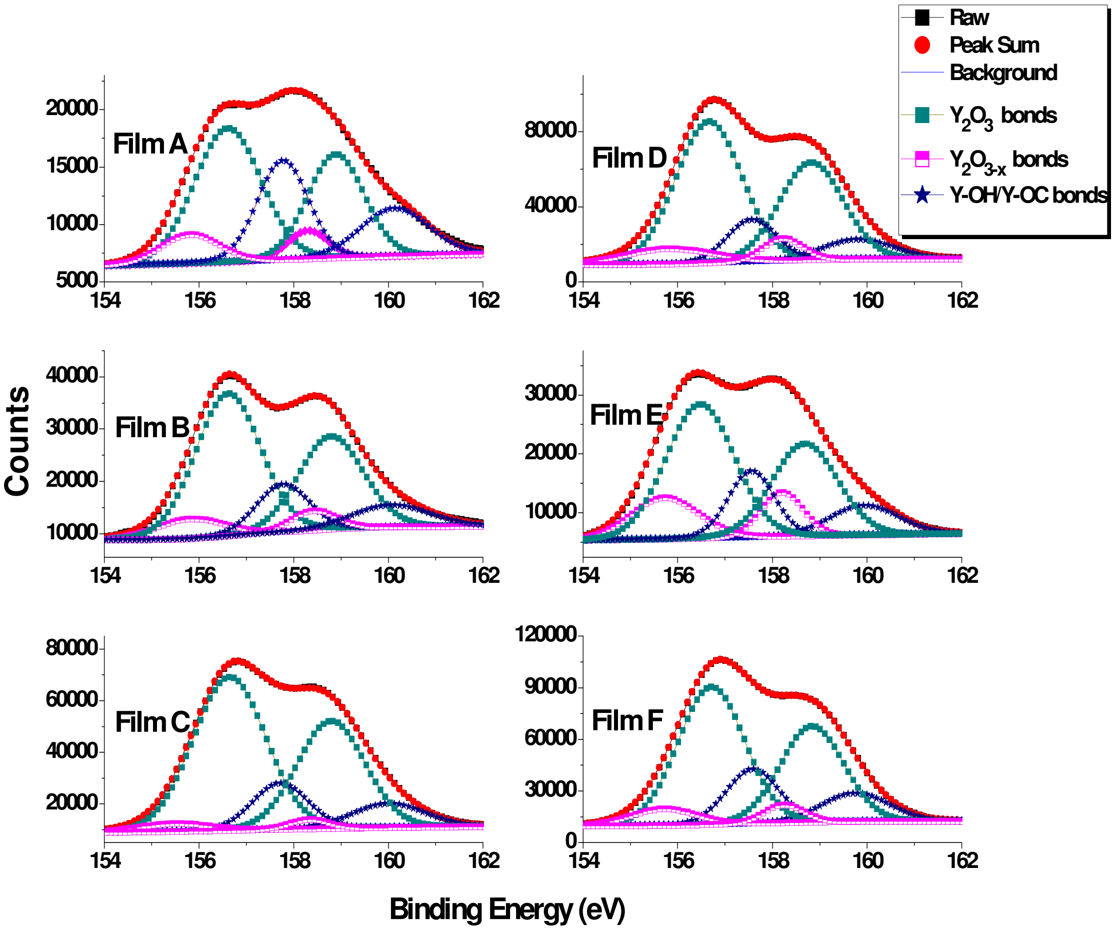

Figure 3.4: Y 3*d* detailed XPS scans for films deposited at different RF self bias voltages

Deconvoluted O 1*s* peaks for the films deposited at different RF self bias voltages are shown in **Figure 3.5**. The O 1*s* peak is deconvoluted into four sub peaks with binding energy, 529 eV, 530 eV, 531 eV and 532 eV corresponding to stoichiometric yttrium oxide, reduced yttrium oxide, O-C=O bond and C=O bond. For film E, peak corresponding to binding energy of 528.5 eV correspond to Y-OH bond [**63**]. As Y_2O_3 is hygroscopic in nature, it absorbs moisture from the atmosphere and reacts to form hydroxide and carbonates. Since in situ sputtering of the sample surfaces prior to XPS scan was not done (to avoid modification of thin film surface) it can be seen that along with stoichiometric Y_2O_3 there exists small amounts of yttrium hydroxide and reduced yttrium oxide in all films [**49**].

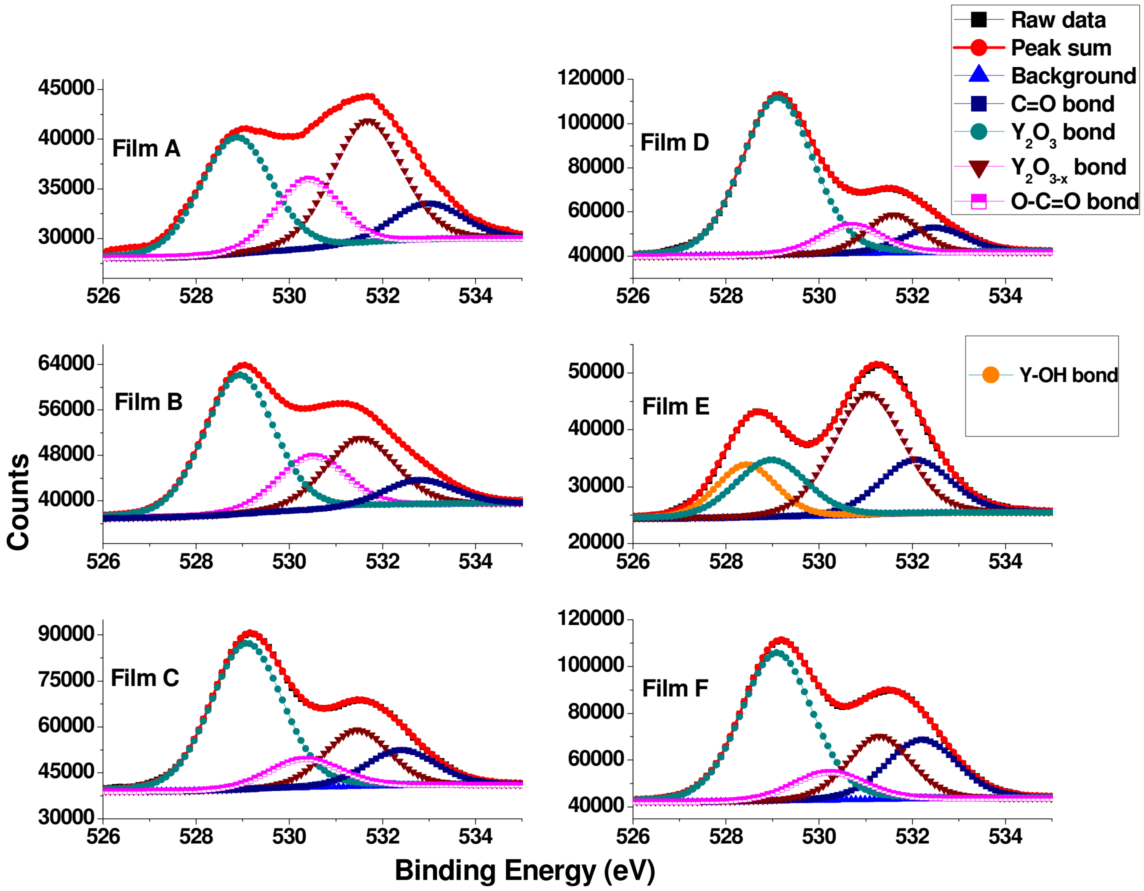

Figure 3.5: O 1*s* detailed XPS scans for films deposited at different RF self bias voltages

Film	**%Y_2O_3 content**	**%Y_2O_{3-x} content**	**%Y-OH/Y-OC content**
A	57.15	10.9	31.8
B	70.29	10.6	19
C	77.8	4.10	18.06
D	73.37	10.6	16.03
E	61.02	18.8	20.16
F	69.89	8.33	21.77

Table 3.3: Semi quantitative analysis (by XPS) of film surfaces from Y 3*d* peak.

Since moisture and carbon species are adsorbed on the surface of the film, quantitative analysis based on XPS from O 1*s* and C 1*s* peaks may not represent the actual bulk composition of films. Hence, semi quantitative analysis (shown in **Table 3.3**) is done only by taking into consideration Y 3*d* peak [**48**]. Semi quantitative analysis from Y 3*d* peak indicate that degree of stoichiometric Y_2O_3 on the surface is increasing with bias and amount of yttrium carbonate is decreasing. However at bias levels above -100 V there is a decrease in degree of stoichiometric Y_2O_3 and slight increase in amount of yttrium carbonate. It is observed that for all deposited films extent of non-stoichiometry and amount of yttrium carbonate on the surface is very small as compared to the quantity of stoichiometric Y_2O_3.

3.3.5 *Infrared Spectroscopy*

The Far-IR reflectance spectra taken on the films are shown in the **Figure 3.6**.

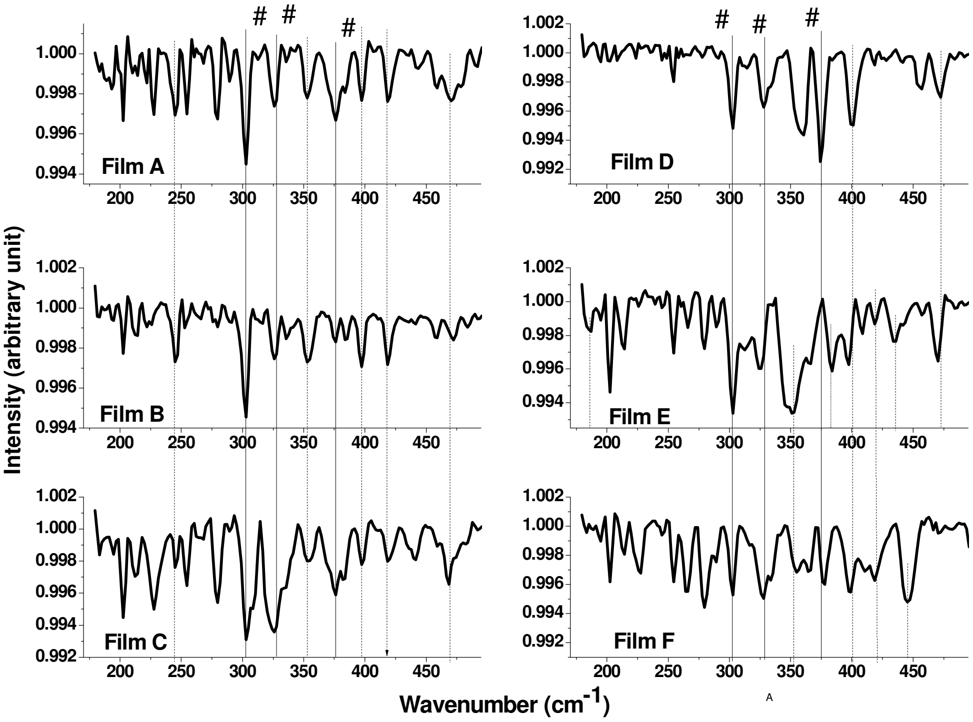

Figure 3.6: Far IR reflectance spectra of Y_2O_3 thin films deposited at different RF self bias voltages.

The triplet consisting of peaks at 305 cm^{-1}, 330 cm^{-1} and 375 cm^{-1} confirm the presence of cubic yttrium oxide [**46**]. Additional peaks for cubic yttrium oxide are present at ~185 cm^{-1}, 243 cm^{-1}, 383 cm^{-1}, 395 cm^{-1} , 420 cm^{-1}, 435 cm^{-1}, 445 cm^{-1}, and 468 cm^{-1} [**54,53,108**]. The triplet is intense for film B and film D as compared to other films. As IR is a bulk technique the intensity of IR peaks will be directly proportional to the thickness of the film.

3.3.6 *Field Emission Scanning Microscopy*

The surface microstructures of the deposited films along with the transverse cross sections for films A-F as seen by SEM are given in **Figures 3.7** and **3.8** respectively. It is seen that the microstructure of the films is changing with the applied bias.

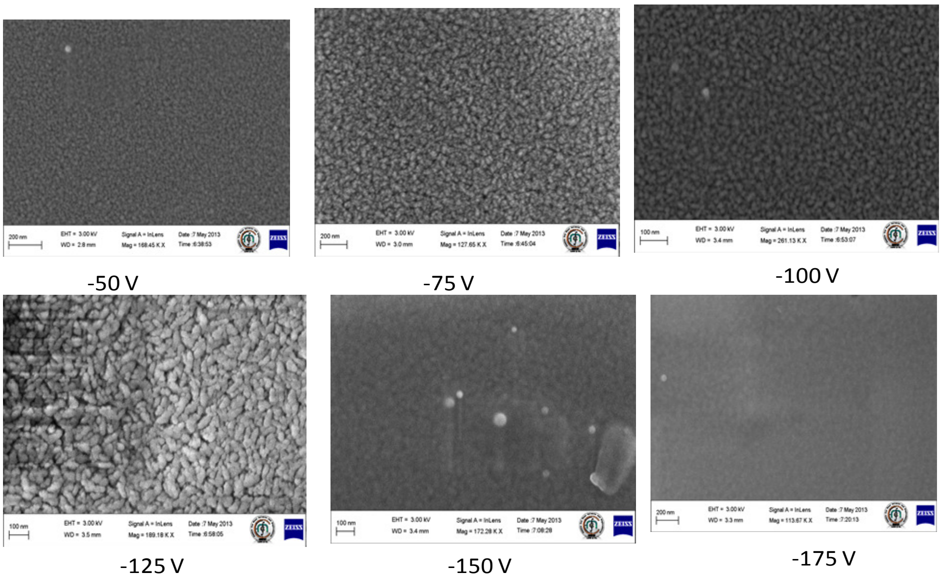

-50 V -75 V -100 V

-125 V -150 V -175 V

Figure 3.7: SEM images showing surface microstructures of the deposited films

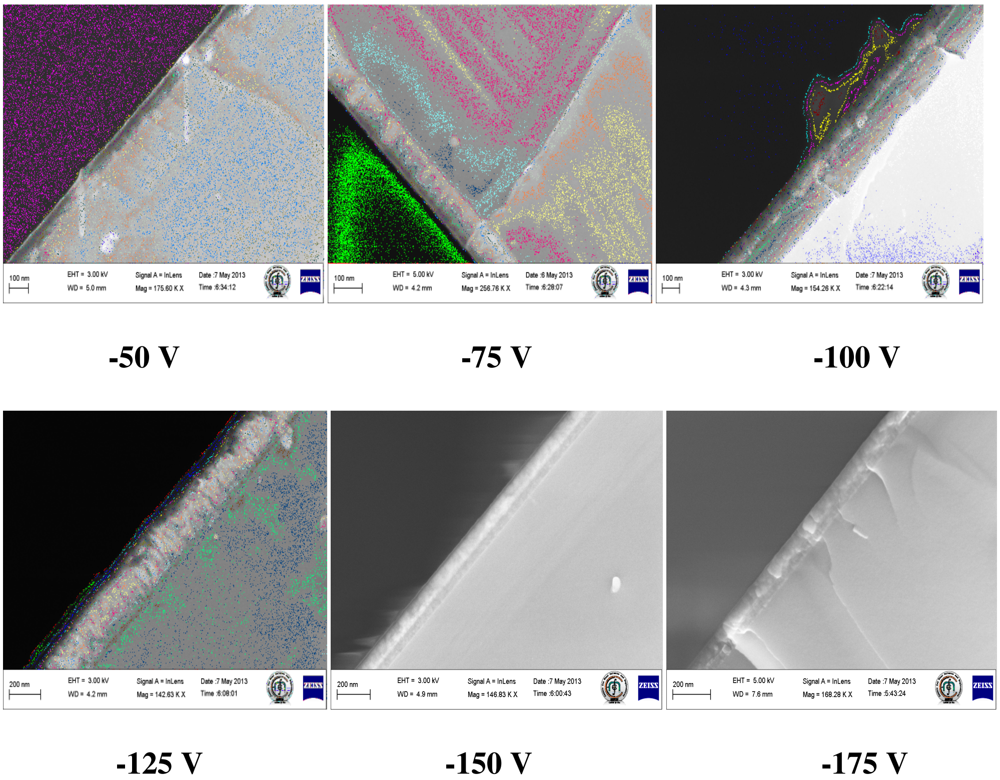

-50 V **-75 V** **-100 V**

-125 V **-150 V** **-175 V**

Figure 3.8: SEM images showing cross sectional views of the deposited films

3.4 Discussion: Effect of bias variation on properties of yttrium oxide thin films

From the X-ray diffraction patterns, it is seen that films A, B, C and D have polycrystalline BCC structure and there is a loss of crystalline nature in case of films E and F. Film A shows textured growth along both (111) and (100) directions. Films B and D show textured growth along (111) direction while film C show preferred growth along (100) direction. In case of films E and F there is a loss of crystalline nature of the films as is evident from the diffraction patterns that show two broad peaks centered at $2\theta = 29°$and 56°. The orientation of the films depends on the deposition method, temperature of the substrate, oxygen partial pressure and the total gas pressure during the deposition **[107]**. The interfacial reactions and the thickness of the interface also play a prominent role in deciding about the orientation as reported earlier by M. H. Cho and co-workers. The thickness of the interface will dictate the adatom arrangement which in turn will decide the interfacial strain energy **[61]**. Zhang et al. have observed a change in orientation of films from (111) dominated to (100) dominated with increase in oxygen pressure [**43**]. In the present case the substrate temperature, oxygen partial pressure and total gas pressure are kept same during all depositions. The initial pre-deposition treatment conditions are also same for all depositions. Therefore, the change in texture of the deposited films can be attributed to the variation in the RF self bias level on the substrate during deposition. The net input power to the plasma will vary with the bias on the substrates. This power level decides about the fragmentation of the precursor and energy of the ions that are impinging on the substrates. This is also evident from the observed deposition rate variation with the bias.

At -50 V bias (film A) on the substrate, the net power fed in the plasma is relatively less compared to the one at higher bias levels. This affects the degree of ionization in the plasma. It is therefore clear that deposition rate is lower for the film A. Yttrium oxide has a bixbyite (Mn_2O_3) structure with ordered oxygen vacancies. The unoccupied oxygen sites form parallel strings along the four (111) directions of the unit cell. These strings help in migration of oxygen through the material as deposition proceeds. Therefore, (111) plane is the lowest surface energy plane of the bixbyite structure [**59**]. There is also a good lattice constant matching between Si (100) and Y_2O_3 (111) resulting in less defects during deposition [**43**]. Also in case of film deposited at -75 V (film B), there is enhanced degree of ionization of the plasma constituents and hence due to these reasons, film B has higher deposition rate as compared to the film A. It is seen that the thickness of film C is reduced drastically. This may be due to orientation of the film along (100) direction. Since (111) is the minimum surface energy plane, growth along (100) direction may produce strain in the film hampering the deposition rate. Cho et al. [21] have suggested that the preferred orientation of thin films is dependent on overall energy minimization compromising of surface and strain energy. When surface energy is dominant, the film would grow by nucleation with lowest surface energy and by nucleation with lowest strain energy when strain energy is dominant [**61**]. Film D that is oriented along (111) also shows enhanced deposition rate compared to film C for the reasons mentioned.

Argon that is used during deposition produces heavy ions that can transfer momentum to the constituents of the plasma resulting in effective ionization of gases including precursor that is used for deposition [**109**]. However, it is observed, at high bias level, use of argon gives undesirable effects as it can bombard the growing film surface with high energy and re-sputter the film. Hence with further increase in bias level on the substrates, the re-sputtering of the deposited surface by energetic ions that are arriving at the substrate surface is dominating, resulting in lower deposition rate as observed in case of films E and F [**20,104**].

The optical constants of Y_2O_3 film are highly dependent on its microstructure [**65**] and even small changes in refractive index values may indicate significant changes in the microstructure of deposited films [**110**]. GIXRD pattern for film E shows broader peaks indicating reduction in grain size due to bombardment by energetic ions; also film E exhibits maximum refractive index. The enhanced refractive index may be due to formation of dense nanocrystals. This dense network of nanocrystals enhances the packing density reported by C. V. Ramana and co-workers **[65]**. Packing density is higher for (111) plane [**63**] as compared to other planes hence films B and D that are textured along (111) direction show high refractive index. Film A does not show any preferred orientation and hence has an intermediate value of refractive index. Orientation of film C is along (100) direction which is not densely packed compared to (111) plane and hence it shows lower refractive index compared to film B. A similar trend was also observed by Y. S. Kim and co-workers [**110**]. Film F exhibits minimum value of refractive index this may be the result of further degradation in crystallinity of the film due to heavy bombardment of highly energetic ions [**110**].

The extinction coefficient of all films is zero from deep UV to near IR region of electromagnetic spectrum indicating that all the films are transparent within this region. All films are having a good band structure so there is no light absorption **[43]**. This also indicates that there is sufficient amount of oxygen ion activity during deposition. The energetic oxygen ions in the plasma can easily react with yttrium to form yttrium oxide films with maximum transmittance [**41**]. The observed transmittance properties and high refractive index of Y_2O_3 is very useful in developing antireflection and protective optical layers [**107, 65**].

XPS being a surface sensitive technique it probes few layers on the surface of the films. GIXRD and IR results indicate deposition of single phase cubic structure; while XPS analysis indicates that the degree of stoichiometry of the deposited phase on the surface of the films varies with bias. The nonstoichiometry may be due to presence of oxygen vacancies on the surface of the films. GIXRD and IR are bulk techniques, while XPS is a surface sensitive technique. GIXRD indicates deposition of single phase BCC structure for all the deposited films. IR peaks for reduced yttria at 170, 233, 407 and 431 cm^{-1} [**48**] are not seen for all the films indicating that the nonstoichiometric nature of films as seen by XPS analysis is only a surface phenomena, the bulk being polycrystalline BCC structure. As stated earlier, semi quantitative analysis is done here by considering only Y 3*d* peak. The XPS analysis (**Table 3.3**) indicates that the degree of stoichiometry is changing with bias. The degree of stoichiometry is bias dependent and increases with bias, becomes maximum for film C and again decreases as bias is increased. At -50 V bias, the power fed in plasma is less and hence degree of ionization is less resulting in lower degree of stoichiometry, compared to films deposited at higher bias voltages. Further at this bias level, the bombarding ions have less energy and hence there can be formation of voids in the film. Formation of voids can lead to increased moisture absorption and subsequent formation of carbonate and hydroxide bonds on the film surface [**51**]. However, this being a surface phenomena, GIXRD pattern for film A indicates single phase BCC deposition. With the increase in the bias level, XPS analysis shows that degree of stoichiometry is also increasing as degree of ionization and energy of bombarding ions increase with bias. At bias voltages beyond -100 V, degree of stoichiometry of Y_2O_3 is decreasing. There is increase (4 to 5 percent) in the amount of yttrium carbonate for films E and F. This may be due to their nanocrystalline nature as nanoparticles have large surface area which favors the adsorption of atmospheric gases **[111]**. However, the increased adsorption of atmospheric gases does not affect the refractive index of nanocrystalline films as also observed by Kokuoz et al [**111**]. From FESEM results it is clear that the microstructure of the films is changing with bias. It can be seen that all films are dense and the grain size is changing with bias. For film A, grain size is approximately 25 nm. For film B, dense granular structure is visible with grain size in the range of ~ 40-50 nm. For film D the grains have grown in elongated shape with grain size of ~ 50-60 nm. Increase in nucleation density results in nanorod like structure. Thus, appearance of nanorods in case of film D indicates the onset of nanocrystalline phase formation. This corroborates with the GIXRD results which show increase in full width half maxima (FWHM) of peaks for film D compared to films deposited at lower bias voltages. Films E and F are showing a broad XRD pattern indicating nanocrystalline structure formation. However, because of the fact that Y_2O_3 is highly hygroscopic, there is an enhanced tendency to pick up moisture at the grain boundary and this result in the degradation of the surface microstructure. Although granular structure is observed, the micro structural features are not clearly seen in case of films E and F. The cross-section images taken on freshly prepared fractured surfaces of all films indicate the deposition of dense films. The Far- IR spectra shows variation in intensity of the peaks with substrate bias. It is seen that the intensity of IR peaks is directly proportional to the thickness of films. Sharp and intense triplet is obtained for films A, B, C and D. In case of films E and F the triplet at 302 cm^{-1}, 330 cm^{-1} and 375 cm^{-1} is relatively broader and shifted indicating degradation in crystalline nature [**37**] . Peak at 395 cm^{-1} is also present for all films and 468 cm^{-1} peak is present in spectra of films A, B, C, D and E. Peak at 243 cm^{-1} is observed for films A, B and C. 350 cm^{-1} and 418 cm^{-1} peaks are present for films A, B, C, E and F. Additional peaks at 183 cm^{-1}, 383 cm^{-1} and 435 cm^{-1} are observed for film E. Peak at 445 cm^{-1} is present for film F. Peaks beyond 300 cm^{-1} are due to deformation in YO_6 octahedra and motion of oxygen atoms and peaks below 300 cm^{-1} are due to motion of yttrium atoms in their octahedral **[54]**. These additional IR absorption peaks besides the triplet indicate presence of cubic yttrium oxide phase in the films **[54, 53,108]**. Thus, from IR analysis it is evident that though GIXRD pattern of films E and F are broad and diffused, these films show distinct peaks for Y-O bonding and hence are not completely amorphous.

Conclusions

From the investigations reported here it is evident that deposition of Y_2O_3 films on silicon substrates is possible at a reasonably low substrate temperature of 350 °C using RF plasma MOCVD. Different characterization techniques confirm deposition of single phase cubic Y_2O_3 on the substrates. Due to highly energetic plasma medium, as deposited coatings exhibit better optical properties without any post treatment. It is seen that all films are transparent from deep UV to near IR range, a very important property that is useful in fabrication of protective optical layers and high power laser hosts. The films deposited under varying influence of RF self bias on the substrates show changes in the texture and properties of the films indicating a strong dependence of the properties on the substrate bias during deposition. The results of these investigations indicate that it is important to control the bias level on the substrates during deposition to get desired properties of the coating.

Chapter 4

EXAFS Study on Yttrium oxide thin films

In Chapter 3 the effect of variation of self bias on the structure and properties of the deposited yttrium oxide thin films is discussed. The changes occurring due to variation of bias on the substrates could be estimated from the results of various characterization techniques. To gain further insight and understand the changes in local structure with the substrate bias, EXAFS measurements are carried out on these thin films. AFM measurements are also done to study morphology of the deposited films. Information regarding co-ordination number, bond length and disorder parameter obtained from EXAFS analysis is correlated with properties of films obtained by other characterization techniques

4.1 Introduction

EXAFS deals with the measurement of fine structures in the X-ray absorption spectra above the absorption edge of the atoms in a material. The fine oscillatory structure in the X-ray absorption spectra of a particular species of atom gives precise information regarding the radial arrangement of atoms around that element and with the advent of modern bright synchrotron radiation sources, this technique has emerged out to be most powerful for local structure determination which can be applied to any type of material viz. amorphous, polycrystalline, polymers, surfaces and solutions [**97**].

EXAFS studies on Y_2O_3 thin films have been reported earlier by different groups. Unlike XRD technique, EXAFS does not require samples with long range structural order and hence this technique is used for study of nanocrystalline samples [**112, 113**]. In case of EXAFS study on nanocrystalline Y_2O_3, presence of Y-(OH) at the particle surface was reported [**112**]. Nano-Y_2O_3 and nano-ZrO_2 ceramics were investigated by EXAFS and it was found that the cation- oxygen co-ordination is higher in sintered nano-ceramics as compared to powders of micrometer size. It was reported that after sintering, the disorder in cation-oxygen co-ordination of nano ceramics decreases compared to powders of micrometer size [**113**]. Cheng Xue-Rui et al. have observed that Y-O bond length and co-ordination number decrease below six due to the presence of oxygen vacancies in Y_2O_3 films [**114**]. They have concluded that presence of oxygen vacancy would change the electron band structure affecting the physical properties of the films. The effect of adsorption of water on Y_2O_3 was studied with EXAFS by Kuroda et al. and it was found that three types of reactions of water with Y_2O_3 are possible [**115**]. It was reported that water was physisorbed, can be strongly adsorbed and can further react to form YO-OH type of bonds. EXAFS study of Y_2O_3 thin films deposited by RF plasma enhanced MOCVD and correlation of local structure of Y_2O_3 with variation of bias voltage has not been reported earlier.

4.2 Experimental details for EXAFS measurement

EXAFS measurements on these samples at Y K edge are carried out in fluorescence mode at the Scanning EXAFS Beamline (BL-9) at the INDUS-2 Synchrotron Source (2.5 GeV, 100 mA) at the Raja Ramanna Centre for Advanced Technology (RRCAT), Indore, India. The schematic of experimental set-up for EXAFS measurement is given in **Figure 4.1**. The beamline uses a double crystal monochromator (DCM) which works in the photon energy range of 4-25 KeV with a resolution of 10^4 at 10 KeV. A 1.5 m horizontal pre-mirror with meridonial cylindrical curvature is used prior to the DCM for collimation of the beam and higher harmonic rejection. The second crystal of the DCM is a saggital cylinder with radius of curvature in the range 1.28-12.91 meter which provides horizontal focusing to the beam. For measurements in the fluorescence mode, the sample is placed at 45^o to the incident X-ray beam and the fluorescence signal (I_f) is detected using a Si drift detector placed at 90^o to the incident X-ray beam. An ionization chamber is used prior to the sample to measure the incident X ray flux (I_0) and the absorbance of the sample ($\mu = \frac{I_f}{I_0}$) is obtained as a function of energy by scanning the monochromator over the specified energy range. The absorption spectra of the samples at Y K edge are recorded in the energy range 16960- 17650 eV.

AFM measurements are carried out on Y_2O_3 thin films in semi-contact mode using NT-MDT make P47H SPM system with a diamond like carbon tip having radius of curvature 1-3 nm.

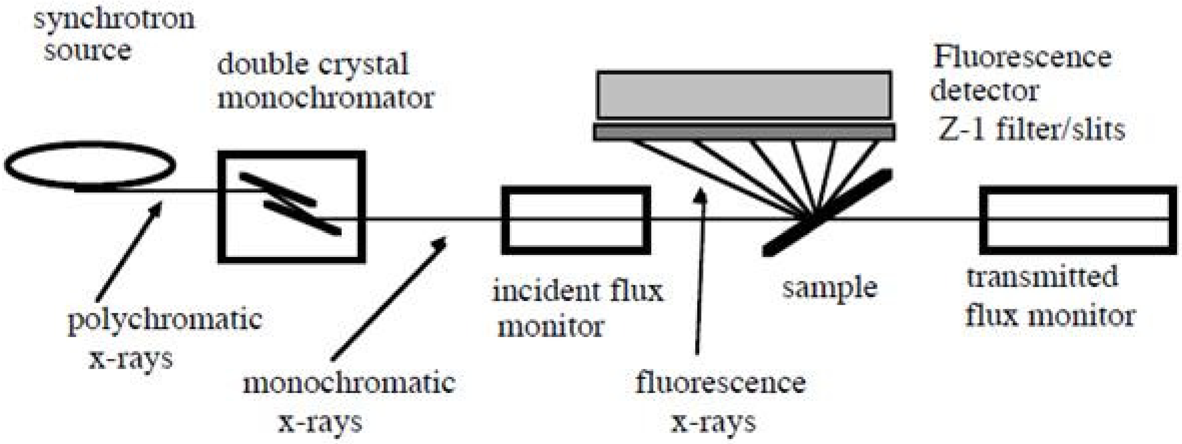

Figure 4.1: Schematic of experimental EXAFS set-up [Ref-**116**]

4. 3 Characterization results

4.3.1 *Extended X-ray Absorption fine spectroscopy*

Figure 4.2 shows the stacked raw EXAFS (normalized (μ) versus E) spectra of the various Y_2O_3 films deposited on silicon substrate under different substrate bias conditions. In order to take care of the oscillations in the absorption spectra, the energy dependent absorption coefficient $\mu(E)$ has been converted to absorption function $\chi(E)$ defined as follows:

$$\chi(E) = \frac{\mu(E) - \mu_0(E)}{\Delta\mu_0(E_0)} \qquad (4.1)$$

where E_0 absorption edge energy, $\mu_0(E_0)$ is the bare atom background and $\Delta\mu_0(E_0)$ is the step in the $\mu(E)$ value at the absorption edge. After converting the energy scale to the photoelectron wave number scale (k) as defined by,

$$k = \sqrt{\frac{2m(E - E_0)}{\hbar^2}} \qquad (4.2)$$

the energy dependent absorption coefficient $\chi(E)$ has been converted to the wave number dependent absorption coefficient $\chi(k)$, where m is the electron mass. The $k\chi(k)$ versus k spectra derived from the μ versus E spectra have been shown in **Figure 4.3** for all the samples. The analyzable k range of the data is from 3-10 Å^{-1} and the $\chi(k)$ spectra is weighted by k to amplify the oscillations at high k.

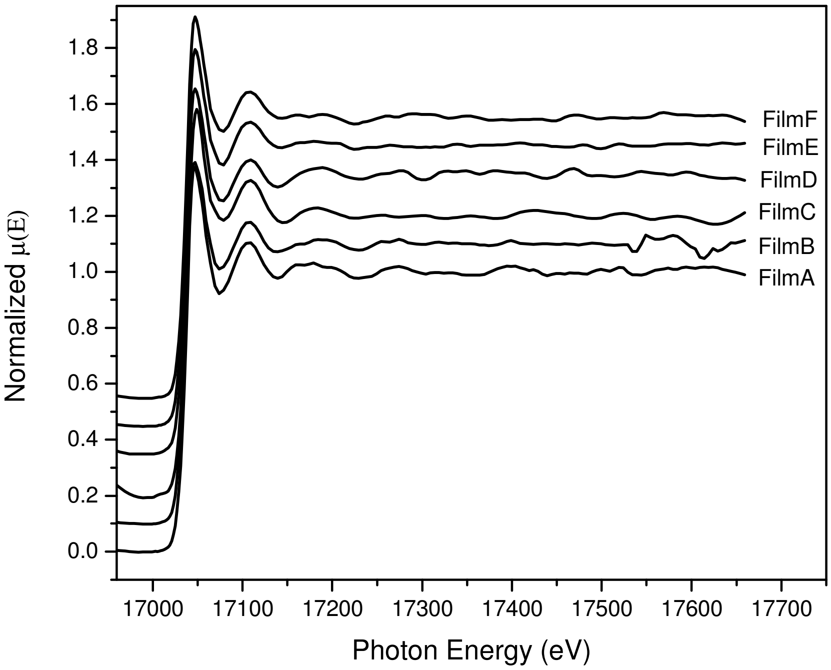

Figure 4.2: EXAFS spectra of Y_2O_3 films deposited at different bias voltage levels

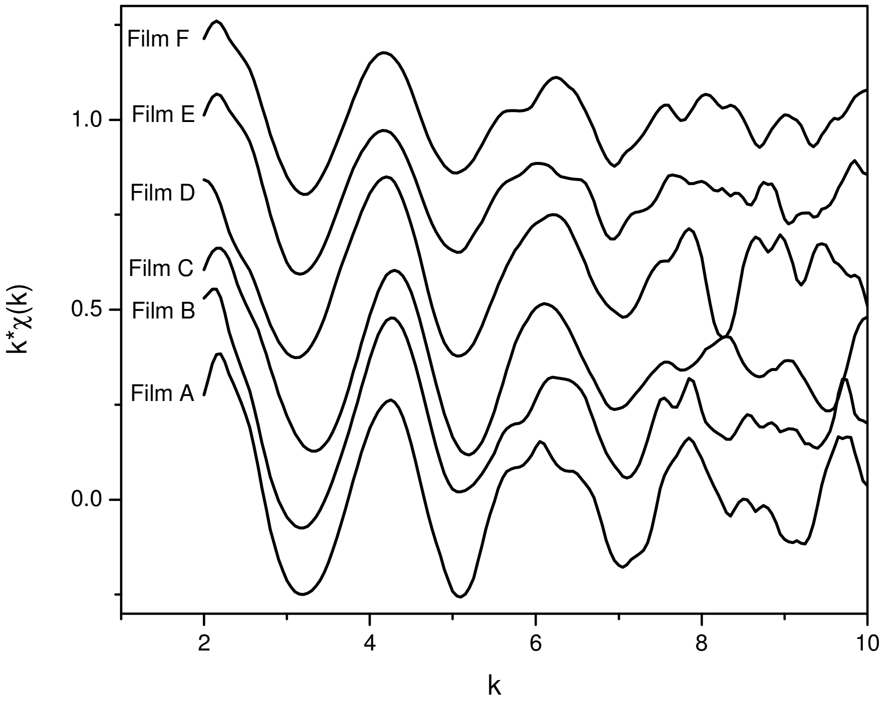

Figure 4.3: $k\,\chi(k)$ versus k spectra of Y_2O_3 films deposited at different bias voltage levels

A set of EXAFS data analysis program available within the IFEFFIT software package [**117**] have been used for reduction and fitting of the experimental EXAFS data. This includes data reduction and Fourier transform to derive the $\chi(r)$ versus r spectra from the $k\chi(k)$ versus k spectra, generation of the theoretical EXAFS spectra starting from an assumed crystallographic structure and finally fitting of the experimental data with the theoretical spectra using the FEFF 6.0 code. The goodness of the fit in each case is decided by the lowest attainable value of the parameter R which is defined as [**118**]:

$$R = \sum \frac{[\mathrm{Im}(\chi_{dat}(r_i) - \chi_{th}(r_i)]^2 + [\mathrm{Re}(\chi_{dat}(r_i) - \chi_{th}(r_i)]^2}{[\mathrm{Im}(\chi_{dat}(r_i)]^2 + [\mathrm{Re}(\chi_{dat}(r_i)]^2} \qquad (4.3)$$

Where, χ_{dat} and χ_{th} refer to the experimental and theoretical $\chi(r)$ values respectively and Im and Re refer to the imaginary and real parts of the respective quantities.

The experimental $\chi(r)$ versus r FT-EXAFS spectra of the Y_2O_3 thin film samples at Y K edge have been fitted with theoretical spectra assuming bixbyite structure with space group Ia3. The bixbyite structure is a body centered cubic structure in which the Y cation occupies two inequivalent sites i.e. the 8 C_{3i} and 24 C_2 positions. However the Y-O bond distances for the two Y sites are very close. Hence, this structure has been fitted from 1.2 to 2.4 Å assuming an average Y-O shell at 2.27Å (×6). The structural parameters for the above mentioned structure are obtained from the reported values in the literature [**52**]. **Figure 4.4** shows the experimental $\chi(r)$ versus r spectra of all the Y_2O_3 thin film samples deposited at different bias voltage along with the best fit theoretical plots carried out as above and the values of the parameter R for the best fit in each case have been given in the respective plots. Only the first co-ordination shell corresponding to Y-O bond is used for fitting. The bond distances (r), co-ordination numbers (N) (including scattering amplitudes) and disorder

(Debye-Waller) factors (σ^2), which give the mean-square fluctuations in the distances, have been used as fitting parameters. The EXAFS fitting results are tabulated in **Table 4.1**.

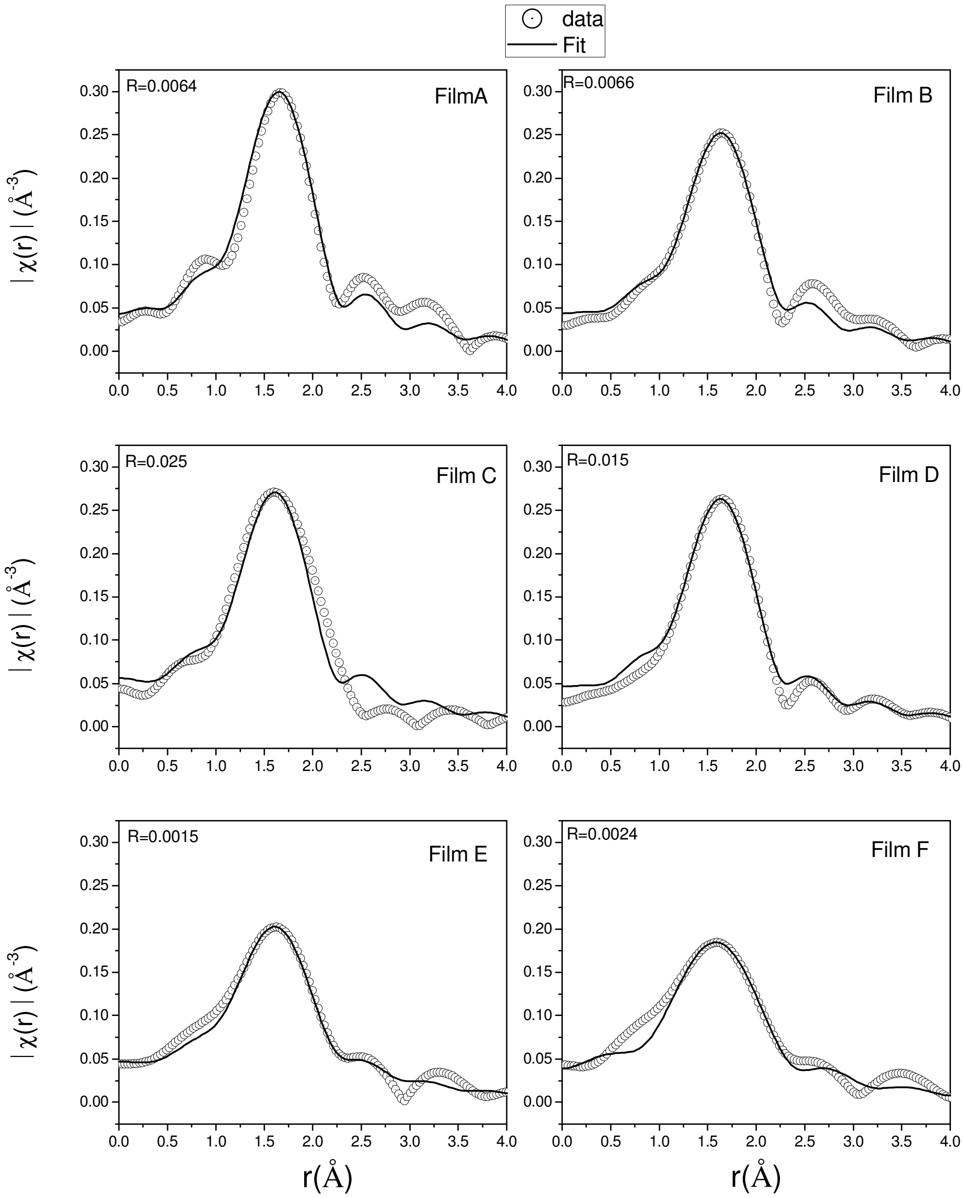

Figure 4.4: Experimental $\chi(r)$ versus r spectra along with best fit theoretical plots of Y_2O_3 films deposited at different bias voltage levels

	Film A	Film B	Film C	Film D	Film E	Film F
RF Self Bias (V)	-50	-75	-100	-125	-150	-175
Y-O Bond						
R(Å)	2.232±0.005	2.221±0.005	2.197±0.011	2.219±0.008	2.211±0.003	2.211±0.003
N	5.7±0.2	5.2±0.2	5.4±0.5	5.4±0.4	5.5±0.2	5.4±0.2
σ^2	0.0010±0.0009	0.0025±0.0009	0.0025±0.0019	0.0025±0.0013	0.0082±0.0005	0.0082±0.0008

Table 4.1: EXAFS Fitting Results

The variation of Y-O bond length, co-ordination number and disorder parameter with bias voltage is shown in **Figure 4.5** along with their respective uncertainties obtained from the fitting.

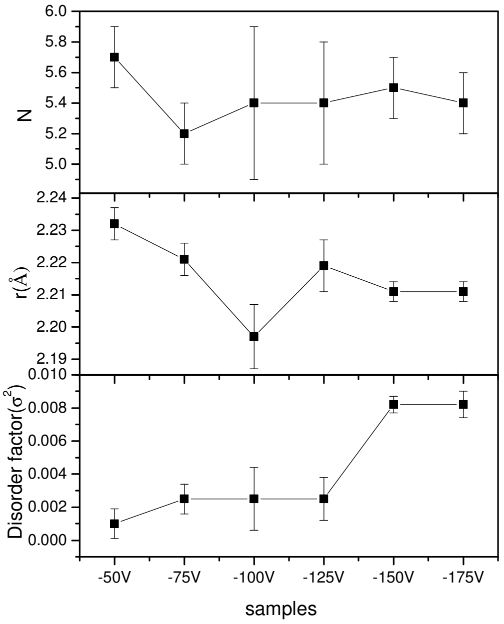

Figure 4.5: Variation of co-ordination number, bond length and Debye Waller factor with RF self-bias voltage

EXAFS analysis indicates that the local structure of the films changes with change in RF self- bias.

4.3.2 *Atomic Force Microscopy*

The 3D AFM images for the films A-F are shown in **Figure 6(a-f)** respectively and the results of AFM measurements are tabulated in **Table 4.2**.

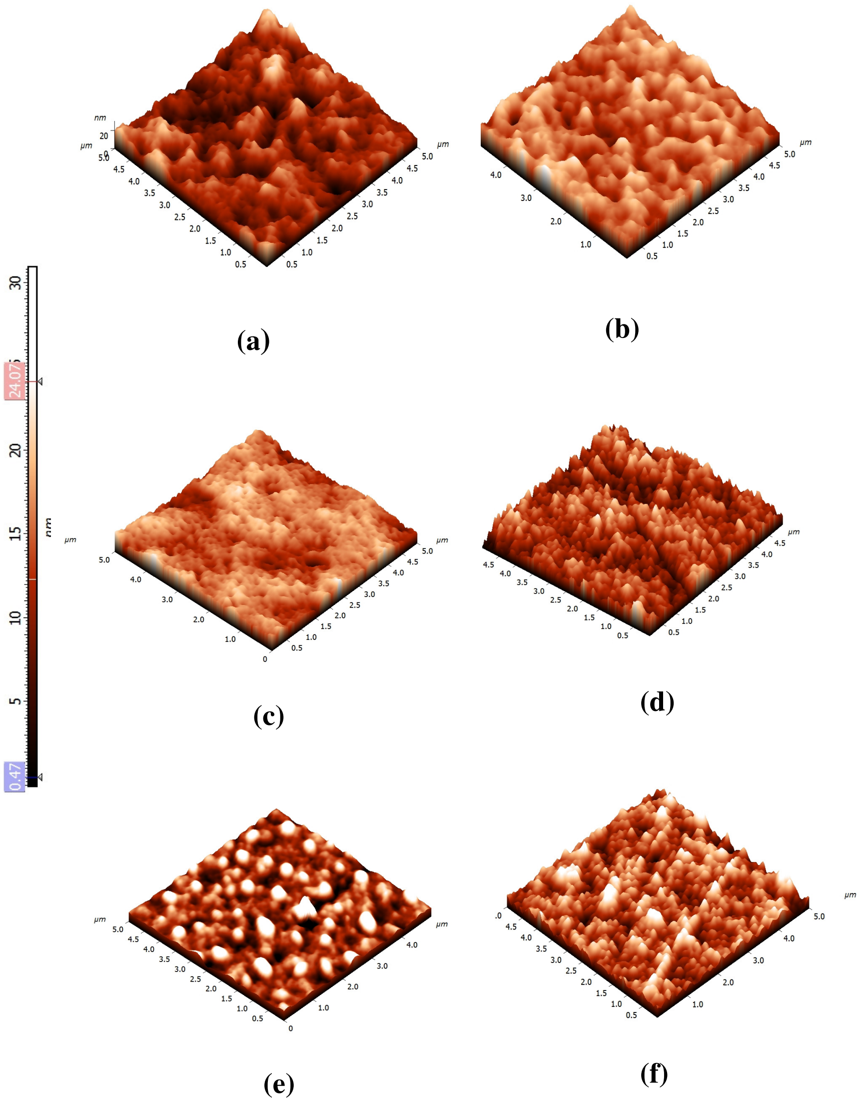

(a) **(b)**

(c) **(d)**

(e) **(f)**

Figure 4.6 (a-f): 3D AFM images of Y_2O_3 films deposited at different bias levels

Film	**Root mean square roughness (nm)**	**Entropy**
A	4.3	8.6
B	3.1	8.2
C	4.0	8.5
D	12.3	10.1
E	8.8	9.4
F	15.5	10.4

Table 4.2: AFM analysis of films deposited at various bias voltages

The expressions used for calculating root mean square roughness (R_q) and entropy $(H(Z))$ values [**119**] are given below,

$$R_q = \sqrt{(1/N_x * N_y)\sum_{j=1}^{N_y}\sum_{i=1}^{N_x}(Z_{ij}-\mu)^2}$$

$$H(Z) = -\sum_{Z} p(Z)\log_2 p(Z)$$

where, $Z_{ij} = Z(X_i, Y_j)$ is a discrete function set on XY plane, N_x and N_y are number of points on X and Y axes, μ is the average height and $p(Z)$ is the discrete probability distribution of one dimensional random variable.

The surface morphology of deposited films is also found to change with self bias. It is observed that the root mean square roughness and entropy values increase for films deposited at bias voltages higher than -100 V.

4.4 Discussion: Effect of bias variation on local structure of Y_2O_3

Our earlier analysis given in chapter-3 from the GIXRD patterns shown in **Figure 3.3** indicates that films A-D have polycrystalline BCC yttrium oxide structure while there is broadening of GIXRD peaks in case of films E and F. It is observed that film A has no preferred orientation; while films B and D show preferred growth along (111) direction and film C shows (100) as preferred growth direction. However, IR spectra reported earlier [**Figure 3.6**] indicate that all films have cubic Y_2O_3 structure.

The co-ordination number and bond length for bulk Y_2O_3 are 6 and 2.27Å respectively [**52**]. However from EXAFS analysis shown in **Figure 4.5**, it can be seen that in case of thin films, the co-ordination number and bond length are smaller as compared to the bulk. This may be due to small degree of non-stoichiometry in the deposited phase present on the surface of the films as reported earlier [**120**]. Dangling unsaturated bonds on surface of the thin films can result in decrease in bond length as well as reduction in co-ordination number.

As seen from **Figure 4.5**, the oxygen co-ordination is high for film A as compared to film B. Earlier XPS analysis (given in **Table 3.3**) indicates significantly high presence of hydroxyl and carbonate group in film A. This is supported by AFM measurements which show presence of valleys on the surface of film A.

At low bias level the decomposition of precursors is not efficient. The energy of ions impinging on the substrate is less resulting in formation of voids. These voids act as favorable sites for moisture adsorption [**51**] and hence oxygen co-ordination is high for film A [**115**]. In case of film B, with increase in bias level, the energy of ions increase, there is improvement in precursor fragmentation and ions impinge on the substrate with higher energy. Hence there is reduction in void formation resulting in decrease in adsorption of hydroxyl group which finally leads to decrease in oxygen co-ordination as compared to film A. From **Figure 4.6(b)** also it is seen that the formation of valleys on the surface in case of film B has decreased as compared to film A resulting in more smoother films with lower r.m.s. roughness as shown in **Table-4.2**. As reported earlier [**120**] the thickness of film B is also higher (250 nm) as compared to film A (140 nm) which is due to the enhanced plasma activity at RF self-bias of -75 V as compared to -50 V bias. Surface energy minimization favors growth along (111) direction and thus this indicates that in case of film B the energy of ad atoms is sufficient for the growth to take place along (111) direction. The enhancement of density of film B as compared to film A can also be seen from the ellipsometry results discussed earlier [**Figure 3.1**], which shows that the refractive index of film B is higher as compared to refractive index of film A.

However, in case of film C, though **Figure 4.6(c)** shows that roughness is less compared to film A. The refractive index is also found to be less than that of film A as orientation of film C is in (100) direction which is not densely packed as (111) plane [**63**]. From XPS analysis (**Table 3.3**), it is seen that there is increase in degree of stoichiometric yttrium oxide in case of film C, indicating increased oxygen reactivity and hence increased co-ordination . This can lead to change in oxygen vacancy concentration resulting in change of orientation to (100) [**59**] and decrease in thickness (65 nm). From **Figure 3.1**, it can be seen that film D has higher refractive index compared to film C because of its preferred orientation in (111) direction. AFM 3D image for the film D (**Figure 4.6(d)**) shows more sharp features as compared to films deposited at lower bias voltages indicating higher roughness of film D. This corroborates with GIXRD pattern of film D which shows increased

FWHM of diffraction peak as compared to films deposited at lower bias voltages indicating decrease in domain size. This decrease in coherently scattering domain size indicates the onset of dominance of sputtering effect over ad atom organization. It can be observed from **Figure 4.4**, that the theoretical fitting of the FT-EXAFS i.e., $\chi(r)$ versus r data of the films C and D are not as good as that of the films A and B, showing higher values for the R parameter and higher uncertainties in the derived values of the fitting parameters as shown in **Figure 4.5**. This is possibly due to the change in the preferred crystallographic orientation in the film C which has affected its local structure around the Y atoms. Though the effect is more pronounced in case of film C affecting both its local and long-range order, in case film D, the effect remains significant in the local structure.

In case of films E and F, which are deposited at bias level beyond -125 V, re-sputtering mechanism further dominates over surface reorganization of ad atoms. This results in higher disorder in films leading to formation of nanocrystalline structure. This can be seen from the GIXRD measurements which show broadened diffraction peaks for these samples. There is also a progressive decrease in thickness of films E (108 nm) and F (75 nm) due to dominating effect of resputtering. From **Figure 3.1** it can be seen that film E has highest refractive index due to nanocrystalline nature as reported by Ramana et al. [**65**]. As can be seen from **Table 4.2** the r.m.s. roughness value for film E is less compared to film D due to the nanocrystalline nature of film E with relatively smaller grain size. **Figure 4.6(f)** however shows sharper features on the surface of film F indicating higher roughness value which may be due to increase in level of structural distortion due to significant bombardment in case of film F. Due to this reason film F also exhibits the minimum value of refractive index. It can be seen from **Figure 4.4** and **4.5** that the fitting quality of the $\chi(r)$ versus r data is better for both the films E and F compared to the films C and D with lower values of the R parameter and lower uncertainties for the fitting parameters. This shows that the local structures around Y atom of these nanocrystalline samples are similar (viz., single oxygen shell in nearest neighborhood) to that of the polycrystalline sample deposited at lower bias voltages viz., the film B. However, nanostructures have increased surface area resulting in higher adsorption of atmospheric gases on the surface and hence there is a slight increase in oxygen co-ordination in case of films E and F compared to the film B as indicated by EXAFS analysis and shown in **Figure 4.5** [**111**].

As seen from **Figure 4.5**, the bond length in general decreases with bias. As bias increases there is reduction in void formation so the amount of adsorbed hydroxyl group decreases resulting in decrease in bond length. The Y-OH bond length is greater than Y-O bond length [**112, 113**]. However **Figure 4.5**, shows that there is abrupt decrease in bond length for film C as compared to films B and D. As has been observed from GIXRD measurements (**Figure 4.7**), the orientation of film C is along (100) direction whereas films B and D are oriented in (111) direction. So, the surface energy of film C is higher as compared to films B and D. The number of dangling bonds at the surface will increase. This leads to a compressive stress in film C, reducing the Y-O bond length as compared to films B and D [**121**] whereas it can be seen that films B and D (both oriented along (111) direction) show similar Y-O bond length. As has been discussed earlier, films E and F show broadened XRD peaks indicating formation of nanocrystalline structure. It is observed that the bond length is reduced for film E and F as compared to film D. Similar reduction of bond length with increasing structural distortion and enhancement of refractive index in case of HfO_2-SiO_2 thin films have also been earlier reported by Das et al. [**122**].

From **Figure 4.5**, it is observed that the Debye-Waller factor (σ^2) increases slightly for film B as compared to film A and remains same for films B-D. The Debye-Waller factor again increases significantly for the films E and F which implies poor crystallinity of these films which has also been observed from GIXRD measurements. Increase in disorder with decrease in particle size has been earlier reported by Zeming Qi et al. for nanocrystalline Y_2O_3: Eu powder particles [**123**]. The above mentioned results on Debye-Waller factor obtained from EXAFS measurements thus corroborate the results obtained earlier by GIXRD [**120**] that films deposited at -150 V and -175 V show nanocrystalline structure. This is due to enhanced sputtering at high bias voltages.

Conclusion

Local structure and surface morphology of Y_2O_3 thin films deposited by RF plasma-assisted MOCVD technique with different RF self-bias has been investigated by EXAFS and AFM technique. As RF self-bias increases the Y-O bond length reduces resulting in more stoichiomeric and denser coating. However, for films deposited beyond a certain bias level, the Debye-Waller factor significantly increases manifesting realization of nanostructured films with structural distortion. AFM measurements also indicate that surface morphology of the films changes with change in bias voltage, where it has been found that with initial increase in substrate bias more compact microstructure is realized with lower r.m.s. roughness. However, roughness increases significantly again as bias is increased beyond –100 V possibly due to dominating effect of re-sputtering. The changes observed in local structural parameters of the films as obtained above could well be correlated with the observed macroscopic properties of the films.

Chapter-5

Deposition and Characterization of Yttrium oxide thin films deposited using $Y(thd)_3$ and $Y(tod)_3$ precursors

In this chapter, comparative study of Y_2O_3 thin films deposited by using two different precursors, $Y(thd)_3$ and $Y(tod)_3$ is reported. The octanedionate (tod) precursors are more volatile and this results in reduced carbon incorporation in deposited film as compared to when heptanedionate (thd) precursor is used. Comparative study is performed through characterizations results on films deposited using these two precursors under identical experimental conditions.

5.1 Introduction

As stated earlier in Chapter-1, deposition of Y_2O_3 thin films by using $Y(thd)_3$ precursor have been done by various groups. However, there are very few reports on deposition of Y_2O_3 thin films by using $Y(tod)_3$ precursor [**51**]. Niu et al. have reported deposition and characterization of Y_2O_3 thin films deposited by yttrium hexafluoroacetylacetonate [$Y(HFAA)_3$] and tris(2,2,6,6-tetramethyl-3,5-heptanedionate) yttrium [$Y(tmhd)_3$] using RF plasma CVD [**37**]. They have extensively studied effects on interface formation during deposition and post deposition annealing. Pasko et al. have earlier done a comparative study of heptanedionate (thd) and octanedionate (tod) precursors for deposition of hafnium oxide and zirconium oxide thin films by pulsed liquid injection MOCVD. They have reported amorphous phase deposition at a temperature of 500-550 °C while crystalline phase was formed at 600-750 °C. They have reported that tod precursors evaporate without leaving any residue and lead to higher growth rate as compared to thd precursor. They found films deposited with tod precursors to be smooth and containing less carbon incorporation as compared to the thd precursor [**10**]. But there has been no such comparative study in case of yttrium oxide films deposited using (thd) and (tod) precursors by RF plasma enhanced MOCVD process under the influence of RF self bias on the substrates.

5.2 Experimental details for deposition of Y_2O_3 thin films by using $Y(thd)_3$ and $Y(tod)_3$ precursors

The schematic of deposition system is shown in **Figure-2.2** in chapter 2. The films were deposited by using two different precursors; $Y(thd)_3$ (film A) and $Y(tod)_3$ (film B) by RF plasma enhanced MOCVD. TGA plots for both the precursors are shown in **Figure 2.1** (**a** and **b**) in chapter 2. Silicon (100), quartz, tantalum and stainless steel substrates were used for deposition. The cleaning process of substrates has been mentioned in Chapter-2. After placing the cleaned substrates on the RF electrode, the chamber along with the precursor container and gas delivery lines are evacuated to a base pressure of 6×10^{-2} mbar pressure using a rotary vacuum pump. The delivery lines and precursor distributor ring (200 °C) are heated to avoid condensation of precursor in its path while the substrates are heated to a temperature of 350 °C with the help of programmable heater controller. Before deposition, the substrates are sputtered cleaned using plasma of argon gas (flow rate 5 sccm) at a substrate bias of -150 V for 20 minutes. The precursor container is gradually heated to a temperature of 200 °C. After sputtering, plasma of precursor vapors, oxygen (10 sccm) and argon (2 sccm) is generated and the substrate bias is adjusted to -75 V for deposition. The deposition is carried for duration of 60 minutes. During the deposition of film A and film B, only the precursors used are different, all the other experimental parameters are kept same. The operating pressure during deposition for film A was ~ 3 x 10^{-1} mbar while for film B was ~ 4 x 10^{-1} mbar.

5.3 Characterization of Y_2O_3 thin films deposited by using $Y(thd)_3$ and $Y(tod)_3$ precursors

The deposited films are characterized by GIXRD, XPS, FTIR, spectroscopic ellipsometry, SEM and thickness measurement. GIXRD was carried out using a Cu K_α radiation source using Bruker D8 Discover model. The incident (grazing) angle was fixed at 1.8°. The scans were taken in 2θ range of 10°-90° with scan step of 0.02° per 3 second. XPS was done by VG make CLAM-2 model hemispherical analyzer with Mg K_α source (1253.6 eV). FTIR measurements were recorded in Far-IR region using Bruker Vertex 80V FTIR spectrometer configured with Mylar beam splitter and DTGS detectors at 4 cm^{-1} spectral resolution. An 11° reflection accessory was used for the measurements. Ellipsometric studies were carried out with a phase modulated spectroscopic ellipsometry unit (model UVSELTM 460 ISA JOBIN-YVON, SPEX) in the range 300-1200 nm. Thickness measurement was done using Veeco make Dektak 150 stylus profilometer. SEM analysis was done by using Carl Zeiss SEM (Supra 55). Characterization results obtained are as follows,

5.3.1 *Thickness measurement*

The thickness of film A is 0.33 µm while that of film B is 1.09 µm.

5.3.2 *Grazing Incidence X-ray diffraction*

The GIXRD patterns taken on the films are shown in **Figure 5.1**. The diffraction lines corresponding to (211), (222), (400), (440) and (622) reflections as indicated in JCPDF card No. 79-1716 do match well with the observed pattern for film A. This indicates deposition of Y_2O_3 with BCC structure for film A. Broad and diffused diffraction lines corresponding to (222), (440) and (622) reflections indicating deposition of BCC structure are also seen in case of film B. Diffraction lines are sharp and intense in case of film A while in case of film B the lines are broadened indicating formation of nanocrystalline phase.

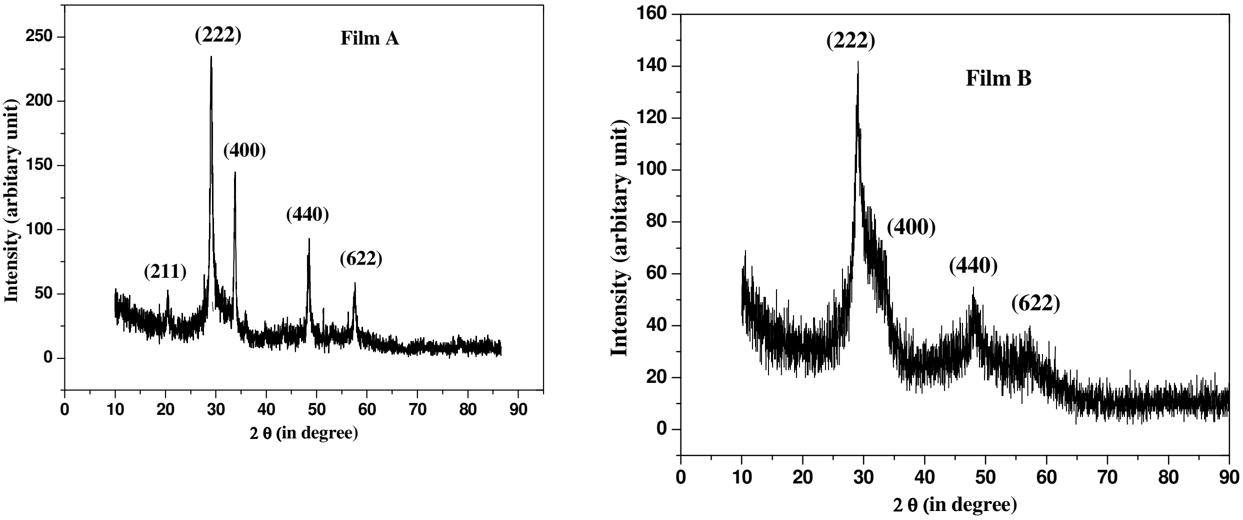

Figure 5.1: GIXRD patterns for films A and B

5.3.3 *X-ray Photoelectron Spectroscopy (XPS)*

The XPS scan was taken with pass energy of 22 eV. Peaks corresponding to Y 3*d* and O 1*s* are scanned in detail with 0.2 eV scan step. XPS Peak fit 4.1 program is used for deconvolution of the peaks. The binding energy shifts were corrected using binding energy of physiadsorbed carbon at 284.6 eV as reference **[107]**.

Y 3*d* deconvoluted peaks for films A and B are shown in **Figure 5.2**. The Y 3*d* core level is getting split into doublet (Y $3d_{5/2}$ and Y $3d_{3/2}$) due to spin orbit coupling. The doublet has energy separation of 2.1 eV and Y $3d_{5/2}$ to Y $3d_{3/2}$ areal intensity ratio is 1.5 [**107]**. The Y 3*d* peak is deconvoluted with Gaussian: Lorentzian (G: L) ratio of 40 with FWHM of individual peaks in the range of 1.4-1.7 eV and chi-square (χ^2) value in the range of 0.7-2. Two different chemical environments are found for the yttrium atoms in both the films. Peak pair with binding energy at ~156.8 eV and ~158.8 eV correspond to stoichiometric yttrium oxide, peak pairs with binding energy at ~157.8 eV and ~160 eV could be either Y-OH or Y-OC bonds [**39**].

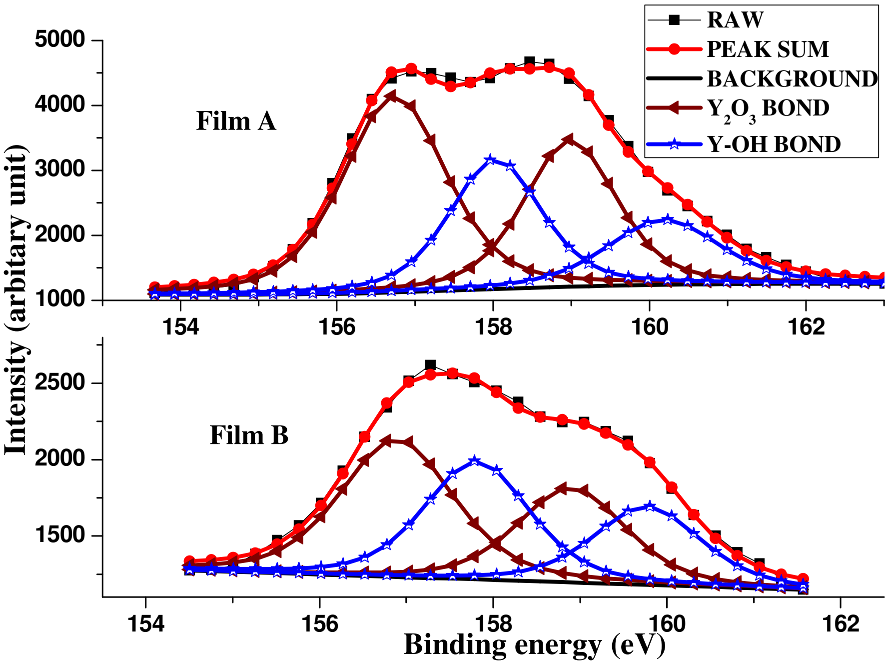

Figure 5.2: Detailed scan of Y 3*d* peak for films A and B

Deconvoluted O 1*s* peaks for both the films are shown in **Figure 5.3**. The O 1*s* peak is deconvoluted with Gaussian:Lorentzian (G:L) ratio of 40 with FWHM of individual peaks in the range of 1-1.8 eV and chi-square (χ^2) value in the range of 0.6-1.4. The O 1*s* peak for film A is deconvoluted into three sub peaks with binding energy, ~ 529.5 eV, ~ 530.5 eV and ~ 532eV corresponding to stoichiometric yttrium oxide, hydroxide (-OH) bond and C=O bond respectively while O1*s* peak for film B has three sub peaks at ~ 529.5 eV, ~ 530.5 eV and ~ 531 eV corresponding to stoichiometric yttrium oxide, -OH bond and O-C=O bond respectively [**120**].

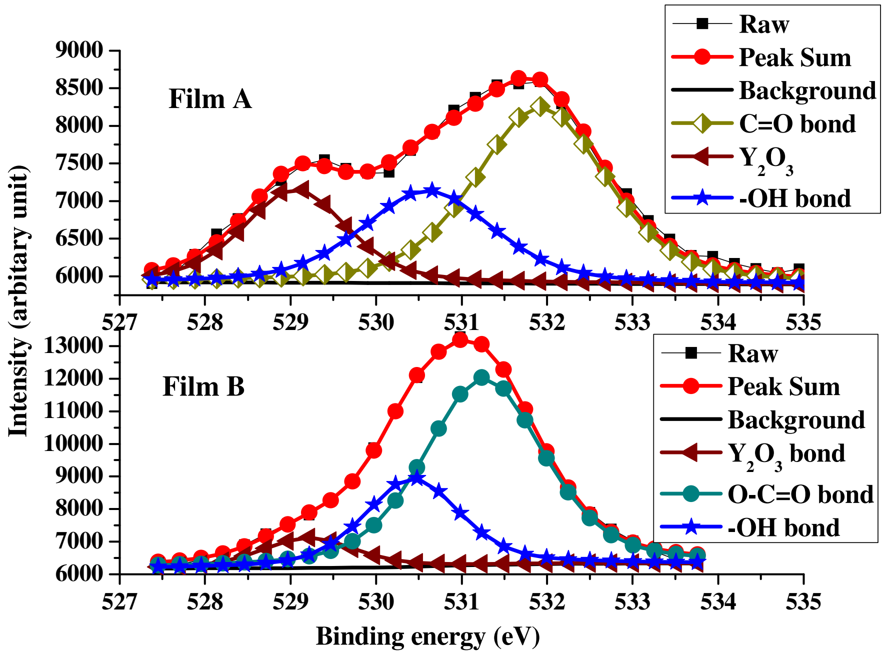

Figure 5.3: Detailed scan of O 1*s* peak for films A and B

5.3.4 *Infrared Spectroscopy*

The Far-IR reflectance spectra taken on the films are shown in the **Figure 5.4**.

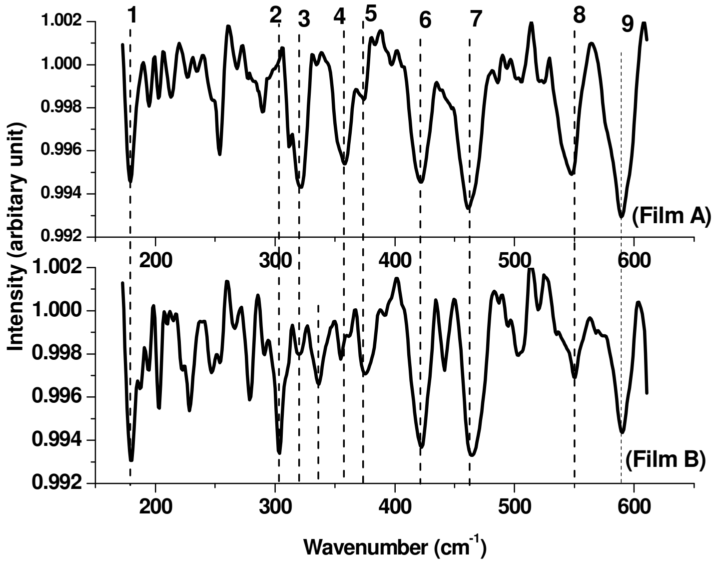

Figure 5.4: Far-IR reflectance spectrum for films A and B

The triplet at ~ 302 cm^{-1}, ~ 320 cm^{-1} and ~3 75 cm^{-1} indicating cubic Y_2O_3 structure is more clearly resolved for film B as compared to film A. Both the films show bands at ~178 cm^{-1}, ~ 358 cm^{-1}, ~ 420 cm^{-1}, ~ 462 cm^{-1}, ~ 560 cm^{-1} and ~ 582 cm^{-1} indicating cubic structure [**54, 108**].

5.3.5 *Spectroscopic Ellipsometry*

The variation of refractive index with wavelength in the range 300-1200 nm is shown in **Figure 5.5(a)**. The refractive index almost remains constant for both the films in the range of 600-1200 nm and as wavelength decreases below 600 nm, refractive index increases as reported in the literature [**43**]. Value of refractive index of film B is more than refractive index value of film A.

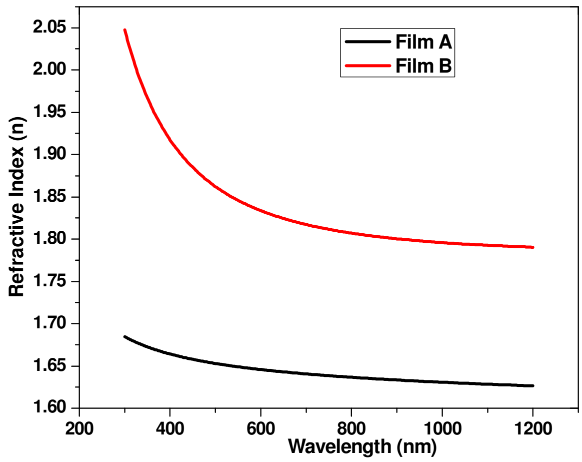

Figure 5.5(a): Variation of refractive index (n) for films A and B

The variation of extinction coefficient with wavelength in the range of 300-1200 nm is shown in the **Figure 5.5(b)**. Film B shows increased value of extinction coefficient as compared to film A. This indicates enhanced absorption in film B.

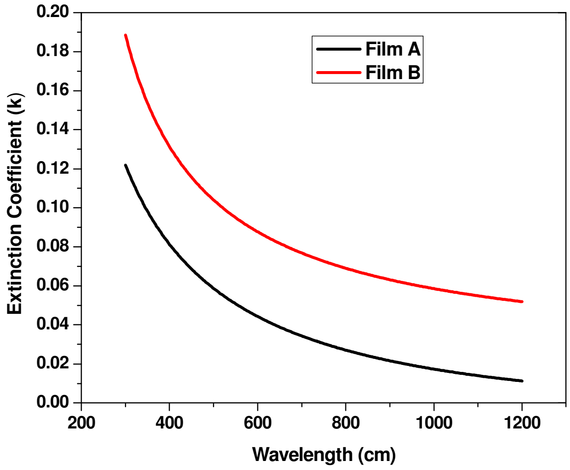

Figure 5.5(b): Variation of extinction coefficient (k) for films A and B

5.3.6 *Scanning electron microscopy*

The SEM images taken on the films A and B are shown in **Figure 5.6(a)** and **Figure 5.6(b)**. SEM images indicate formation of granular structure for both the films.

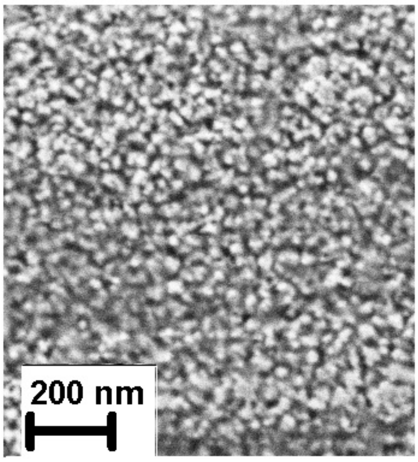

Figure 5.6(a): SEM image of film A

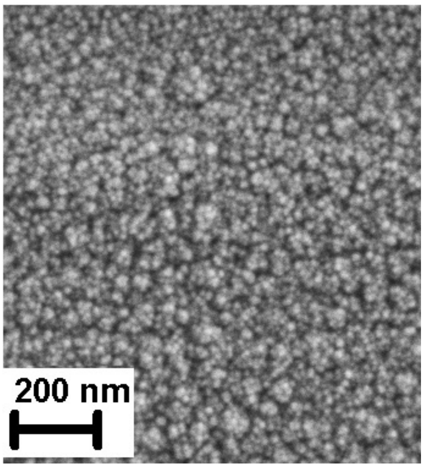

Figure 5.6(b): SEM image of film B

5.4 Discussion: Comparative study of properties of Y_2O_3 thin films deposited by using $Y(thd)_3$ and $Y(tod)_3$ precursors

It is seen that the thickness of film B is more than the thickness of film A. This is due to enhanced volatility of $Y(tod)_3$ precursor as compared to $Y(thd)_3$ precursor. This can be seen from TGA of precursors shown in **Figure 2.1** (**a** and **b**) in chapter-2**.** The enhanced volatility of tod precursors was reported earlier by Pasko and co-workers in case of $Hf(tod)_4$ and $Zr(tod)_4$ precursors stating tod precursors to be less thermally robust then the corresponding thd precursors [**10**]. In case of $Y(tod)_3$ hydrogen has been substituted by a methyl radical so enhanced shielding effect increases the volatility [**8**]. From the TGA plots it is seen that, for the $Y(thd)_3$ precursor at temperature of 200 °C, mass loss is approximately

40 % while for the $Y(tod)_3$ precursor at 200 °C, the mass loss is approximately 67 %. At 300 °C temperature, the mass loss for $Y(thd)_3$ precursor is 59 % while that for $Y(tod)_3$ precursor increases to 89 %.

From GIXRD patterns it is seen that film A has polycrystalline nature with BCC structure. Though peaks have broadened in case of film B, the GIXRD pattern seen in case of film B is also consistent with that of cubic yttrium oxide. The broad GIXRD peaks and high background of diffraction spectrum indicate that the film B has poor crystallinity as earlier reported by Kokuoz et al. [**111**]. This indicates that particle size in case of film B has decreased and there is formation of nanocrystalline structure. The broadened GIXRD peaks in case of film B may be due to increase in deposition pressure [**22**]. Both the films show textured growth along (111) direction. As yttrium oxide has bixbyite structure, (111) plane has minimum surface energy and hence preferred growth direction is along (111) [**43**]. Earlier Pasko et al. have obtained amorphous films of ZrO_2 and HfO_2 using thd and tod precursor at temperature of 550 °C by pulsed liquid injection method [**10**]. In the current work, it is seen that crystalline film deposition of Y_2O_3 is possible even at temperature of 350 °C due to high internal energy of plasma state during deposition.

Far-IR reflectance spectra confirm deposition of cubic Y_2O_3 structure in both the films. The triplet at ~ 302 cm^{-1}, ~ 320 cm^{-1} and ~ 375 cm^{-1} is more clearly resolved in case of film B than film A as thickness of film B is more than film A. The other bands ~178 cm^{-1}, ~ 358 cm^{-1}, ~ 420 cm^{-1}, ~ 462 cm^{-1}, ~ 560 cm^{-1} and ~ 582 cm^{-1} indicating cubic structure are present in both the films [**54, 108**]. SEM images for both the films indicate granular structure for both the films. This is in agreement with the GIXRD and FTIR results, confirming that film B is nanocrystalline and not amorphous in nature.

Yttrium oxide is hygroscopic in nature; hence it has a tendency to absorb moisture. The moisture further reacts with atmospheric carbon to form carbonate and hydro carbonate bonds [**46**]. The films were not sputtered prior to XPS scan hence surface adsorbed moisture and carbon species are present. Hence semi quantitative analysis is done by considering only the Y 3*d* peak [**48**]. Semi quantitative analyses from Y 3*d* peak indicate higher percentage of Y-OC bonds (44 %) on the surface of film B as compared to film A (36 %) while the amount of stoichiometric Y_2O_3 is higher in film A (64 %) as compared to film B (56 %). The O 1*s* peak deconvolution for film A shows that in addition to yttrium oxide there are hydroxide and carbonate bonds present at the surface of the film. The O 1*s* peak deconvolution for film B is dominated by the presence of carbonate bonds.

Reason for increase in carbon adsorption in case of film B is its nanocrystalline structure. Nanostructures have enhanced surface area as compared to their volume leading to greater amount of adsorption of atmospheric gases such as moisture and carbon dioxide [**111**].

Ramana et al. have reported that value of refractive index (n) and extinction coefficient (k) is also enhanced due to formation of dense network of nanocrystals [**65]**. This can be seen from the ellipsometry measurements of film B. Both refractive index (n) and extinction coefficient (k) values have increased in case of film B. The increase in (n) shows film B has higher density. Although film B shows higher amount of adsorbed moisture and carbon species on the surface its refractive index is not affected as earlier reported by Kokuoz and co-workers [**111**]. Comparative decrease in refractive index in case of film A indicates that film A is not as dense as film B. Although film A has good crystallinity, the density of film B is higher due to formation of nanocrystalline phase. Kim et al. had earlier reported that structural changes dominate the stoichiometric effects in deciding the refractive index of Y_2O_3 [**110**]. The enhancement of refractive index for nanocrystalline Y_2O_3 film as compared to well crystallized film was also observed in our earlier study reported in chapter 3.

Conclusion

Investigations reported here indicate that both the films deposited using $Y(thd)_3$ and $Y(tod)_3$ have BCC structure. Higher deposition rate can be achieved using $Y(tod)_3$ precursor. There is formation of nanocrystalline structure for the film deposited using $Y(tod)_3$ precursor. The film deposited using $Y(tod)_3$ precursor shows enhanced refractive index indicating higher density of the film.

Chapter 6

Deposition and characterization of yttria stabilized zirconia thin films using octanedionate precursors

This chapter describes about the deposition of yttria doped zirconia thin films by RF plasma enhanced MOCVD process using Y(tod)$_3$ and Zr(tod)$_4$ precursors. Keeping the content of zirconia same, the yttria content in the films is varied by changing the temperature of Y(tod)$_3$ precursor container and three different films with varying contents of yttria are deposited. The phase change and properties of the deposited films are studied with the help of different characterization techniques.

6.1 Introduction

Zirconium oxide (ZrO_2) is a wide band gap (~ 5.1eV) material with high dielectric constant (~18) and is chemically inert. Hence ZrO_2 thin films are finding applications as dielectric material in microelectronic industry [**23**]. Zirconia undergoes phase transformation with temperature. The various polymorphic forms of ZrO_2 have been discussed in Chapter 1. Various deposition methods used for deposition of yttria stabilized zirconia thin films are listed during discussion in chapter-1.

Earlier researchers have deposited yttria stabilized zirconia coatings by using microwave plasma CVD [**72, 124**]. There are very few reports on study of yttria stabilized zirconia thin films by RF plasma enhanced CVD [**125**]. In case of RF plasma enhanced CVD, DC self bias on the substrates acts as an accelerating energy source for the ions and plays an important role in deciding about the properties of the deposited films. Optical properties are found to be improved by using this technique [**120**]. Holzschuh and Suhr have reported that negative bias strongly influences the film composition and balances the oxygen deficiency in case of copper oxide thin films [**126**, **72**]. Use of metalorganic precursors for deposition is known for getting uniform, dense and conformal coating [**8**]. In the past, metal-organic precursors such as $Zr(dpm)_4$, $Y(dpm)_3$ [**72**], $Y(thd)_3$, $Zr(thd)_4$ [**74**, **125**, **76**], have been used for deposition of yttria stabilized zirconia coatings. In the present study, $Y(tod)_3$ and $Zr(tod)_4$ precursors are used for the first time for deposition of these coatings. Advantages of octanedionate (tod) precursors are enhanced volatility, evaporation without leaving any residue and reduction in carbon contamination in the deposited films.

Three different yttria stabilized zirconia thin films are deposited by varying the yttria content in the films. To study the properties of the films different characterization techniques are used. The deposited films are characterized by grazing incidence X-ray diffraction (GIXRD), fourier transform infrared spectroscopy (FTIR), X-ray photoelectron spectroscopy (XPS), field emission scanning electron microscopy (FESEM), atomic force microscopy (AFM), X-ray near edge absorption fine structure (XANES), Extended X-ray absorption fine structure (EXAFS), Energy dispersive X-ray analysis (EDAX) and spectroscopic ellipsometry. Thickness of the films is measured by stylus profilometer. Tribological investigations are carried on to study the mechanical behavior of the coatings.

6.2 Experimental details for deposition of YSZ thin films

The schematic of deposition system and detailed cleaning procedure for substrates is given in chapter-2. The cleaned substrates were placed on the RF electrode. The $Zr(tod)_4$ and $Y(tod)_3$ precursors in form of pellets are placed in two separate containers (provided with gate valve) that can be heated by heating tapes wound on it. The flow rate of each precursor can be independently controlled by using gate valve. The base pressure achieved by the rotary pump was order of 7.4×10^{-2} mbar. The substrates were heated to a temperature of 400 °C by using a programmable heater controller. Then substrates were sputter cleaned by argon plasma for 20 minutes. During sputtering, flow rate of argon was maintained at 5 sccm and the bias was kept at -150 V. The operating pressure during sputtering was ~1.8×10^{-1} mbar.

After sputtering, plasma of argon, oxygen, vapors of $Zr(tod)_4$ and $Y(tod)_3$ was used for the deposition. The temperature of container with $Zr(tod)_4$ precursor is maintained at 220 °C while three different films namely A, B and C were deposited by maintaining temperature of $Y(tod)_3$ containing container at 110 °C, 130 °C and 160 °C respectively. Argon and oxygen flow rates were maintained at 1 and 10 sccm respectively for all the films. The operating pressures were in the range of 3.5×10^{-1} to 2.8×10^{-1} mbar. The RF self bias on the substrates was maintained at -100 V and deposition was carried out for a period of 60 minutes for all the three films.

6.3 Characterization of YSZ thin films deposited by using $Y(tod)_3$ and $Zr(tod)_4$

Thickness of the films was measured using DekTek stylus profilometer (model 150 Veeco).The deposited films were further characterized by EDAX, GIXRD, FTIR, spectroscopic ellipsometry, XPS, FESEM, AFM, XANES and EAXFS. To estimate mechanical properties, tribological measurements were carried on the deposited YSZ films. EDAX was done using Bruker Quantax make X-ray detector. GIXRD was carried out with a Cu K_α radiation source using Bruker D8 Discover model. The incident (grazing) angle is fixed at 1.8°. The scans were recorded in 2θ range of 10°-70° with scan step of 0.02° per 3 second. XPS was done with SPECS Gmbh spectrometer with Phoibos 100 MCD energy analyzer. Scans were taken using Al K_α (1486.6 eV energy) with a pass energy of 22 eV. Infrared spectra were recorded in the Far-IR region at 4 cm^{-1} spectral resolution using Bruker Vertex 80 V FTIR spectrometer configured with Mylar beam splitter and DTGS detector. An 11° reflection accessory was used for the measurements. Ellipsometric studies were carried out with a phase modulated spectroscopic unit (model UVSELTM 460 ISA JOBIN-YVON, SPEX) in the range 300-1200 nm. AFM was done in semi-contact mode using NT-MDT make P47H SPM system with a diamond like carbon tip having radius of curvature 1-3 nm. EXAFS measurements on these films at Y and Zr (K) edges were carried out in fluorescence mode at the scanning EXAFS Beamline (BL-9) at the INDUS-2 Synchrotron Source (2.5 GeV, 100 mA) at the Raja Ramanna Centre for Advanced Technology (RRCAT), Indore, India [**127**,**128**]. Details regarding the experimental setup for EXAFS measurements are illustrated in chapter-4. The EXAFS spectra of the samples at Y and Zr (K) edge were recorded in the energy range 16900-17400 eV and 17950-18430 eV respectively.

Linear reciprocating mode of a ball on the disk micro- tribometer (CSM Instruments, Switzerland) was used to carry out friction measurements. In all these measurements, the normal loads, sliding speeds and sliding distance were kept constant at 1 N, 4 cm/s and 100 m, respectively. The diameter of the sliding Al_2O_3 ball is 6 mm with a surface roughness of 0.04 µm. Tribology experiments were conducted in ambient atmospheric and non-lubricated conditions at room temperature where relative humidity level is 75 %. The deformation and morphology of the wear tracks were examined by the FESEM. Scratch resistance of the film was measured by a scratch tester (CSM Instruments, Switzerland) coupled to a Rockwell spherical diamond indenter with a tip radius of 200 µm. These tests were performed using progressive loads from 1 to 30 N for a transverse scratch length of 3 mm with loading rate of

5 N/min. The tests were carried out in ambient atmospheric conditions. Scratch tracks were examined by FESEM (make-Zeiss, model-Supra.)

6.4 Characterization results

Table 6.1 shows the percentage of yttria (estimated from the EDAX measurement) and thickness of the films.

Film	**Temperature of $Y(tod)_3$ containing bubbler (°C)**	**Yttrium atomic % (EDAX)**	**Mol % yttrium oxide**	**Thickness (nm)**
A	110	14	4	336
B	130	17	5	376
C	160	30	9	495

Table 6.1: Variation of yttria content and thickness of YSZ thin films with temperature of $Y(tod)_3$ container

It is seen that percentage of yttria content in the films is increasing with increase in temperature of $Y(tod)_3$ precursor container. Similar trend is observed for thickness values of the films.

6.4.1 *Grazing incidence X- ray diffraction*

The GIXRD patterns for the films are shown in **Figure 6.1**. The diffraction peaks for all the films are broadened indicating small crystallite size. The diffraction lines for cubic and tetragonal phase of YSZ are close and as peaks are broadened, identification of different phases from GIXRD pattern may not be very accurate. There could also be co-existence of other phases in the film. The diffraction pattern for film A shows broader peaks as compared to film B and in case of film C diffraction pattern shows two broad peaks without any sharp features indicating the formation of nanocrystalline phase.

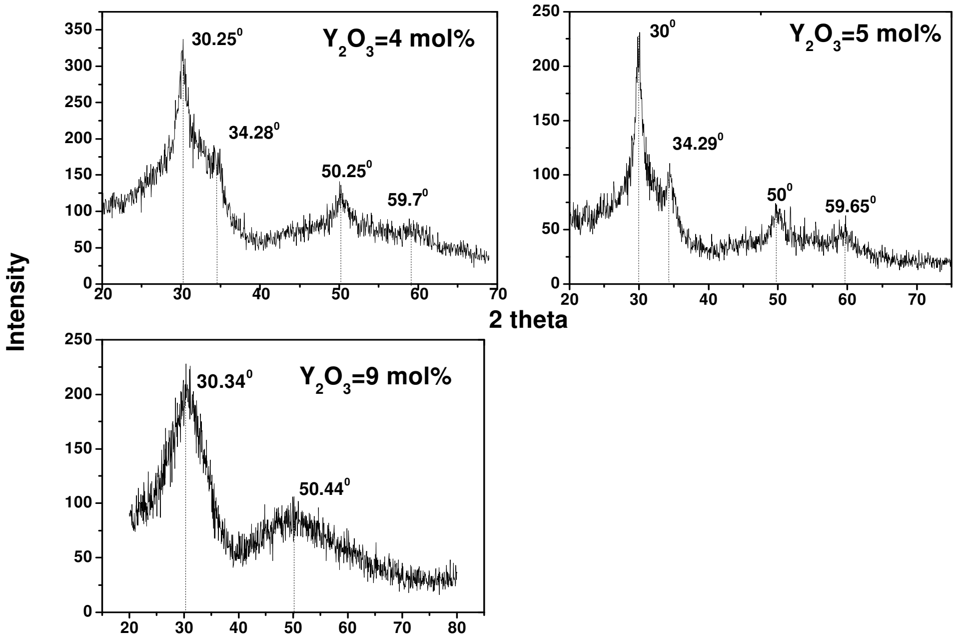

Figure 6.1: GIXRD patterns for films deposited with different yttria content

6.4.2 *Fourier Transform Infrared Spectroscopy*

The Far-IR spectra taken on the films are shown in **Figure 6.2**. The spectra for film A shows peaks at 228, 334, 380, 419, 504, 594 cm^{-1} indicating presence of monoclinic phase while peak at 632 cm^{-1} indicate the presence of tetragonal phase .The peaks at 253, 230 and 281 cm^{-1} indicate the presence of monoclinic phase while peaks at 458, 643 $cm^{-1}$and the broad band ~ 550-650 cm^{-1} indicate presence of tetragonal phase for the film B. The dominant peak at 636 cm^{-1} indicate cubic phase [**82**, **80**, 1**29**].

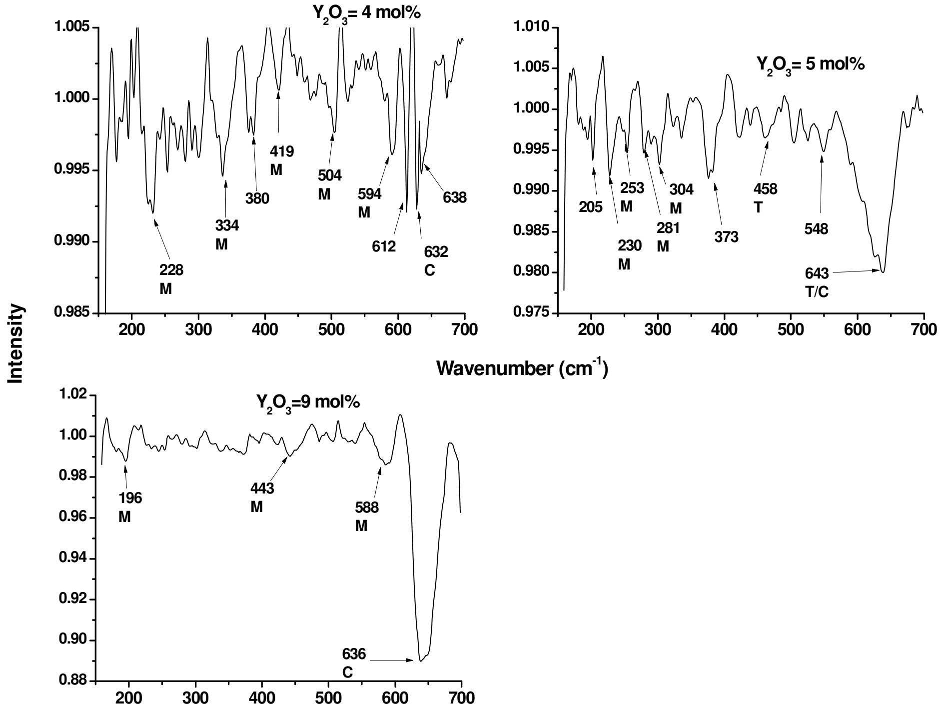

Figure 6.2: Far-IR reflectance spectra for films deposited with different yttria content

The vibrational modes below 450 cm^{-1} in monoclinic ZrO_2 are external modes which describe ZrO_2 molecules vibrating as rigid units while those above 450 cm^{-1} are internal modes in which Zr or O atoms vibrate relative to one another. Zhang et al. have proposed that with decrease in particle size, the internal modes soften to some extent while external modes are least affected [1**29**].

6.4.3 Spectroscopic Ellipsometry:

Figure 6.3 (a) shows the variation of refractive index with wavelength for the films A, B and C.

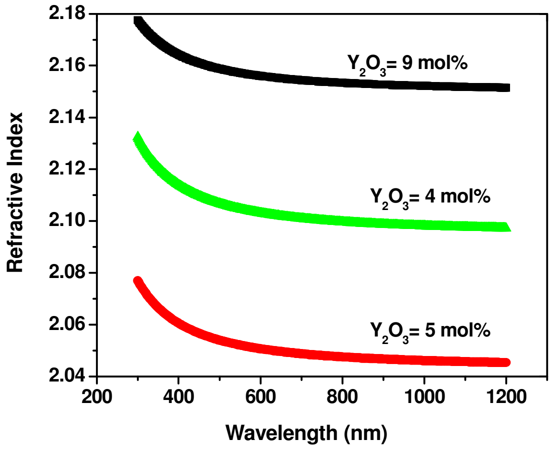

Figure 6.3 (a): Variation of refractive index with wavelength for films deposited with different yttria content

The refractive index remains constant in the wavelength range 600-1200 nm and increases as wavelength decreases below 600 nm, in agreement with the literature [**130**]. The refractive index is highest for the film C and minimum for the film B. The extinction coefficient for all the three films is zero within the measurement limit as shown in **Figure 6.3 (b)**.

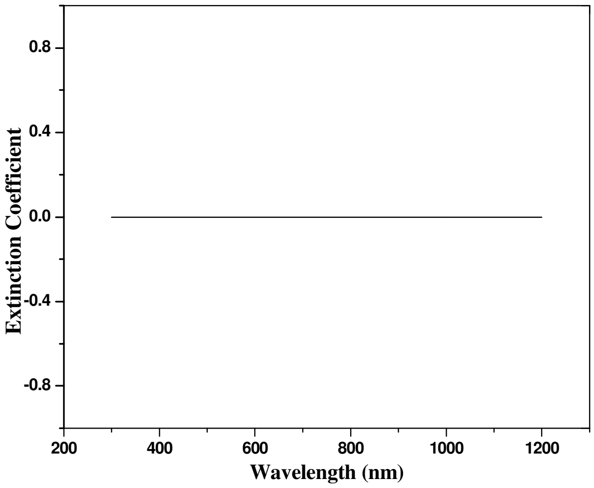

Figure 6.3 (b): Variation of extinction coefficient with wavelength for films deposited with different yttria content

6.4.4 *X-ray photoelectron spectroscopy*

The XPS scans were taken with pass energy of 22 eV. Peaks corresponding to Zr 3*d*, Y 3*d* and O 1*s* were scanned in detail with 0.1 eV scan step. These peaks are deconvoluted by using XPS Peak fit 4.1 program. The binding energy shifts are corrected using binding energy of physiadsorbed carbon at 284.6 eV as reference. Prior sputtering of the film surfaces was not done to avoid any structural changes **[83]**. Hence carbon and moisture contamination is seen on the surface of the films. The Zr 3*d* deconvoluted peaks for films deposited with different yttria concentration are shown in **Figure 6.4(a)**.

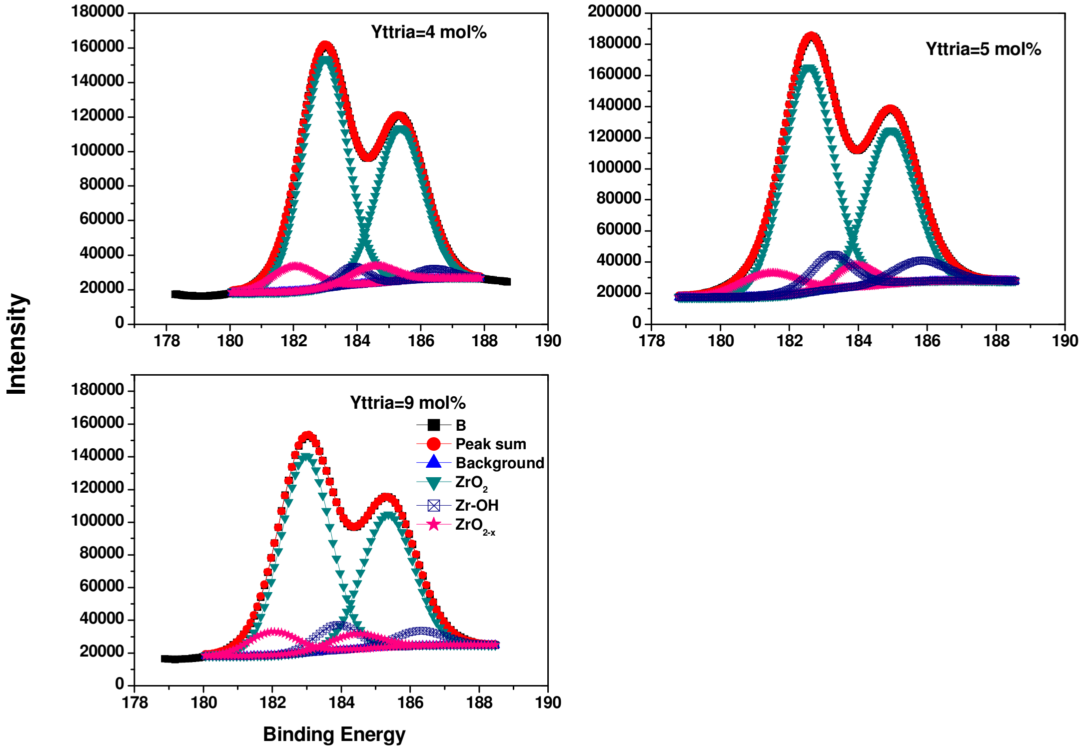

Figure 6.4(a): Zr 3*d* detailed XPS scans for films deposited with different yttria content

The Zr 3*d* core level is getting split into doublet (Zr 3*d* $_{5/2}$ and Zr 3*d* $_{3/2)}$ due to spin orbit coupling. The doublet has energy separation of 2.4 eV and Zr 3*d* $_{5/2}$ to Zr 3*d* $_{3/2}$ intensity ratio is 1.5 [**83**]. Three different chemical environments are found for the zirconium atoms in all films. Peak pair at binding energy, ~ 182.4 and 184.8 eV corresponds to Zr^{4+} oxidation state. While peak pair at lower binding energy ~ 181.5 and 183.9 eV correspond to the reduced Zr^{2+} [**131**]. Zr-OH shift binding energy to higher value ~ 183.4 and 185.8 eV [**132**].

The Y 3*d* deconvoluted peaks for deposited films are shown in **Figure 6.4(b)**.

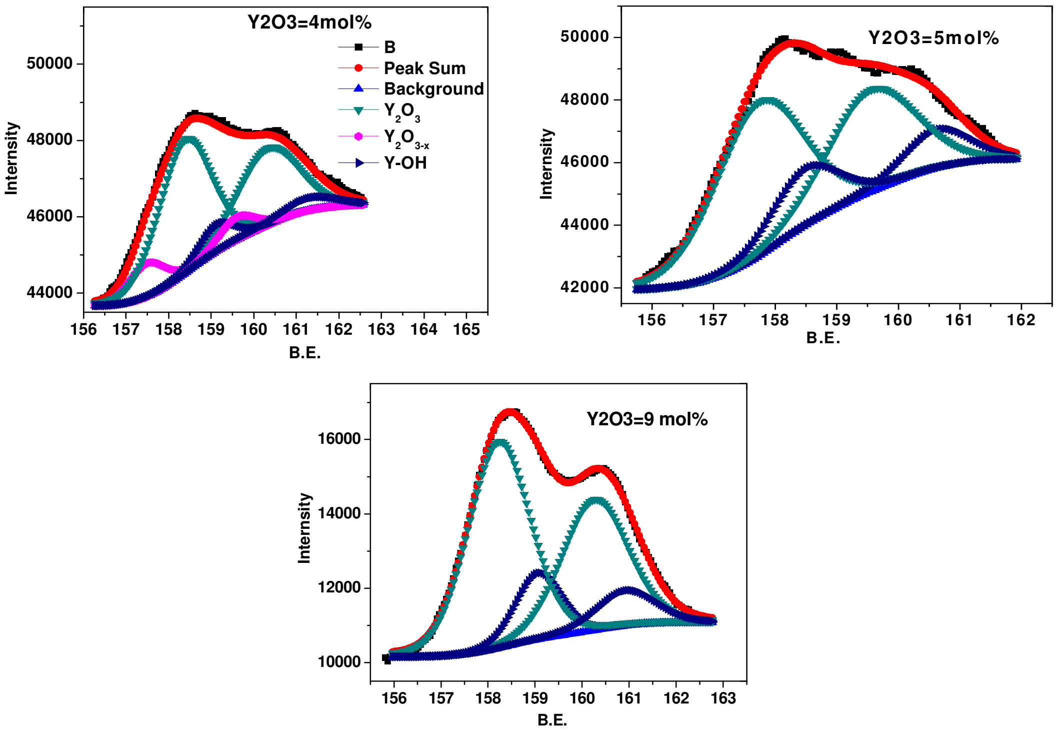

Figure 6.4(b): Y 3*d* detailed XPS scans for films deposited with different yttria content

The Y 3*d* core level gets split into doublet (Y 3*d* $_{5/2}$ and Y 3*d* $_{3/2}$) due to spin orbit coupling. The doublet has energy separation of 2.1 eV and Y 3*d* $_{5/2}$ to Y 3*d* $_{3/2}$ intensity ratio is 1.5. The peak corresponding to Y 3*d* core level is deconvoluted into three peak pairs corresponding to three different chemical environments. Peak pair at binding energy ~ 156.2 eV and 158.3 eV correspond to stoichiometric Y_2O_3. Peak pair at ~ 157.4 and 159.4 eV correspond to Y-OH [**83**]. Peak pair at ~ 155.2 and 157.2 eV corresponds to reduced Y_2O_3 [**120**]. Semi quantitative analyses from Zr 3d peak for the three films have been shown in **Table 6.2**.

Film	**ZrO_2 %**	**ZrO_{2-x} %**	**Zr-OH %**
A	82.2	9	8.9
B	78.9	9.4	11.7
C	86.9	8.9	4.2

Table 6.2: Semi quantitative analysis (by XPS) of film surfaces from Zr 3*d* peak

6.4.5 *Field emission scanning electron microscopy*

The FESEM images on as deposited surfaces of the films are shown in **Figure 6.5**. The images indicate that deposited films are uniform and dense.

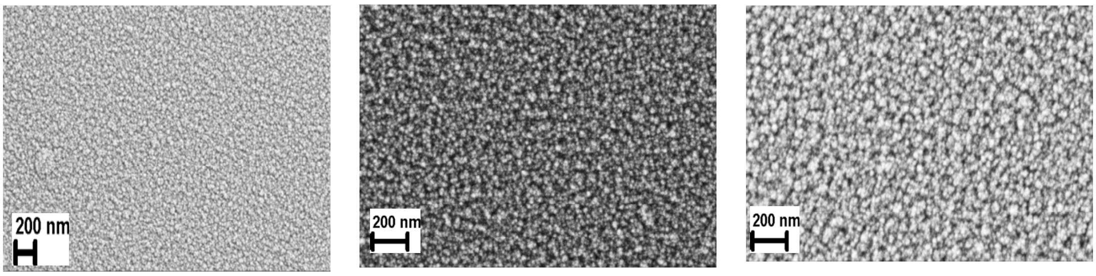

Y_2O_3= 4 mol% **Y_2O_3= 5 mol%** **Y_2O_3= 9 mol%**

Figure 6.5: FESEM images for films deposited with different yttria content

6.4.6 *Atomic Force microscopy*

The 3D AFM images of the deposited films are shown in **Figure 6.6**. The root mean square roughness value for the three films, A, B and C are 1.5 nm, 4.2 nm and 3.7 nm respectively.

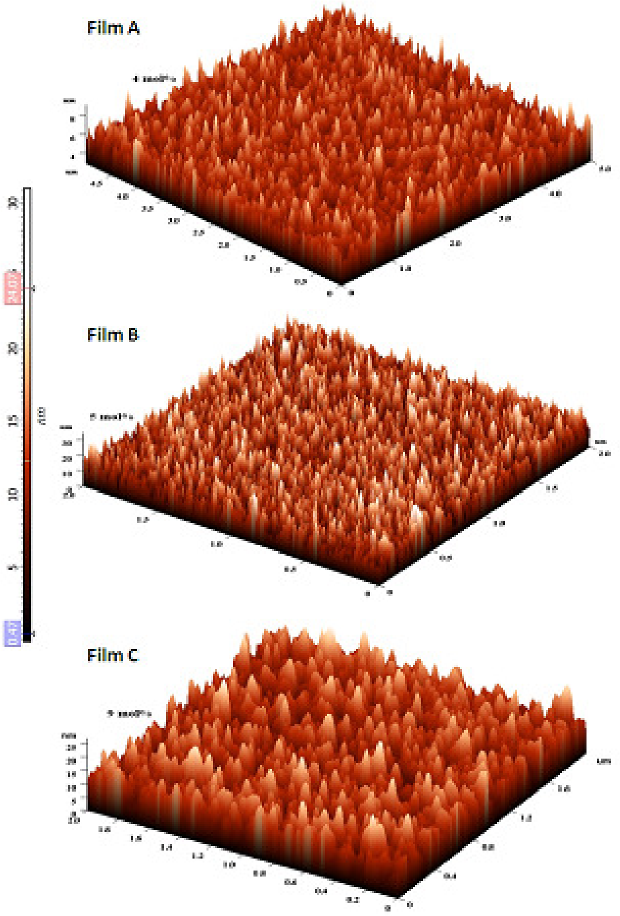

Figure 6.6: AFM 3D images for films deposited with different yttria content

6.4.7 *X-ray Absorption Near Edge Structure and Extended X-ray Absorption Fine Structure*

Figure 6.7 shows the Zr K edge XANES spectra of the films from where it is seen that with change in yttria concentration the near edge spectra shows some new features denoted by arrows in the figure which confirms structural change of zirconia with doping. As the concentration of yttria increases, the absorption edge becomes broader and then splits into two.

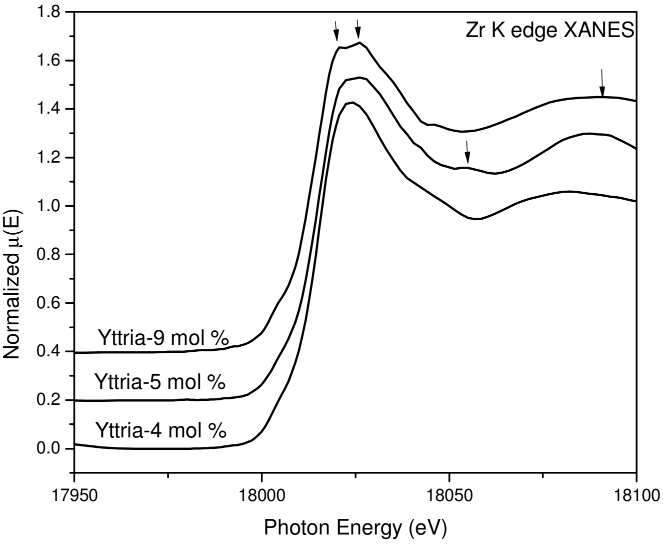

Figure 6.7: Zr K edge XANES spectra of films deposited with different yttria content

Figure 6.8 shows the experimental EXAFS ($\mu(E)$ versus E) spectra of the YSZ thin films deposited with different yttria concentration at Zr K edge. $\chi(k)$ is weighted by k^2 to amplify the oscillation at high k. **Figure 6.9** shows the $\chi(k)\,k^2$ versus k spectra of the YSZ thin films. The functions $\chi(k)\,k^2$ are Fourier transformed in r space to generate the $\chi(r)$ versus r (or FT-EXAFS) spectra in terms of the real distances from the center of the absorbing atom. A set of EXAFS data analysis program available within the IFEFFIT software package [**117**] have been used for reduction and fitting of the experimental EXAFS data. **Figure 6.10** shows the experimental $\chi(r)$ versus r spectra of the thin films along with the best fit theoretical plots. The values of the best fitting parameters for the Zr K edge EXAFS spectra have been shown in **Table 6.3**.

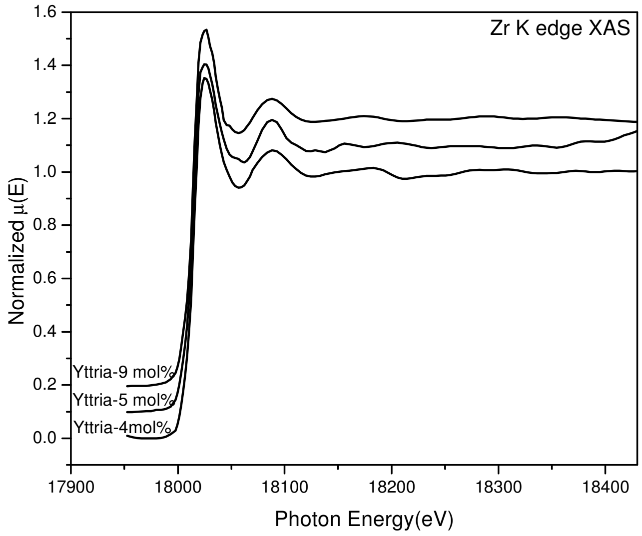

Figure 6.8: Experimental EXAFS ($\mu(E)$ versus E) spectra of the films deposited with different yttria concentration at Zr K edge

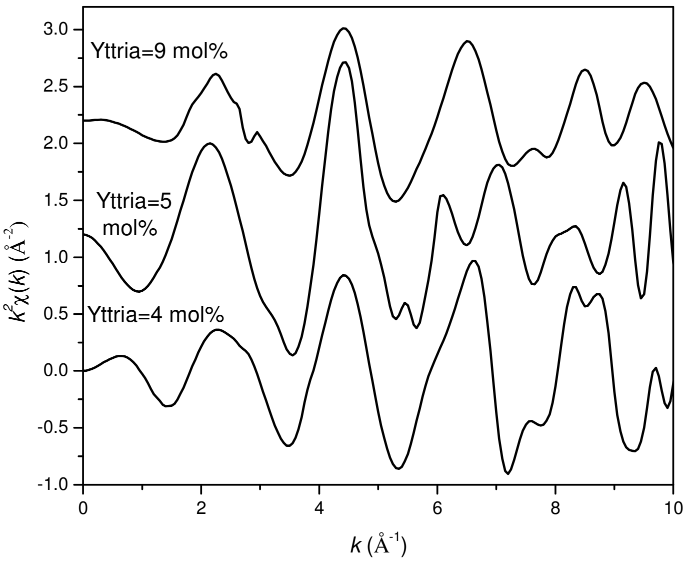

Figure 6.9: $\chi(k)\,k^2$ versus k spectra for the Zr K edge

	Yttria=4 mol % (Monoclinic Structure) R factor=0.001			
Bond	Theoretical r (Å)	r (Å)	N	σ^2
Zr-O	1.91	2.09(4)	2	0.003(2)
Zr-O	2.12	2.13(3)	2	0.002(2)
Zr-O	2.33	2.24(2)	2	0.004(3)
Zr-O	2.50	2.58(5)	1	0.002(1)
	Yttria=5 mol % (Tetragonal Structure) R factor=0.005			
Zr-O	2.08	2.05(5)	4	0.006(4)
Zr-O	2.38	2.23(5)	4	0.006(3)
	Yttria=9 mol % (Cubic Structure) R factor = 0.007			
Zr-O	2.22	2.14(4)	8	0.016(3)

Table 6.3: EXAFS fitting results for the Zr K edge

Yttria=5 mol % (Tetragonal Structure) R factor=0.016			
Y-O	2.14(3)	3.0(4)	0.008(4)
Y-O	2.32(2)	3.2(4)	0.002(2)
Yttria=9 mol % (Cubic Structure) R factor = 0.001			
Y-O	2.31(1)	6.5(6)	0.009(2)

Table 6.4: EXAFS fitting results for the Y K edge

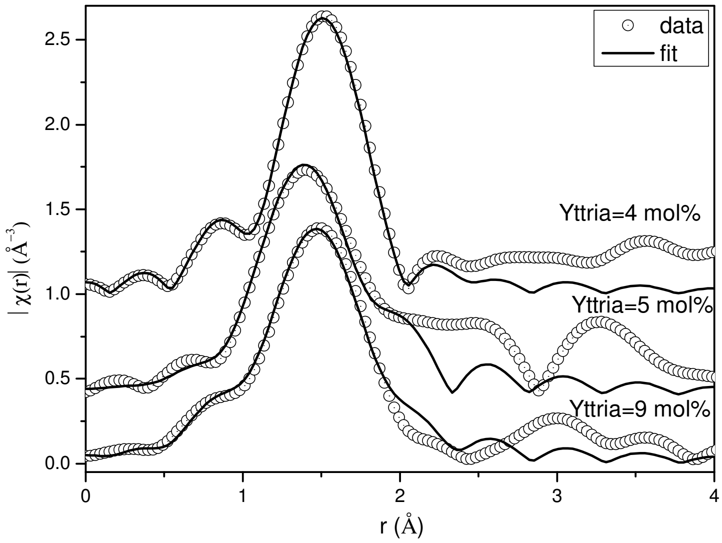

Figure 6.10: Experimental $\chi(r)$ versus r spectra along with best fit theoretical plots for the Zr K edge

Figure 6.11 shows the experimental EXAFS ($\mu(E)$ versus E) spectra of the films B and C at Y K edge. The quality of EXAFS data at Y K edge of film A was not good due to low concentration of yttria in it and hence has not been analyzed. The $\chi(k)$ spectra are weighted by k as shown in **Figure 6.12**. The experimental $\chi(r)$ versus r spectra of the films B and C have been fitted in the range of 1-2.2 Å assuming Y^{+3} ions replace Zr^{+4} ions. The experimental $\chi(r)$ versus r spectra of the films B and C at Y K edge along with the best fit theoretical plots have been shown in **Figure 6.13**. The results of the best fitting parameters of these films have been given in **Table 6.4**. The value of S_0^2 has been fixed to 0.9 from the fitting of standard Y_2O_3 sample.

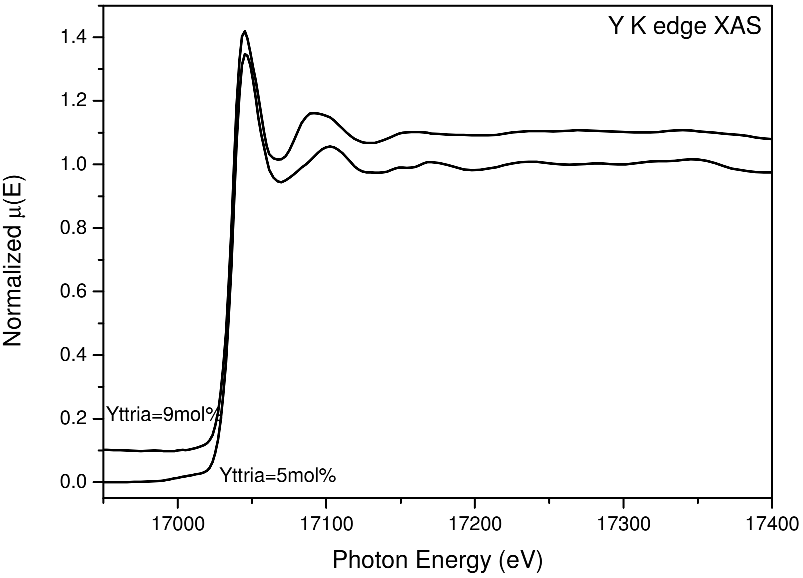

Figure 6.11: Experimental EXAFS ($\mu(E)$ versus E) spectra of the films deposited with different yttria concentration at Y K edge

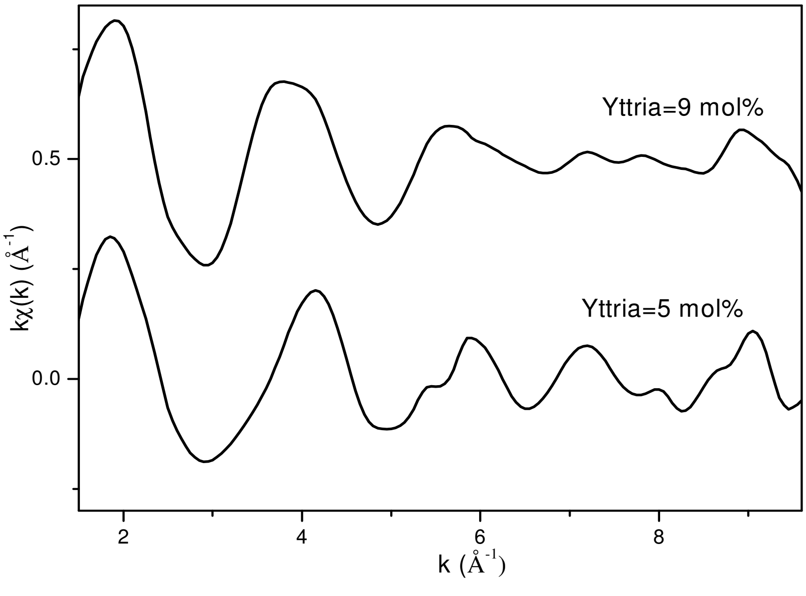

Figure 6.12: $\chi(k)\,k$ versus k spectra for the Y K edge

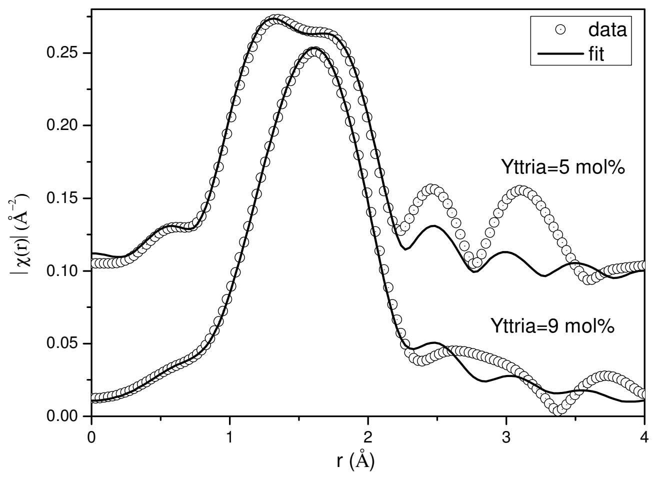

Figure 6.13: Experimental $\chi(r)$ versus r spectra along with best fit theoretical plots for the Y K edge

6.4.8 *Scratch adhesion testing*

The plot of acoustic emission against the progressive normal load during the scratch test is shown in **Figure 6.14**. The nature of acoustic emission in all the three films is similar. SEM images of scratch tracks for films A-C along with high resolution images of central portion of scratch track are presented in **Figure 6.15 (a-c)** respectively. Scratch track of film A does not show sign of cracking and the film exhibits elastic recovery. In case of films B and C parallel cracks have developed along the transverse direction of scratch length. It is observed that for film B, yielding has occurred after 2/3 portion of the track at ~ 22 N normal load. While film C has remained intact only for half the length of the track and comparatively yielded at a lower load of ~16 N.

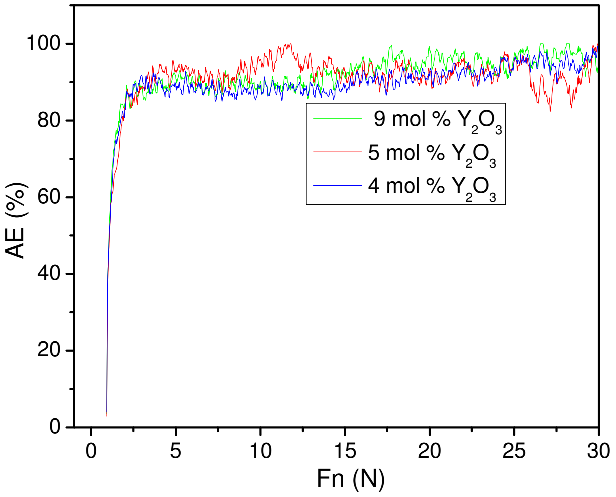

Figure 6.14: Accoustic emission vs normal force

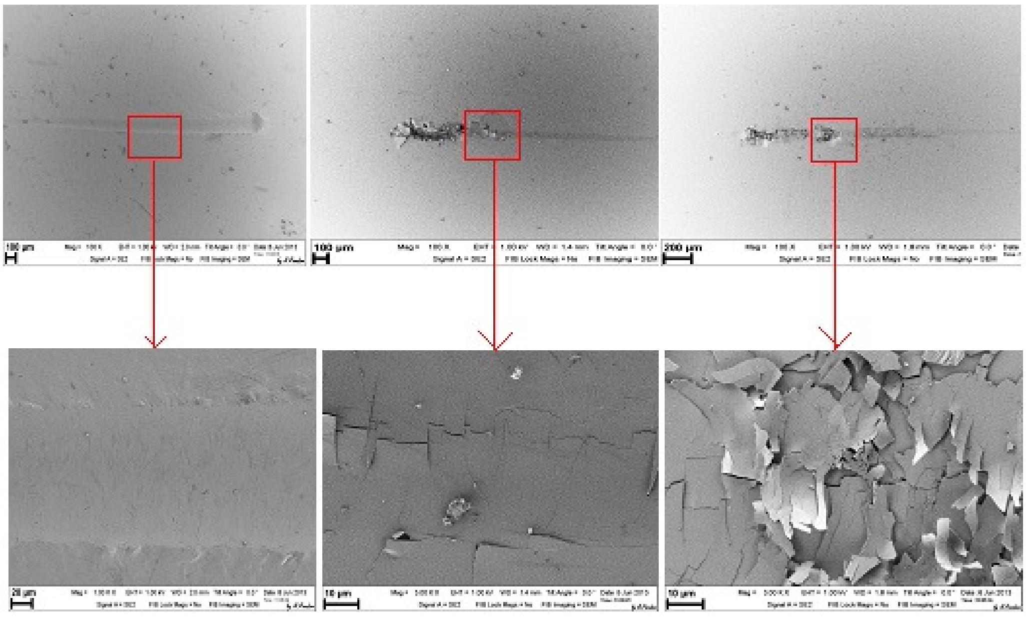

(a) **(b)** **(c)**

Figure 6.15(a-c): SEM images of scratch for films A, B and C

6.4.9 *Tribology measurements*

Plot of variation of friction coefficient with distance for the three films is shown in **Figure 6.16**. Friction coefficient of these films is less than 0.04 which clearly indicates superior tribological properties. Friction coefficient of film A is less than 0.02 compared to films B and C. The trend of friction coefficient in films B and C is same. This is directly corroborated by scratch induced deformation which is similar in nature. The SEM images of wear tracks for the films A-C are shown in **Figure 6.17(a-c)** respectively.

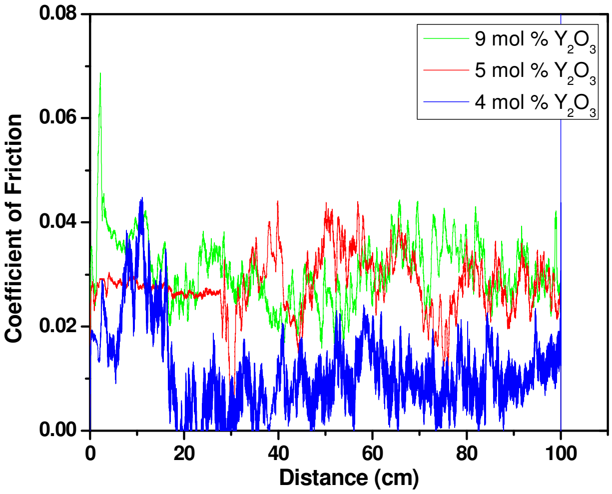

Figure 6.16: Coefficient of friction vs. distance

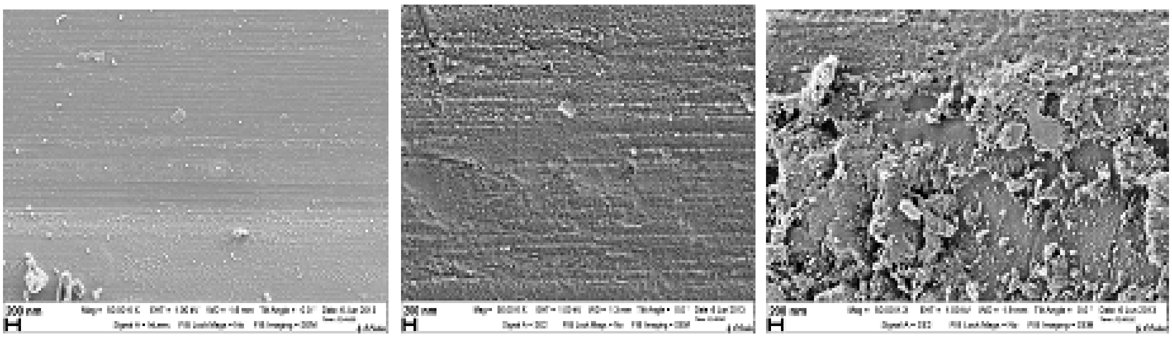

(a) **(b)** **(c)**

Figure 6.17 (a-c): SEM images of middle portion of wear track of film A, B and C

6.5 Discussion: Effect of variation of yttria content on properties of YSZ thin films

From **Table 6.1**, it is seen that the thickness of the films and yttrium oxide content increase with the increase in the temperature of Y $(tod)_3$ containing bubbler. As reported in the literature approximately 3-5 mol % of yttria is required for formation of PSZ while 8 mol % yttria stabilizes zirconia in cubic phase (YSZ) [**89**, **78**]. However, it is seen from the GIXRD pattern shown in **Figure 6.1** that the diffraction peaks are broad for the three deposited films making phase identification difficult. It is observed that the crystallite size is minimum for film C and maximum for film B. The diffraction pattern for film B indicates dominance of tetragonal phase. The diffraction lines corresponding to reflections (101), (110), (200), (211) as indicated in JCPDF card no.82-1241 are in good agreement with observed diffraction pattern of film B. The FTIR spectra **(Figure 6.2)** further help in identifying the phases. From the FTIR spectra**,** it is seen that film A shows a mixture of monoclinic and tetragonal phases. As yttria content increases further in film B; along with monoclinic phase, there is dominant tetragonal phase indicated by a broad band at ~ 550-650 cm^{-1}. With 9 mol % of yttria in film C, the prominent peak at ~ 636 cm^{-1} indicates the formation of cubic phase [**82**]. Earlier Holzschuh and Suhr reported formation of fully stabilized cubic structure over a wide range of yttria content from 3.5 to 80 mol % by using RF plasma enhanced CVD and heptanedionate precursors [**125**]. While in the present case as yttria content increases, the monoclinic phase transforms partly to tetragonal phase and with further increase of yttria content, fully stabilized cubic phase is formed as observed in case of film C.

The variation of refractive index with wavelength for the three films is shown in **Figure 6.3(a)**. Here, we do not observe a particular trend in variation of refractive index with the yttria content. It has been reported in the literature that refractive index decrease as yttria content in the film increase. It has been reported by M. Boulouz et al. that refractive index increase with yttria content upto 8 mol % and then decreases with increase in yttria content [**79**]. Xiao et al. deposited YSZ by using electron beam evaporation and found refractive index increased with increase in deposition rate and decreased with increase in oxygen partial pressure [**78**]. As reported by Heiroth et al. the crystallite size has stronger influence on optical properties of zirconia based oxide thin films [**91**]. Ramana et al. have reported that nanocrystalline nature enhances the density of the film resulting in increase of refractive index [**65**]. This is observed in case of film C, which demonstrates enhancement of refractive index due to smaller crystallite size. Similarly, film A exhibits higher value of refractive index due to smaller crystallite size as compared to film B. The extinction coefficient value for all films is zero within the measurement limit indicating that the films are transparent within the investigated spectral range (300-1200 nm) with no inter-band absorption. M. Boulouz et al. have observed an increase in extinction coefficient with increase in dopant concentration [**79**]. The transparency of the films can be attributed to the deposition process of RF plasma enhanced MOCVD. The fragmentation of bulky precursor molecule can be efficiently achieved due to high internal energy of plasma medium. There is uniform mixing of precursors and the reactivity of precursors is enhanced, resulting in dense coatings with good stoichiometry. Utilization of sputtering deposition techniques in enhancing the packing density has been demonstrated earlier. It has been reported that sputtering technique result in dense and moisture stable films [**79**]. RF PECVD is one such technique which combines the advantages of CVD and sputtering technique. The RF self-bias on the substrates dictates the energy of bombarding ions on the substrate. Therefore, RF self-bias plays an important role in deciding the composition and structure of the deposited films [**120]**. The bombarding ions remove the loosely bonded atoms and thus help in reducing the degree of contamination in the deposited films.

The advantages of octanedionate precursors used in this deposition are they are volatile as compared to other metal organic precursors and result in less carbon contamination in the deposited films. The hydrogen in case of heptanedionate precursors is replaced by methyl radical in octanedionate precursor, leading to enhanced volatility due to the shielding effect of this bulky radical [**8**]. The dense and uniform nature of coatings is also evident from FESEM images shown in **Figure 6.5**. The AFM images (**Figure 6.6**) show sharper features in case of film B as compared to the other two films indicating higher value of roughness of film B. This may be due to better crystallinity of film B as compared to other films [**74**].

XPS analyses indicate three different chemical environments for the zirconium atoms in the deposited films. There is some degree of non- stoichiometry on the surface of the films indicated by presence of peak pair shifted to lower binding energy at ~181.5 and 183.9 eV. The presence of small amount of Zr-OH is also seen on the surface of the films. This may be due to moisture adsorption as the films were not sputtered prior to XPS scan. For the same reason it can be seen from Y 3*d* peak deconvolution that there are peaks corresponding to Y-OH bond in addition to peak pair corresponding to stoichiometric Y_2O_3. The Zr-OH content is higher in film B as compared to the other two films. This indicates that film B has columnar structure which can lead to increased moisture absorption. Columnar structure reduces the packing density resulting in decrease of refractive index [**91, 65**] and increase in roughness. This corroborates with the ellipsometry and AFM results of film B.

Variation of structure with change in yttria content is observed in the XANES spectra. When compared with theoretical spectra of different phases of zirconia, it is inferred that XANES spectra of the films A, B and C agree with presence of predominant monoclinic, tetragonal and cubic phases respectively as reported by Dura et al. [**86**].

The bond distances and disorder (Debye-Waller) factors (σ^2), which give the mean-square fluctuations in the distances, have been used as fitting parameters for the EXAFS spectra.

Taking clue from the XANES analysis, the experimental $\chi(r)$ versus r spectra of the YSZ thin film at Zr K edge have been fitted with theoretical spectra for films A, B and C assuming monoclinic, tetragonal and cubic structure respectively. The structural parameters for the above structure are obtained from the reported values in the literature [**133-135**]. The coordination number of the Zr-O shells in all these structures have been kept fixed while fitting. It has been observed that the $\chi(r)$ versus r spectrum of the film A can be best fitted with monoclinic structure, while fitting with tetragonal or cubic structure doesn't yield a good fit. However, when the coordination number N is varied during fitting with tetragonal and cubic structure, the Zr-O coordination turns out to be ~ 7 which is the coordination of Zr-O in monoclinic structure. For films B and C, the best fit is obtained with tetragonal and cubic structure respectively with physically acceptable fitting parameters while fitting with other structures yield unphysical values of the fitting parameters. However FTIR analyses indicate that films A and B consist of both monoclinic and tetragonal phases. Thus, it is confirmed that zirconia has dominant monoclinic phase in film A and dominant tetragonal phase in film B while cubic phase is present in film C.

However, it is observed from the EXAFS results that the value of Debye Waller factor increases with increase in yttria doping concentration which implies that the distortion in general increases from monoclinic to cubic structure. Though cubic is more symmetric structure distortions occur to accommodate ZrO_7 polyhedra which are not regular features of the fluorite type structure [**85**]. The Y K edge EXAFS analysis shows that the Y^{+3} ions substitutes the Zr^{+4} ions in the zirconia crystal structure. However the oxygen coordination around Y^{+3} ions remains 6 which suggests that oxygen vacancies exist near Y^{+3} ions in order to compensate the charge differences between Y and Zr cations. Conversely, P. Li et al. [**85**] have reported zirconia atoms to be the nearest neighbors of oxygen vacancies as in their case yttrium atom maintained eight fold co-ordination.

It should be noted from **Table-6.3** and **6.4** that Zr-O bond lengths in films B and C are lower than the theoretical bond lengths in pure ZrO_2 while, the Y-O bond lengths in these samples are higher than the theoretical Zr-O bond lengths. This is due to the fact that since ionic radius of Y^{+3} is higher than that of Zr, substitution of Zr by Y elongates the bond lengths around Y and reduces the bond lengths around Zr atoms. It can also be observed that no Zr-Zr correlation is found in these samples except a small peak between 3-4 Å for film B indicating that the cation- cation network is more ordered in this tetragonal dominated film as compared to the other two films which corroborates the XRD results also as described above. There is amplitude reduction of peak corresponding to Zr-Zr correlation in fourier transform of nanocrystalline materials as reported by Dura et al. [**86**]. P. Li et al. have also reported that tetragonal structure has the most regular Zr-cation arrangement [**84**].

Tribological behavior of films depends on key factors such as grain size, film porosity, stress and crystalline phase [**89**]. Generally adhesive failure occurs first, followed by cohesive failure at higher loads. In this case from the acoustic energy plots (**Figure 6.14)** it is seen that acoustic energy during the cohesive failure of the film surface is high and this is inherently related to strong covalent bonding in YSZ film. In this case, the acoustic energy of the cohesive and adhesive failure is more or less similar in magnitude. This is seen from the fact that, magnitude of acoustic emission intensity remains nearly same over the whole scratch length. It is clearly seen from the SEM images (**Figure 6.15**) that in the beginning of the scratch test, the adhesive failure is absent but the intensity magnitude of acoustic emission is high and similar to the case where adhesive failure occurs at high progressive load. In all the three films, high elastic energy is released due to cohesive and adhesive failure and show identical magnitude of acoustic emission intensity. However, SEM image of scratch track for film A (**Figure 6.15a**) show that this particular film has high resistance to brittle failure as there is no appearance of cracks in the scratch track. This suggests that film A has high strength of cohesive and adhesive failure. Scratch induced failure is identical in case of films B and C (**Figure 6.15b and 6.15c**) and it is normally indicative of brittle failure.

From **Figure 6.16** it is observed that coefficient of friction is less in case of film A as compared to other two films. From AFM analysis, it is seen that as compared to films B and C, film A has the least roughness value. Resistance to scratch induced crack and cohesive strength is also high in film A. These factors prove superior tribological properties of the film A. However, the presence of deformed adhesive layer is seen in the wear track of this film which may originate from the tribo- chemical reaction. From this result, one can say that this film has weak chemical resistance leading to reaction with ambient condition forming tribo-layer. Due to this tribo-layer the film is protected and helps to reduce the friction coefficient. Crack in the wear tracks is not observed for films B and C but scratch track shows severe cracking in these films. This is related to contact stress which is significantly higher during the scratch test. However, in tribology test, the contact area is larger which does not cross the limit of crack propagation. The enhancement of tribological properties of films A and B in comparison to film C can be attributed to the phenomena of martensitic transformation of metastable tetragonal phase to monoclinic phase. There is 4-5 % volume increase associated with this martensitic transformation resulting into compressive stress which arrests crack propagation and imparts fracture toughness to these films [**83**]. Film C consists of cubic phase and hence is less resistant to fracture as compared to other two films. Higher the yttria content in PSZ, more will be stability of tetragonal phase and lesser will be its wear resistance hence film B is less wear resistant as compared to film A.

Conclusion

Dense and uniform yttria stabilized zirconia thin films have been deposited by RF plasma enhanced MOCVD using octanedionate precursors, $Y(tod)_3$ and $Zr(tod)_4$. RF plasma helps in enhancing the optical properties of the films. All films are found to be transparent from UV to near IR range and have nanocystalline structure. FTIR and XANES measurements confirm that the films with 4 mol %, 5 mol % and 9 mol % yttria are characterized by presence of predominant monoclinic, tetragonal and cubic phases respectively. AFM analysis suggest that as compared to films with 5 mol % and 9 mol % yttria, film with 4 mol % yttria has least roughness value and tribological measurements confirm that the resistance to scratch induced crack and cohesive strength is also high in case of this film .

Chapter 7

Summary and Conclusions

The primary objective of the investigations reported in this thesis is to optimize the process parameters for deposition of yttrium oxide (Y_2O_3) and yttria stabilized zirconia (YSZ) coatings by the process of RF plasma enhanced metalorganic chemical vapor deposition, characterize the deposited coatings by various techniques and explain the characterization results in terms of variations in the deposition process parameters. RF effects can permeate through dielectrics hence deposition of dielectric (ceramic) coatings become feasible under the influence of RF bias on the substrates. By using RF plasma enhanced CVD, thin films can be deposited at low vacuum (rotary) level and hence minor fluctuations in the operating pressure does not create problems as regards to the stability of the plasma during deposition. The various process parameters, such as type of precursor, pressure, substrate temperature, RF self bias on electrode, etc affect the properties of the deposited films. Hence efforts are made to study the effect of variations of some of these process parameters on the properties of the deposited coatings.

The deposited Y_2O_3 and YSZ thin films are characterized by using various characterization techniques such as stylus profilometry, GIXRD, XPS, FTIR, spectroscopic ellipsometry, SEM, EDAX, EXAFS, XANES, AFM and tribological measurements.

There are very few reports on deposition of Y_2O_3 films using RF plasma enhanced MOCVD. To the best of my knowledge, the significant role played by RF self-bias on the substrates during deposition on the properties of the deposited coatings is not reported so far. Hence systematic investigations are made to study the effect of variation of RF self bias on the substrates during deposition (from -50 to -175 V) on the properties of deposited Y_2O_3 films using $Y(thd)_3$ precursor.

Self generated RF bias voltage determines the plasma chemistry and energy of impinging ions on the substrates, thus it is playing a very important role in determining the properties of deposited films. To get information on effect of RF bias variation on local structure of deposited Y_2O_3 thin films, the films are analyzed by EXAFS by probing absorption at Y K-edge. The changes in morphology are studied by AFM. The changes in bond length, co-ordination and disorder parameter obtained by EXAFS data analysis are correlated with the properties of deposited Y_2O_3 thin films.

Type of metalorganic precursor used and its decomposition characteristics, decides the deposition rate and amount of carbon incorporation in the film. This ultimately determines the structure and chemical composition of the deposited films. Hence a comparative study on Y_2O_3 films deposited using $Y(thd)_3$ and $Y(tod)_3$ precursor is done by studying the properties of films deposited by using these two precursors, keeping all other experimental parameters same.

In the present work, yttria is used to stabilize zirconia. Keeping all other experimental parameters same, three films are deposited by varying the concentration of yttria as 4, 5 and 9 mol percent. Depositions are done using $Y(tod)_3$ and $Zr(tod)_4$ precursors. To the best of my knowledge deposition and characterization of YSZ thin film using these octanedionate (tod) precursors is not reported so far.

7.1 Important Conclusions

From the investigations reported here it is evident that RF self bias plays a very important role in deciding about the properties of the deposited yttrium oxide films. Further, it is evident that deposition of Y_2O_3 films on silicon substrates is possible at a reasonably low substrate temperature of 350 °C using a RF plasma MOCVD process. Plasma medium allows uniform mixing of precursors resulting in uniform deposition. Due to deposition under the influence of highly energetic plasma constituents, the deposited coatings exhibit better optical properties without any post treatment. It is seen that all deposited films are transparent from deep UV to near IR range, a very important property that is useful in fabrication of protective optical layers. The results indicate that the reactivity of oxygen in plasma is sufficient and hence degree of non stoichiometry in the deposited films is less.

The films deposited under varying influence of RF self bias on the substrates show changes in the texture and properties of the films indicating a strong dependence of the properties on the substrate bias during deposition. The results of these investigations indicate that it is important to control the bias level on the substrates during deposition to get desired properties of the coating.

Local structure and surface morphology of Y_2O_3 thin films deposited by RF plasma-assisted MOCVD technique with different RF self-bias are investigated by EXAFS and AFM technique. As RF self-bias increases the Y-O bond length reduces and the deposited coating becomes more stoichiomeric and denser. However, for films deposited beyond a certain bias level, the Debye-Waller factor significantly increases manifesting realization of nanostructured films with structural distortion. AFM measurements also indicate that surface morphology of the films changes with change in bias voltage, where it is found that with initial increase in substrate bias more compact microstructure is realized with lower root minimum squared (r.m.s.) roughness. However, roughness increases significantly again as bias is increased beyond – 100 V possibly due to dominating effect of re-sputtering. The changes observed in local structural parameters of the films as obtained above could well be correlated with the observed macroscopic properties of the films.

Investigations reported here indicate that Y_2O_3 films deposited using $Y(thd)_3$ and $Y(tod)_3$ have BCC structure. Higher deposition rate can be achieved using $Y(tod)_3$ precursor. The film deposited using $Y(tod)_3$ precursor are nanocrystalline in nature. These films show enhanced refractive index indicating higher density of the film.

Dense and uniform yttria stabilized zirconia thin films are deposited by RF plasma enhanced MOCVD using octanedionate precursors, $Y(tod)_3$ and $Zr(tod)_4$. Deposition with RF plasma helps in enhancing the optical properties of the films. All films are found to be transparent from UV to near IR range and have nanocystalline structure. FTIR and XANES measurements confirm that the films with yttria content 4 mole % (film A), 5 mole % (film B) and 9 mole % (film C) are characterized by presence of predominant monoclinic, tetragonal and cubic phases respectively. AFM analysis suggest that as compared to films B and C, film A has least roughness value and tribological measurements confirm that the resistance to scratch induced crack and cohesive strength is also high in case of film A.

7.2 Scope of Future work

The RF plasma enhanced MOCVD technique holds a great promise for deposition of the thin films investigated here and also other films as it combines the advantages of CVD with bombardment of the growing film with energetic ions during deposition. By changing

RF self bias on the substrate during deposition, the coatings can be tailor-made according to the requirement. Variations in microstructure of deposited films from polycrystalline to nanocrystalline and amorphous is possible at low substrate temperature.

As deposited thin films exhibit good optical properties, they can be further investigated for its application in various areas like antireflection coatings and other optical coatings. PSZ coatings can be studied further for its use in tribological applications.

Systematic variation in process parameters for deposition of films using other precursors will also give a greater insight into the role played by precursors on the properties of the deposited films. Such studies can be carried out in future.

Studying the effect of varying RF self bias on the substrates during deposition on the properties of deposited partially stabilized zirconia and fully stabilized zirconia thin films will provide a window for deposition of the coatings with desired properties. Such investigations are extremely important for development of these coatings for various technological applications.

Annexure-I

Impedance matching and Smith chart

The output impedance of the RF generator is 50 ohms. The impedance matching network acts as a buffer in matching the impedance of the plasma reactor to that of the RF generator. The purpose of impedance matching network is to ensure that source impedance seen by load is equal to its complex conjugate. In RF circuits impedance matching serves two purposes,

I. Ensures maximum power transfer from generator to the plasma reactor.

II. Minimizes the reflected power and thus prevents damage to the connecting cables and generator.

Forward power is the power delivered by the generator to the load. While, reflected power is the fraction of power that is bounced back from the load. Thus, power available to the load is equal to difference in forward and reflected power. Improper matching results in higher reflected power. This power causes standing waves, resulting in heating of cables and certain components of generator. Under severe conditions, this can damage the cables as well as the generator.

There are two types of matching networks, using transformer and using reactive components. Network using transformer is easy to design, inexpensive and best suited for applications below 1 MHz. Transformers are suitable for matching the resistive part of the load, but cannot match the reactive component of the load. Hence there are chances of reflected power to the generator. The other type of matching network consists of reactive components like capacitors and inductors. These types of networks are suitable for exactly matching load impedance above frequency of 1 MHz. Design of impedance matching network is greatly facilitated by use of graphical tool known as Smith chart. In the year 1930, P.H. Smith had designed this tool and to date has remained popular for analysis of circuit impedances, design of matching networks, computations of noise figures, gain and stability circles [**136**].Smith chart is a polar plot of complex reflection coefficient. The reflection coefficient is defined as ratio of reflected voltage to incident voltage.

$$\Gamma_L = \frac{V_{refl}}{V_{inc}} = \frac{Z_L - Z_O}{Z_L + Z_O} = \Gamma_r + j\Gamma_i \qquad (1)$$

The load impedance is normalized with a characteristic impedance which is a industry standard (for ex-50 ohm)

$$z = \frac{Z_L}{Z_O} = \frac{R + jX}{Z_O} = r + jx \qquad (2)$$

Then the reflection coefficient (equation 1) can be given as,

$$\Gamma_L = \Gamma_r + j\Gamma_i = \frac{(Z_L - Z_O)/Z_O}{(Z_L + Z_O)/Z_O} = \frac{z-1}{z+1} = \frac{r + jx - 1}{r + jx + 1} \qquad (3)$$

$$z = r + jx = \frac{1 + \Gamma_L}{1 - \Gamma_L} = \frac{1 + \Gamma_r + j\Gamma_i}{1 - \Gamma_r - j\Gamma_i} \qquad (4)$$

$$r = \frac{1 - \Gamma_r^2 - \Gamma_i^2}{1 + \Gamma_r^2 - 2\Gamma_r + \Gamma_i^2} \qquad (5)$$

$$x = \frac{2\Gamma_i}{1 + \Gamma_r^2 - 2\Gamma_r + \Gamma_i^2} \qquad (6)$$

From equation 5,

$$r + r\Gamma_r^2 - 2r\Gamma_r + r\Gamma_i^2 = 1 - \Gamma_r^2 - \Gamma_i^2$$

$$\Gamma_r^2 + r\Gamma_r^2 - 2r\Gamma_r + r\Gamma_i^2 + \Gamma_i^2 = 1 - r$$

$$(1 + r)\Gamma_r^2 - 2r\Gamma_r + (r + 1)\Gamma_i^2 = 1 - r$$

$$\Gamma_r^2 - \frac{2r}{r+1}\Gamma_r + \Gamma_i^2 = \frac{1-r}{1+r}$$

$$\Gamma_r^2 - \frac{2r}{r+1}\Gamma_r + \frac{r^2}{(r+1)^2} + \Gamma_i^2 - \frac{r^2}{(r+1)^2} = \frac{1-r}{1+r}$$

$$(\Gamma_r - \frac{r}{r+1})^2 + \Gamma_i^2 = \frac{(1-r)}{(1+r)} + \frac{r^2}{(1+r)^2} = \frac{1}{(1+r)^2}$$

$$(\Gamma_r - \frac{r}{r+1})^2 + \Gamma_i^2 = (\frac{1}{1+r})^2 \qquad (7)$$

The equation (7) is parametric equation for the circle in the form $(x - a)^2 + (y - b)^2 = R^2$ in the complex plane (Γ_r, Γ_i) centered at the coordinates [r/(r + 1), 0] and having a radius of 1/ (1 + r).

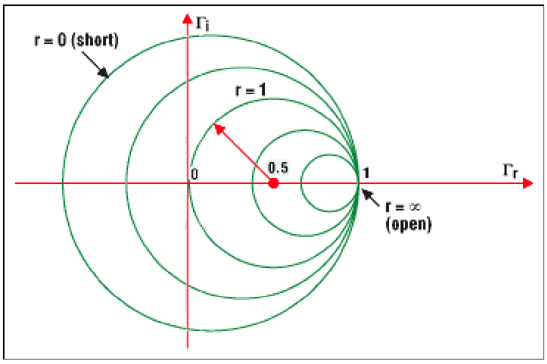

Figure I: Constant resistance circles of Smith chart [Ref-**137]**

Thus circles represent constant resistance values as shown in **Figure I**. For instance, the circle, r = 1, is centered at the coordinates (0.5, 0) and has a radius of 0.5. The point (0, 0), is the reflection zero point (the load is matched with the characteristic impedance, 50 ohm). A short circuit, as a load, is represented by a circle centered at the coordinate (0, 0) and has a radius of 1. For an open circuit load, the circle converges to a single point at (1, 0). This corresponds to a maximum reflection coefficient of 1, at which the entire incident wave is reflected totally.

Now, from equation 6,

$$x + x\Gamma_r^2 - 2x\Gamma_r + x\Gamma_i^2 = 2\Gamma_i$$

$$1 + \Gamma_r^2 - 2\Gamma_r + \Gamma_i^2 = \frac{2\Gamma_i}{x}$$

$$\Gamma_r^2 - 2\Gamma_r + 1 + \Gamma_i^2 - \frac{2}{x}\Gamma_i = 0$$

$$\Gamma_r^2 - 2\Gamma_r + 1 + \Gamma_i^2 - \frac{2}{x}\Gamma_i + \frac{1}{x^2} - \frac{1}{x^2} = 0$$

$$(\Gamma_r - 1)^2 + (\Gamma_i - \frac{1}{x})^2 = \frac{1}{x^2} \qquad (8)$$

Again, equation (8) is a parametric equation of the type $(x - a)^2 + (y - b)^2 = R^2$ in the complex plane (Γ_r, Γ_i) of a circle centered at the coordinates (1, 1/x) and having a radius of 1/x as shown in **Figure II**.

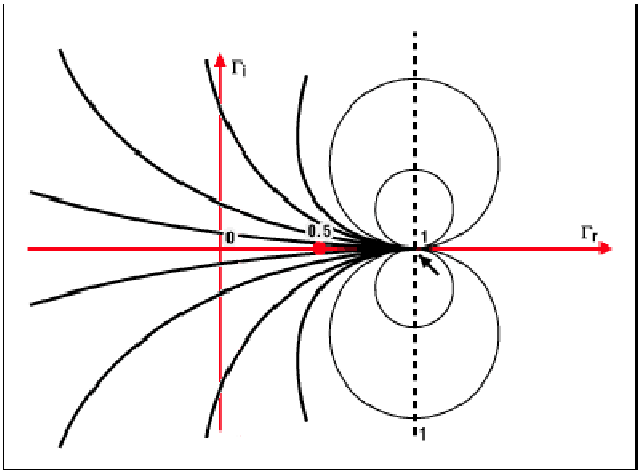

Figure II: Constant reactance circles [Ref-**137**]

The points situated on a circle are all the impedances characterized by same imaginary impedance part value x. For example, the circle x = 1 is centered at coordinate (1, 1) and has a radius of 1. All circles (constant x) include the point (1, 0). Differing with the real part circles, x can be positive or negative. This explains the duplicate mirrored circles at the bottom side of the complex plane. All the circle centers are placed on the vertical axis, intersecting the point 1.

The impedance Smith chart (shown in **Figure III (a)**) will be superposition of both the family of circles. The intersection points will indicate the value of complex impedance values as $z = r + jx$. Addition of reactance connected in series with a complex impedance results in motion along constant resistance circle in the combined Smith chart. Motion along constant conductance circle is produced by a shunt connection.

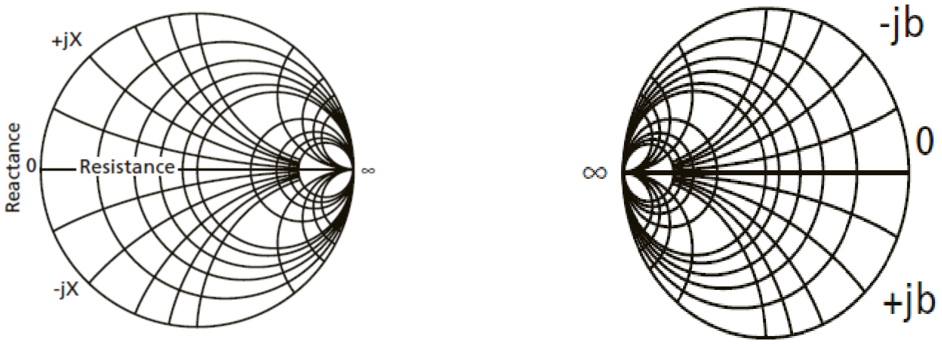

Figure III: (a) Impedance Smith chart (b) Admittance Smith chart [Ref-**138]**

Working with series elements is easier in Smith chart, however for shunt elements, working is greatly facilitated in admittance Smith chart shown here in **Figure III (b)**. The impedance smith chart can be converted into admittance smith chart by rotating every point by 180° around the origin of Γcomplex plane. Thus admittance smith chart will consist of family of circles of constant conductance and constant susceptance. Generally, for working, the impedance and admittance smith charts (Z-Y Smith chart) are overlapped as seen from **Figure IV.**

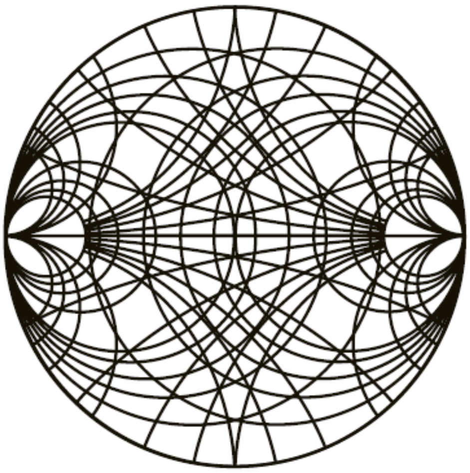

Figure IV: Overlapping of impedance and admittance Smith chart **[**Ref-**138]**

In the present case, capacitance of the electrode measured with LCR meter is 96 pf and capacitance of the cable connected is 104 pf. So system should have a total capacitance of 200 pf and resistance of order of mega ohm. The plasma load can be represented as a parallel combination of resistance and capacitance. The series equivalent can be calculated as,

$$\frac{1}{Z} = \frac{1}{R + j\omega C} \qquad (9)$$

$$Z = \frac{R - j\omega R^2}{(1 + (\omega RC)^2)} = R_L + jX_L \qquad (10)$$

Substituting the values of R and C in the equation (10), value of load impedance obtained is Z_L= 0.003-58.7j. Smith V2.03 software was used for calculating the component values and designing required impedance matching network. This value of load impedance (Z_L) is plotted and represented as point no.1 on Z-Y smith chart (**Figure V**).

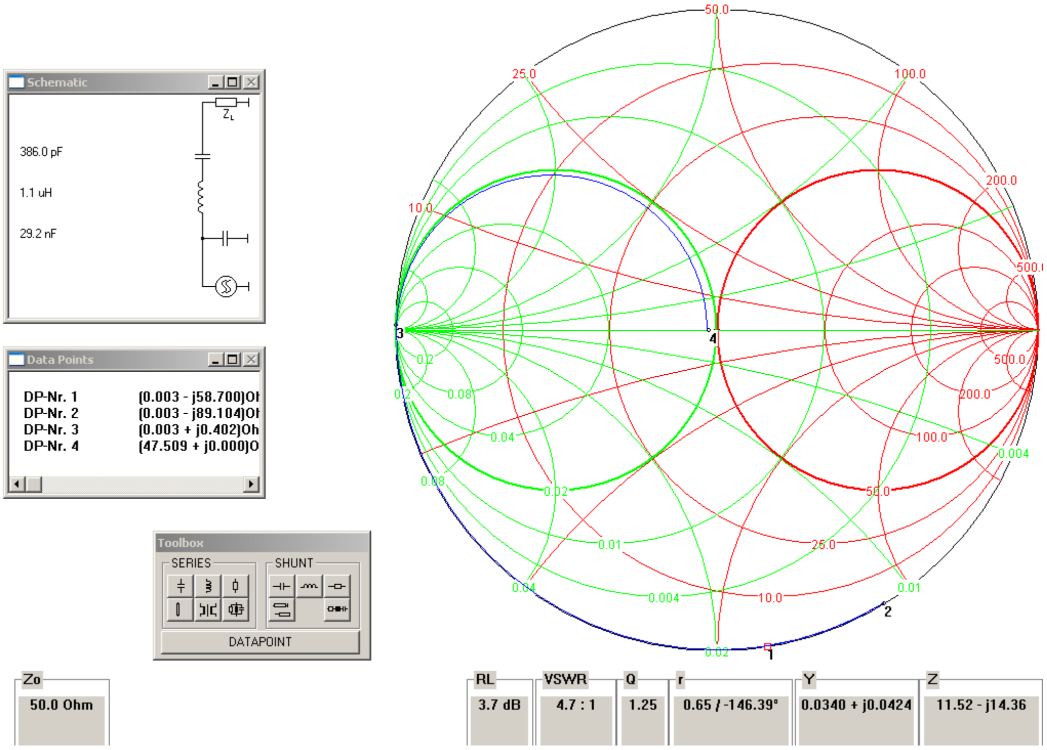

DP-Nr. 1 (0.003 - j58.700)Oh
DP-Nr. 2 (0.003 - j89.104)Oh
DP-Nr. 3 (0.003 + j0.402)Oh
DP-Nr. 4 (47.509 + j0.000)O

Zo: 50.0 Ohm

RL	VSWR	Q	r	Y	Z
3.7 dB	4.7 : 1	1.25	0.65 / -146.39°	0.0340 + j0.0424	11.52 - j14.36

Figure V: Determination of impedance matching network from Smith chart

Connecting a capacitor of value ~386 pf moves the point to no.2. Adding series inductor of value 1.1µH moves point to no.3. Then addition of 29.2 nf finally moves the point to no.4. This value is matched to 47 ohm and has not been exactly matched but is close to source resistance (50 ohm). Taking a clue of the values obtained from the smith chart, the components were chosen. A 5-500 pf variable series capacitor (C_2) and series inductor (L) of 1.1 µH is used. A shunt variable capacitor (C_1) of 10-1000 pf is connected in parallel with few fixed value capacitors so that the combination resulted in value of 23 nf. This circuit was tried for matching impedance of plasma load to the source. However, due to presence of stray capacitance, it is found that the actual values slightly differ. The inductance value required was ~ 1.8 µH and value of shunt capacitance was ~ 22 pf. A D.C. voltmeter (0-500 V) was connected in parallel to the load with an inductor in series. This inductor (~ mH) acts a choke, blocking the A.C. component and allowing only D.C. current to pass through. The bias voltage developed can be measured with the help of the D.C. voltmeter. The forward and reflected power is observed with the help of a cathode ray oscilloscope (CRO).

The value of capacitors can be tuned manually to maximize the forward power and minimize the reflected power. From the values of components actually used, the impedance of the load was back calculated. Here the source impedance is presented as point no.1 (**Figure VI**).

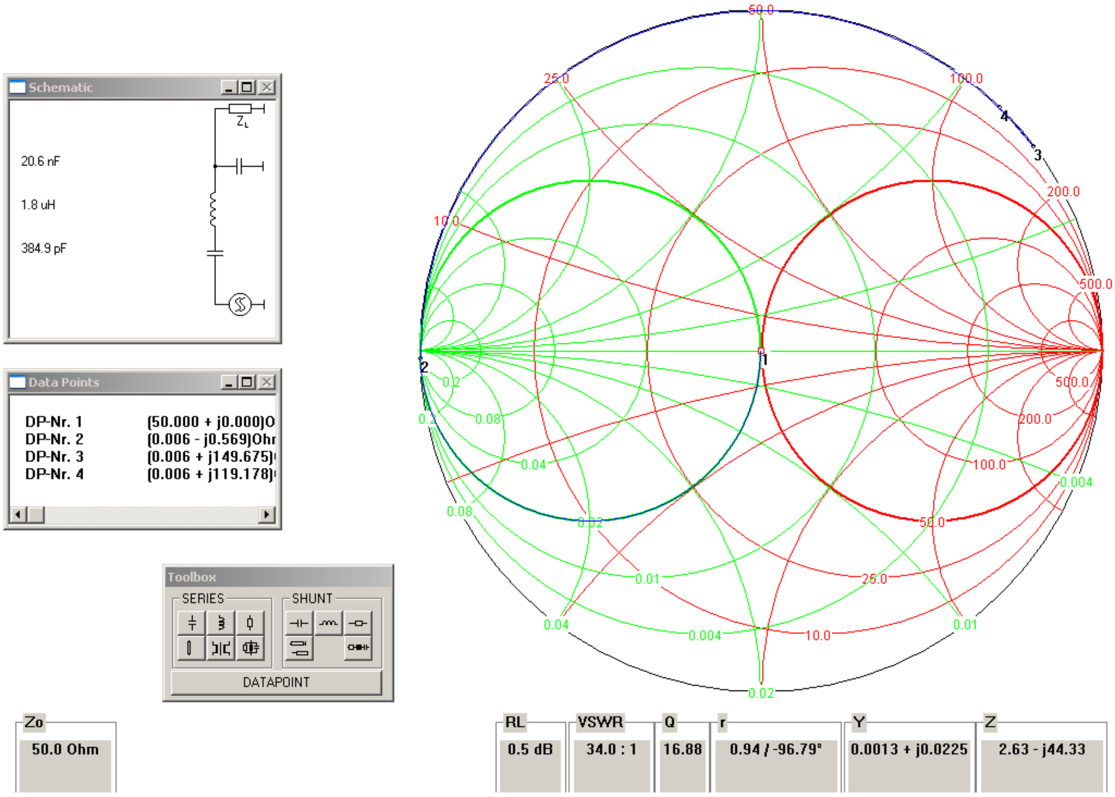

20.6 nF
1.8 uH
384.9 pF

DP-Nr. 1 (50.000 + j0.000)O
DP-Nr. 2 (0.006 - j0.569)Ohr
DP-Nr. 3 (0.006 + j149.675)
DP-Nr. 4 (0.006 + j119.178)

Zo	RL	VSWR	Q	r	Y	Z
50.0 Ohm	0.5 dB	34.0 : 1	16.88	0.94 / -96.79°	0.0013 + j0.0225	2.63 - j44.33

Figure VI: Determination of plasma impedance from the Smith chart

With addition of shunt capacitance (20.6 nf), the point is shifted to no.2, with addition of inductor (1.8 μH), the point shifts to no.3 and after addition of series capacitor (384 pf) finally point no.4 gives impedance value of Z_L =0.006+j119. The actual load impendance is complex conjugate of this value. Hence, the actual value of load impedance is Z_L = 0.006-

j119. The equivalent values of resistance and capacitance can be calculated by using the equations,

$$R = \frac{R_L^2 + X_L^2}{R_L}$$

$$C = \frac{X_L}{(R_L^2 + X_L^2)(2\Pi f)}$$

The value of resistance (R) comes out to be approximately 2.36 MΩ and the capacitance is approximately 98 pf. The discrepancy observed in calculated and measured capacitance may be due to some stray capacitance.

References

[1] Francis F. Chen, '*Introduction to plasma physics and controlled fusion*', 2nd edition, Volume-1: Plasma physics, 1974

[2] A. Bogaerts, E. Neyts, R. Gijbels, J van der Mullen, '*Gas discharge plasmas and their applications*', Spectrochimica Acta Part B 57 (2002) 609-658.

[3] Ravi Dey, '*Some spectroscopic studies on diamond like carbon (DLC) coatings deposited by microwave electron cyclotron resonance (ECR) plasma*',Ph.D. thesis, Pune University, May 2010.

[4] www.glow-discharge.com/?Physical_background:Glow_Discharges

[5] A. Ganguli, R. D. Tarey, '*Understanding plasma sources*', Current Science 83 (3) (2002) 279-290.

[6] Michael Kransnopolski, '*Metalorganic chemical vapor deposition routes for fabrication of rare earth materials*', dissertation, Ruhr University, Bochum Germany 2014.

[7] Joy George, '*Preparation of thin films*', CRC press, USA, 1992.

[8] F. Maury, '*Recent trends in the selection of metal-organic precursors for MOCVD process*', J. Phys. IV 5 (1995) C5-449-C5-463.

[9] Anthony C Jones, Paul R Chalker, '*Some recent developments in the chemical vapour deposition of electroceramic oxides*', J. Phys. D: Appl. Phys. 36 (2003) R80-R95.

[10] Serej V. Pasko, Liliane G. Hubert-Pfalzgraf, Adulfas Abrutis, Phillippe Richard, Ausrine Bartasyte and Vida Kazlauskiene, '*New sterically hindered Hf, Zr and Y β-diketonates as MOCVD precursors for oxide films*', J. Mater. Chem. 14, (2004) 1245-1251.

[11] Milton Ohring, '*Materials Science of thin films, deposition and structure*', 2nd edition, Academic press, USA, 2002.

[12] G. Alarcón-Flores, M. Aguilar-Frutis, M. García-Hipolito, J. Guzmán-Mendoza, M. A. Canseco, C. Falcony, '*Optical and structural characteristics of* Y_2O_3 *thin films synthesized from yttrium acetylacetonate*', J. Mater. Sci. 43 (2008) 3582-3588.

[13] Stuart Deutsch, '*High pressure phase transformations in polycrystalline yttrium oxide*', dissertation, Graduate school New Brunswick Rutgers the State University of New Jersey, 2012.

[14] pubs.rsc.org/en/content/articlelanding/2005/jm/b417143h#!divAbstract

[15] P. Zhang, A. Navrotsky, B. Guo, I. Kennedy, A. Clark, C. Lesher, Q. Liu, '*Energetics of cubic and monoclinic yttrium oxide polymorphs: Phase transitions, Surface enthalpies and stability at the nanoscale*', J. Phys. Chem. C 112(4) (2008) 932-938.

[16] Ralf Riedel, I-Wei Chen (eds.) '*Ceramics Science and technology, Materials and properties*', Wiley publisher, 2010.

[17] R. J. Gaboriaud, F. Pailloux, P. Guerin, F. Paumier, '*Yttrium oxide thin films,* Y_2O_3*, grown by ion beam sputtering on Si'*, J. Phys. D: Appl.Phys.33 (2000) 2884-2889.

[18] J. R. Jayaramaiah, B. N. Lakshminarasappa, B. M. Nagabhushana, '*Luminescence studies of europium doped yttrium oxide nano phosphor*', Sensors and Actuators B 173 (2012) 234– 238.

[19] X. J. Wang, L. D. Zhang, J. P. Zhang, G. He, M. Liu, L. Q. Zhu, '*Effects of post-deposition annealing on the structure and optical properties of* Y_2O_3 *thin films*', Materials letters 62 (2008) 4235-4237.

[20] C. Durand, C. Dubourdieu, C. Vallée, V. Loup, M. Bonvalot, '*Microstructure and electrical characterizations of yttrium oxide and yttrium silicate thin films deposited by pulsed liquid injection plasma enhanced metal organic chemical vapor deposition*', J. Appl. Phys.96 (3) (2004) 1719-1729.

[21] M. Gurvitch, L. Manchanda, J. M. Gibson, '*Study of thermally oxidized yttrium films on silicon'*, Appl. Phys. Lett. 51 (1987) 919-921.

[22] W. J. Varhue, M. Massimo, J. M. Carrulli, V. Baranauskas, E. Adams, '*Deposition of* Y_2O_3 *by plasma enhanced organometallic chemical vapor deposition using an electron cyclotron resonance source*', J. Vac. Sci. Technol. A 11 (1993) 1870-1874.

[23] Cheol Seong Hwang, Hyeong Joon Kim, '*Deposition and characterization of* ZrO_2 *thin films on silicon substrate by MOCVD*', J. Mater. Res. 8 (6) (1993) 1361-1367.

[24] Richard H. J. Hannink**,** Patrick M. Kelly, Barry C. Muddle, '*Transformation toughening in Zirconia-Containing Ceramics*', J. Am. Ceram. Soc.83 [3] (2000) 461–487.

[25] P. C. Clapp, '*How would we recognize a martensitic transformation if it bumped into us on a dark and austy night?*', Journal De Physique IV 5 1995 C8-11-C8-19.

[26] Shruti Barve, '*Plasma assisted chemical vapor deposition and characterization of oxide based coatings*', dissertation, University of Mumbai, 2011.

[27] Xin Xia, '*Computational modelling study of Yttria-stabilized Zirconia*', dissertation, University college, London, 2010.

[28] Mangali Bonne, Masaaaki Haneda, Daniel Duprez, Masakuni Ozawa; '*Effect of addition of* Y_2O_3 *In* ZrO_2 *support on n-butane Pt catalysed oxidation*', Catalysis Communication 19 (2012) 74-79.

[29] www.doitpoms.ac.uk/tlplib/fuel-cells/sofc_electrolyte.php?printable=1

[30] J. Robert Kelly, Isabelle Denry, ‘*Stabilized zirconia as a structural ceramic: An overview*’, Dental materials 24 (2008) 289-298.

[31] F. Milovichi, N. Tabachkova, V. Bublik, E. Lomonova, M. Borik, A. Kulebyakin, V. Myzina, ‘*Study of the structure and mechanical properties of PSZ (Partially stabilized Zirconia) after heat treatment at 1600 °C*’, Proceedings of the international conference Nanomaterials: Applications and properties 2 (4) (2013).

[32] Farshihaghro Ebrahim, ‘*Pyrolysis of yttria stabilized zirconia and its characterization*’, dissertation, University of California, Riverside, 2013.

[33] www.electronicstructure.wikidot.com/predicting-the-ionic-conductivity-of-ysz-from-ab-initio-calc for YSZ structure

[34] Sheng Yue Wang, Zu Hong Lu, ‘*Preparation of* Y_2O_3 *thin films deposited by pulse ultrasonic spray pyrolysis*’, Materials Chemistry and Physics 78 (2002) 542-545.

[35] V. V. Bakovets, T. M. Levashova, V. T. Ratushnyak, L. F. Bakhturova, ‘*Chemical vapor deposition of* Y_2O_3 *films using* $Y(dpm)_3$’, Inorganic Materials 38(4) (2002) 371-373.

[36] R. N. Sharma, A. C. Rastogi, ‘*Structure and composition of interfacial silicon oxide layer in chemical vapor deposited* Y_2O_3-SiO_2 *bilayer dielectrics for metal-insulator-semiconductor devices*’, J. Appl. Phys. 76 (1994) 4215-4224.

[37] D. Niu, R. W. Ashcraft ,Z. Chen, S. Stemmer and G. N. Parsons, ‘*Chemical, physical and electrical characterizations of oxygen plasma assisted chemical vapor deposited yttrium oxide on silicon*’, J. Electrochem. Soc.150 (5) (2003) F102-F109.

[38] G. Apostolopoulous, G. Vellianitis, A. Dimoulas, '*High epitaxial quality Y_2O_3 high-κ dielectric on vicinal Si (001) surfaces*', Appl. Phys. Lett. 81 (19) (2002) 3549-3551.

[39] Phillipe de Rouffignac, Jin-Seong Park, Roy G.Gordon, '*Atomic Layer Deposition of Y_2O_3 thin films from Yttrium Tris(N,N-diisopropylacetamidinate) and water*', Chem. Mater. 17 (2005) 4808-4814.

[40] Y. J. Lee, W. C. Lee, C. W. Nieh ,Z. K. Yang, A. R. Kortan, M. Hong, J. Kwo, C. -H Hsu, '*High-quality nanothick single-crystal Y_2O_3 films epitaxially grown on Si(111):Growth and structural characteristics',* J. Vac. Sci. Technol. B 26(3) (2008) 1124-1126.

[41] Jian Leng, Zhinong Yu, Yuqiong Li, Dongpu Zhang, Xiaoyi Liao, Wei Xue, '*Optical and electrical properties of Y_2O_3 thin films prepared by ion beam assisted deposition*', Appl. Surf. Sci. 256 (2010) 5832-5836.

[42] R. J. Gaboriaud, F. Pailloux, J. Perriere, '*Pulsed laser deposition of Y_2O_3 thin films on MgO*', Appl. Surf. Sci.186 (2002) 477-482.

[43] Shaoqiang Zhang, Rongfu Xiao, '*Yttrium oxide films prepared by pulsed laser deposition*', J. Appl. Phys. 83(7) (1998) 3842-3848.

[44] J. J. Araiza, M. A. Aguilar-Frutis, C. Falcony, '*Optical, electrical and structural characteristics of yttrium oxide films deposited on plasma etched silicon substrates*', J. Vac. Sci. Technol. B 19(6) (2001) 2206-2211.

[45] W. M. Cranton, D. M. Spink, R. Stevens, C. B. Thomas, '*Growth and dielectric characterization of yttrium oxide thin films deposited on Si by r .f .-magnetron sputtering*', Thin Solid Films 226 (1993) 156-160.

[46] Theodosia Gougousi, Zhiying Chen, '*Deposition of yttrium oxide thin films in supercritical carbon dioxide*', Thin Solid Films 516 (2008) 6197-6204.

[47] C .Durand and C. Vallée, C. Dubourdieu, E. Gautier, M. Bonvalot and O. Joubert, '*Interface formation during the yttrium oxide deposition on Si by pulsed liquid-injection plasma enhanced metal-organic chemical vapor deposition*', J. Vac. Sci. Technol. A 22(6) (2004) 2490-2499.

[48] S. A. Barve, Jagannath, N. Mithal, M. N. Deo, A. Biswas, R. Mishra, R. Kishore, B. M. Bhanage, L. M. Gantayet, D. S. Patil, '*Effects of precursor evaporation temperature on the properties of the yttrium oxide thin films deposited by microwave electron cyclotron resonance plasma assisted metal organic chemical vapor deposition*', Thin Solid films 519 (2011) 3011-3020.

[49] S. A. Barve, Jagannath, N. Mithal, M. N. Deo, N. Chand, B. M. Bhanage, L. M. Gantayet, D. S. Patil, '*Microwave ECR plasma CVD of cubic Y_2O_3 coatings and their characterization*', Surf. Coat. Technol. 204 (2010) 3167-3172.

[50] T. T. Van, J. P. Chang, '*Radical-enhanced atomic layer deposition of Y_2O_3 via a β-diketonate and O radicals*', Surface science 596 (2005) 1-11.

[51] Shruti Barve, Mukul Deo, Rajib Kar, Nimisha Sreenivasan, Ramaswamy Kishore, Arup Biswas, Bhalchandra Bhanage, Mohan Rao, Lalit Mohan Gantayet, Dinkar Patil, '*Microwave ECR plasma assisted MOCVD of Y_2O_3 thin films using $Y(tod)_3$ precursor and their characterization*', Plasma Process. Polym. 8 (2011) 740-749.

[52] Frantisek Hanic, Maria Hartmanova, Galina G. Knab, Aida A. Urusovskaya and Khachik S. Bagdasarov, '*Real structure of undoped Y_2O_3 single crystals*', Acta. Cryst. B40 (1984) 76.

[53] Yutaka Nigara, Mareo Ishigame and Takemaro Sakurai, '*Infrared properties of yttrium oxide*', J. Phys. Soc. Jpn. 30 (1971) 453-458.

[54] Y. Repelin, C. Proust, E. Husson, J. M. Beny, '*Vibrational Spectroscopy of the C-Form of Yttrium Sesquioxide*', J. Solid State Chem. 118 (1995) 163-169.

[55] A. Travlos, N. Boukos, G. Apostolopous, A. Dimoulas, C. Giannakopoulos, '*EELS study of oxygen superstructure in epitaxial Y_2O_3 layers*', Materials Science and engineering B 109 (2004) 52-55.

[56] V. Craciun, J. Howard, E. S. Lambers, R. K. Singh, D. Craciun, J. Perriere, '*Low temperature growth of Y_2O_3 thin films by ultraviolet-assisted pulsed laser deposition*', Appl. Phys. A 69 [Suppl.] (1999) S5535-S538.

[57] Xuerui Cheng, Zeming Qj, Guobin Zhang, Hongjun Zhou, Weiping Zhang, Min Yin, '*Growth and characterization of Y_2O_3 thin films*', Physica B 404 (2009) 146-149.

[58] M.-H. Cho, D. -H. Ko, K. Jeong, S. W. Whangbo and C. N. Whang, S. C. Choi, S. J. Cho, '*Structural transition of crystalline Y_2O_3 film on Si(111) with substrate temperature*', Thin Solid Films 349 (1999) 266-269.

[59] R. J. Gaboriaud, F. Pailloux, F. Paumier, '*Characterisation of Y_2O_3 thin films deposited by laser ablation on MgO: why a biaxial epitaxy*', Appl. Surf. Sci. 188 (2002) 29-35.

[60] Takashi Goto, Ryan Banal, Teiichi Kimura, '*Morphology and preferred orientation of Y_2O_3 films prepared by high speed laser CVD*', Surface and Coating technology, 201 (2007) 5776-5781.

[61] M. -H. Cho, D. -H. Ko, K. Jeong, S. W. Whangbo and C. N. Whang, S. C. Choi, S. J. Cho, '*Growth stage of crystalline Y_2O_3 film on Si(100) grown by ionized cluster beam deposition*', J. Appl. Phy. 85 (5) (1999) 2909-2914.

[62] R. W. Tustison, T. E. Varitimos, D. G. Montanari, J. M. Wahl, '*Stress in Y_2O_3 thin films deposited by radio-frequency magnetron and ion beam sputtering*', J. Vac. Sci. Technol. A 7(3) (1989), 2256-2260.

[63] V. Craciun, E. S. Lambers, N. D. Bassim and R. K. Singh, '*Characteristics of ultraviolet-assisted pulsed-laser-deposited Y_2O_3 thin films*', J. Mater. Res.15(2) (2000) 488-494.

[64] A. Huignard, Astrid Aron, Patrick Aschehoug, Bruno Viana, Jeanine Théry,Alain Laurent, Jacques Perrière, '*Growth by laser ablation of Y_2O_3 and Tm:Y_2O_3 thin films for optical applications*', Mater. Chem .10 (2000) 549-554.

[65] C. V. Ramana, V. H. Mudavakkat, K. Kamala Bharathi, V. V. Atuchin, L. D. Pokrovsky and V. N. Kruchinin, '*Enhanced optical constants of nanocrystalline yttrium oxide thin films*', Appl. Phys. Lett. 98 (2011) 031905(1)-031905(3).

[66] Zhonghua Zhu, Daqiang Gao, GuijinYang, Jing Zhang, Jinlin Zhang, Zhenhua Shi, Feng Xu, Hua Gao, Desheng Xue, '*Room temperature ferromagnetism in pure Y_2O_3 nanoparticles*', EPL 97 (2012) 17005-p1-p5.

[67] Y. L. Soo, S. W. Huang, Z. H. Ming, Y. H. Kao, G. C. Smith, E. Goldburt, R. Hodel, B. Kulkarni, J. V. D. Veliadis, R. N. Bhargava, '*X-ray excited luminescence and local structures in Tb-doped Y_2O_3 nanocrystals*', J. Appl. Phys. 83(10) (1998) 5404-5409.

[68] Chang Ki Lee and Hyung –Ho Park , '*Interface control of Y_2O_3 thin film with Si(100) in a metal-(ferroelectric)-insulator-semiconductor structure*', J. Korean Phys. Soc. 46 (1)(2005) 254-257.

[69] M. Sillassen, P. Eklund, M. Sridharan, N. Pryds, N. Bonanos, J. Bottiger, '*Ionic conductivity and thermal stability of magnetron-sputtered nanocrystalline yttria-stabilized zirconia*', J. Appl. Phys. 105 (2009) 104907(1)-104907(6).

[70] S. Heiroth, R. Frison, J. Rupp, T. Lippert, E. Meier, E. Gubler, M. Dobeli, K. Conder, A. Wokaun, L. Gauckler, '*Crystallization and grain growth characteristics of yttria-stabilized zirconia thin films grown by pulsed laser deposition*', Solid State Ionics 191 (2011) 12-23.

[71] Xin Guo, '*On the degradation of zirconia ceramics during low temperature annealing in water or water vapor*', J. Phys. Chem. Solids 60 (1999) 539-546.

[72] C. -B. Cao, J. -T. Wang, W. -J. Yu, D. -K. Peng, G. -Y. Meng, '*Research on YSZ thin films prepared by plasma-CVD process*', Thin Solid Films 249 (1994) 163-167.

[73] M. Hartmanova, I. Thurzo, M. Jergel, J. Bartos, F. Kadlec, V. Zelezny, D. Tunega, F. Kundracik, S. Chromik, M. Brunel, '*Characterization of yttria-stabilized zirconia thin films deposited by electron beam evaporation on silicon substrates*', J. Mater. Sci. 33 (1998) 969-975.

[74] S. Chevalier, M. Kilo, G. Borchardt, J. Larpin, '*MOCVD deposition of YSZ on stainless steels*', Appl. Surf. Sci. 205 (2003) 188-195.

[75] Hussien Ahmed Abbas, Fadwaa Fwad Hamad, Atrss Khair Mohamad, Zeinab Mohamad Hanafi and Martin Kilo; '*Stuctural properties of zirconia doped with some oxides*', Diffusion Fundametals 8 (20008) 7.1-7.8

[76] V. G. Varanasi, T. M. Besmann, R. L. Hyde, E. A. Payzant, T. J. Anderson, '*MOCVD of YSZ coatings using β-diketonate precursors*', J. Alloy Compd. 470 (2009) 354-359.

[77] A. Stamper, D. W. Gereve and T.E. Schlesinger, '*Deposition of textured yttria-stabillized ZrO_2 films on oxidized silicon*', J Appl. Phys. 70(4) (1991)2046-2051.

[78] Qiling Xiao, Hongbo He, Shuying Shao, Jianda Shao, Zhengxiu Fan, '*Influences of deposition rate and oxygen partial pressure on residual stress and microstructure of YSZ thin films*', Thin Solid Films 517 (2009) 4295-4298.

[79] M. Boulouz, A. Boulouz, A. Giani, A. Boyer, '*Influence of substrate temperature and target composition on properties of yttria-stabilized zirconia thin films by r. f. reactive magnetron sputtering*', Thin Solid Films 323 (1998) 85-92.

[80] D. Liu, C. Perry, R. Ingel, '*Infrared spectra in nonstoichiiometric yttriastabilized zirconia mixed crystals at elevated temperatures*', J. Appl. Phys. 64 (1988) 1413-1417.

[81] Z. Qian and J. L. Shi, '*Characterization of pure and doped zirconia nanoparticles with infrared transmission spectroscopy*', Nanostructured materials 10(20) (1998) 235-244.

[82] T. Hirata, E. Asari, M. Kitajima, '*Infrared and raman spectroscopic studies of ZrO_2 polymorphs doped with Y_2O_3 or CeO_2*', J. Solid State Chem. 110 (1994) 201-207.

[83] D. Majumdar, D. Chatterjee, '*X-ray photoelectron spectroscopic studies on yttria, zirconia and yttria-stabilized zirconia*', J. Appl. Phys. 70 (2) (1991) 988-992.

[84] Ping Li, I-Wei Chen, James E.Penner-Hahn, '*X-ray absorption studies of zirconia polymorphs. I.Characteristic local structures'*, Physical Review B 48 (14) (1993) 10063-10073.

[85] P. Li, I-Wei Chen and J. E. Penner-Hahn, '*X-ray absorption studies of zirconia polymorphs. II. Effect of Y_2O_3 dopant on ZrO_2 structure*', Physical Review B 48 (14) (1993) 10074-10081.

[86] O. J. Dura, R. Boada, M. A. López de la Torre, G. Aquilanti, A. Rivera-Calzada, C. Leon and J. Chaboy, '*XANES and EXAFS study of the local order in nanocrystalline yttria-stabilized zirconia*', Physical Review B 87 (2013) 174109(1)-174109(10).

[87] A. G. Evans, N. Burlingame, M. Drary, W. M. Kriven, '*Martenstic transformations in zirconia-particle size effects and toughning*', Acta Metallurgica, 29 (1980) 447-456.

[88] S. Novak, G. Drazic, M. Kalin, '*Structural changes in ZrO_2 ceramics during sliding under various environments*', Wear 259 (2005) 562-568.

[89] M. S. Miller, W. L. Skeicher, P. B. Narayan, G. T. Swami, J. Crist, R. L. Peterson, R. R. Thomas, H. F. Erskine, '*The effect of deposition parameters on the wear properties of yttria-stabilized zirconia overcoats*', J. Appl. Phys.67 (9) (1990) 4872-4874.

[90] Kun'ichi Miyazawa, Kunio Suzuki, Mycong Yong wey, '*Microstructure and oxidation-ressistant property of sol-gel derived ZrO_2-Y_2O_3 films prepared on austenitic stainless steel substrates*', J. Am. Ceram. Soc 78(2) (1992) 347-355.

[91] S. Heiroth, R. Ghisleni, T. Lippert, J. Michler, A. Wokaun, '*Optical and mechanical properties of amorphous and crystalline yttria-Stabilized zirconia thin films prepared by pulsed laser deposition*', Acta Mater 59 (2011) 2330-2340.

[92] J. R. Vargas Gracia, Takashi Goto, '*Thermal barrier coatings produced by chemical vapor depositions*', science and technology of advanced materials 4(2003) 397-402 (review article)

[93] http://www.lanl.gov/orgs/nmt/nmtdo/AQarchive/04summer/XPS.html

[94] http://pubs.acs.org/subscribe/archive/tcaw/11/i06/html/06inst.html#auth

[95] http://www.ccn.yamanashi.ac.jp/~kondoh/ellips_e.html

[96] http://magicspin.jku.at/synchrotron.php

[97] D. C. Konigsberger and R. Prince, '*X-Ray Absorption: Principles, Applications, Techniques of EXAFS, SEXAFS and XANES*', Wiley, New York, 1988.

[98] D. C. Koningsberger, B. L. Mojet, G. E. van Dorssen, D. E. Ramaker, '*XAFS spectroscopy; fundamental principles and data analysis*', Topics in Catalysis 10 (2000) 143-155.

[99] A. C Jones, M. L. Hitchman (eds.), '*Chemical vapor deposition: Precursors, processes and applications*', RSC Publishing, UK, 2009.

[100] K. Jensen, A. Annapragada, K. Ho, J. –S. Huh, S. Patnaik, S. Salim, '*Metalorganic chemical vapor deposition: example of the influence of precursor structure on film properties*', Journal de Physique IV (1991) 02(C2) C2-243-C2-252.

[101] Hideaki Zama, Shunri Oda, '*Properties of Metalorganic Precursors for Chemical Vapor Deposition of Oxide Superconductors*', Jpn. J. Appl.Phys. 29(7) 1990 L 1072-L 1074.

[102] N. S. Nandurkar, D. S. Patil, B. M. Bhanage, '*Ultrasound assisted synthesis of metal-1, 3-diketonates*', Inorg. Chem. Commun. 11(2008) 733-736.

[103] India 236638 (2009), B. M. Bhanage, N. S. Nandurkar, D. S. Patil

[104] Young Hoon Lee, ‘*A role of energetic ions in RF-biased PECVD of* TiO_2’, Vacuum 51(4) (1998) 503-509.

[105] F. Yan, Z. T. Liu, W. T. Liu, ‘*The properties of* Y_2O_3 *films exposed at elevated temperature*’, Physica B 406 (2011) 2827-2833.

[106] Hirofumi Fukumoto, Takeshi Imura and Yukio Osaka, ‘*Heteroepitaxial growth of* Y_2O_3 *films on silicon*’, Appl. Phys. Lett-55 (4) (1989) 360-361.

[107] Jiaqi Zhu, Yuankun Zhu, Weixia Shen, Yongjie Wang, Jiecai Han, Gui Tian, Pei Lei, Bing Dai, ‘*Growth and characterization of yttrium oxide films by reactive magnetron sputtering*’, Thin Solid Films 519 (2011) 4894-4898.

[108] Neil T. McDevitt and A. D. Davidson, ‘*Infrared Lattice Spectra of Cubic Rare Earth Oxides in the Region 700 to 50* cm^{-1}’, J. Opt. Soc. Am. 56(5) (1966) 636-638.

[109] S. A. Barve, Jagannath, M. N. Deo, R. Kishore, A. Biswas, L. M. Gantayet, D. S. Patil, ‘*Effect of argon ion activity on the properties of* Y_2O_3 *thin films deposited by low pressure PACVD*’, Appl. Surf. Sci. 257 (2010) 215-221.

[110] You Song Kim, Weon Hyo Kim, ‘*Optical loss mechanism in yttria thin film waveguides*’, Optical Materials 14 (2000) 229-234.

[111] Basak Yazgan Kokuoz, Karn Serivalsatit, Baris Kokuoz, Olt Geiculescu, Exley McCormick, John Ballato, ‘*Er-Doped* Y_2O_3 *Nanoparticles: A Comparison of Different Synthesis Methods*’, J. Am. Ceram. Soc. 92(10) (2009) 2247-2253.

[112] M. Winterer, R. Nitsche, H. Hahn, ‘*EXAFS of nanocrystalline* Y_2O_3’, J. Phys IV France 7 (1997) C2-1211-C2-1212.

[113] M. Winterer, R. Nitsche, H. Hahn, ‘*Local structure in nanocrystalline* ZrO_2 *and* Y_2O_3 *by EXAFS*’, Nanostructured Materials 9 (1997) 397-400.

[114] CHENG Xue-Rui, DAI Hai-Yang, QI Ze-Ming, WANG Yu-Yin, ZHANG Guo-Bin, '*Local structure of oxygen –deficient Yttrium oxide*', Chinese Physics C 37 (2013) 098002-1-098002-4.

[115] Yasushige Kuroda, Hideaki Hamano, Toshinori Mori, Yuzo Yoshikawa, Mahiko Nagao, '*Specific adsorption behavior of water on a* Y_2O_3 *surface*', Langmuir 16 (2000) 6937-6947.

[116] Zhihu Sun, Wensheng Yan, Tao Yao, Qinghua Liu, Yi Xie Shiqiang Wei, '*XAFS in dilute magnetic semiconductor', Dalton Trans.* 42(2013) 13779-13801.

[117] M. Newville, B. Ravel, D. Haskel, J. J. Rehr, E. A. Stern, and Y. Yacoby, '*Analysis of multiple-scattering XAFS data using theoretical standards*', Physica B 154 (1995) 208.

[118] B. Ravel, '*Commentary on EXAFS Analysis with FEFF and IFEFFIT*', Part 2, (2004). http://xafs.org/Community/NSLSXasTraining?action=AttachFile&do=get&target=stats_in_exfas.pdf

[119] NT-MDT Image analysis reference manual (2012), 2-39-2-40.

[120] S. S. Chopade, S. A. Barve, K. H. Thulasi Raman, N. Chand, M. N. Deo, A. Biswas, Sanjay Rai, G. S. Lodha, G. M. Rao, D. S. Patil, '*RF plasma MOCVD of* Y_2O_3 *thin films: Effect of RF self-bias on the substrates during deposition*', Appl. Surf. Sci 285P (2013) 524-531.

[121] Zhen Guo and Li Tan, '*Fundamentals and Applications of Nanomaterials*', Artech house, Boston, 2009.

[122] N. C. Das, N. K. Sahoo, D. Bhattacharyya, S. Thakur, N. M. Kamble, D. Nanda, S. Hazra, J. K. Bal, J. F. Lee, Y. L. Tai, C. A. Hsieh, '*Correlation between local*

structure and refractive index of e-beam evaporated (HfO_2-SiO_2) composite thin films', J. Appl. Phys.108 (2010) 023515-1-023515-5.

[123] Zeming Qi, Chaoshu Shi, Weiwei Zhang, Weiping Zhang, Tiandou Hu, '*Local structure and luminescence of nanocrystalline Y_2O_3:Eu*', Appl.Phys.Lett. 81(15) (2002) 2857-2859.

[124] B. Preauchat, S. Drawin, '*Isothermal and cycling properties of zirconia based thermal barrier coatings deposited by PECVD*', Surf. Coat. Technol. 146-147 (2001) 94-101.

[125] H. Holzschuh, H. Suhr, '*Textured (100) yttria-stabilized zirconia thin films deposited by plasma enhanced chemical vapor deposition*', Appl. Phys. Lett. 59 (4) (1991) 470-472

[126] H. Holzschuh, H. Suhr, '*Deposition of copper oxide (Cu_2O, CuO) thin films at high temperatures by plasma enhanced CVD*', Appl. Phys. A 51 (1990) 486-490.

[127] A. K. Poswal, A. Agrawal, A. K. Yadav, C. Nayak, S. Basu, S. R. Kane, C. K. Garg, D. Bhattacharyya, S. N. Jha and N. K. Sahoo, '*Commissioning and first results of scanning type EXAFS beamline (BL-09) at INDUS-2 synchrotron source*', AIP Conf. Proc. 1591 (2014) 649.

[128] S. Basu, C. Nayak, A. K. Yadav, A. Agrawal, A. K. Poswal, D. Bhattacharyya, S. N. Jha and N. K. Sahoo, '*A comprehensive facility for EXAFS measurements at INDUS-2 synchrotron source at RRCAT, Indore, India*', J. Phys.: Conf. Ser. 493 (2014) 012032.

[129] H. Zhang, Y. Liu, K. Zhu, G. Siu, Y. Xiong, C. Xiong, '*Infrared spectra of nanometer granular zirconia*', J. Phys.Condens.Mat. 11 (1999) 2035-2042.

[130] M. Boulouz, F. Tcheliebou, A. Boyer, '*Electrical and optical properties of magnetron sputtered Y_2O_3 stabilized ZrO_2 thin films*', J. Eur. Ceram. Soc.17 (1997) 1741-1748.

[131] G. M. Ingo, '*Origin of darkening in 8 wt% yttria-zirconia plasma sprayed thermal barrier coatings*', J. Am. Ceram. Soc.74 (2) (1991) 381-386.

[132] M. Newville, B. Ravel, D. Haskel, J. J. Rehr, E. A. Stern and Y. Yacoby, '*Analysis of multiple scattering XAFS data using theoretical standards*', Physica B: Condens. Matter 208 (1995) 154-156.

[133] D. K. Smith and H.W. Newkirk, '*The crystal structure of baddeleyite (monoclinic ZrO_2) and its relation to the polymorphism of ZrO_2*' , Acta Cryst.18 (1965) 983-991.

[134] G. Teufer, '*The crystal structure of tetragonal ZrO_2*', Acta Cryst.15 (1962) 1187.

[135] D. Steele and B.E.F. Fender, '*The structure of cubic ZrO_2: $YO_{1.5}$ solid solutions by neutron scattering*', J. Phys. C: Solid State Phys.7 (1974) 1-11.

[136] Reinhold Ludwig, Pavel Bretchko, '*RF circuit design, theory and applications*', Pearson education inc., South Asia, 2011.

[137] Maxim application note- 742, '*Impedance matching and smith chart: The fundamentals*', 2002. www.maxim-ic.com/an 742.

[138] www.advanced-energy.com/upload/file/white_papers/eng-white18-270-02.pdf